SDC-92-396

SDC
SOLENOIDAL DETECTOR NOTES

A MONOLITHIC ENDCAP ELECTROMAGNETIC CALORIMETER FOR THE SDC

December 21, 1992

G. Abrams, L. Benedict, A. Ciocio, K. Einsweiler, D. Groom, C. Hawblitzel, C. Hearty, M. Hoff, R.W. Kadel, J. Kadyk, A. Lim, M. Long, Y. Minamihara, W. Pope, M. Pripstein, G. Przybylski, W. Thur, T. Weber, W. Wenzel and M. Wong
Lawrence Berkeley Laboratory

D. Bintinger
SSC Laboratory

P. LeDu
Saclay

SDC-92-396

A Monolithic Endcap Electromagnetic Calorimeter for the SDC

G. Abrams, L. Benedict, A. Ciocio, K. Einsweiler, D. Groom, C. Hawblitzel, C. Hearty, M. Hoff, R. W. Kadel, J. Kadyk, A. Lim, M. Long, Y. Minamihara, W. Pope, M. Pripstein, G. Przybylski, W. Thur, T. Weber, W. Wenzel, M. Wong
Lawrence Berkeley Laboratory

D. Bintinger
Superconducting Super Collider Laboratory

P. LeDu
Saclay

December 21, 1992

Abstract: We propose a monolithic, endcap electromagnetic calorimeter without η bulkheads or ϕ cracks to replace the current wedge based EM calorimeters in the SDC endcaps. We discuss the physics requirements, design goals, mechanical structure, calibration and optical system for the monolithic ECEM. Additionally, we present test beam results showing the proposed support structure is invisible in the active volume of the EM calorimeter, the calorimeter is linear to within 1% and has a resolution of $19\%/\sqrt{E}$ with no constant term ($< 1.4\%$ at the 90% confidence level).

Table of Contents

1. Acknowledgements . . . 1-1

2. Introduction . . . 2-1
   2.1. Introduction References . . . 2-2

3. Physics Parameters . . . 3-1
   3.1. Transverse Segmentation . . . 3-1
   3.2. EM1/EM2 Longitudinal Segmentation . . . 3-2
   3.3. Massless Gap . . . 3-3
   3.4. Pre-shower detector . . . 3-4
   3.5. Shower Maximum Detector . . . 3-5
   3.6. Radiation Damage and Replaceable ECEM Core . . . 3-6
   3.7. Physics Performance References . . . 3-10

4. Mechanical Structure . . . 4-1
   4.1. Basic Structure . . . 4-1
   4.2. Tile Options . . . 4-4
   4.3. Perimeter Structure . . . 4-6
   4.4. Calibration Source Tubes . . . 4-10
   4.5. Shower Maximum Layers . . . 4-10
   4.6. Barrel/Endcap Overlap . . . 4-11
   4.7. Light-tighting System . . . 4-11
   4.8. Tolerances and Manufacturing Techniques . . . 4-11
      4.8.1. Curtains . . . 4-12
      4.8.2. Absorber . . . 4-13
      4.8.3. Tile Gaps and Tolerance Buildup . . . 14-4
   4.9. Assembly . . . 4-16
   4.10. Shipping and Handling at SSCL . . . 4-18
   4.11. Beamline Calibration . . . 4-18
   4.12. Rebuildable Inner Core . . . 4-18
   4.13. Options: The Case for Spokes . . . 4-19
   4.14. Responses to Criticisms . . . 4-24
      4.14.1. Spoke Holes in Scintillator Tiles . . . 4-24
      4.14.2. Spoke hole interference with fiber "sigma" patterns in the tiles 4-25
      4.14.3. Mechanical stress on the scintillator tiles . . . 4-25
      4.14.4. Rotation of the scintillator tiles on their bushings . . . 4-25
      4.14.5. Increased overall thickness of the EM calorimeter . . . 4-25
      4.14.6. Structural mass at the perimeter of the endcap EM module . . 4-25
      4.14.7. Radiation damage of fibers . . . 4-26
   4.15. Mechanical Structure Summary . . . 4-26
   4.16. Mechanical Structure References . . . 4-27

5. Optical System . . . 5-1
   5.1. Description of the System Used in the Calorimeter Test Station Module . 5-1
   5.2. Performance . . . 5-3
      5.2.1. Light Yield . . . 5-3
      5.2.2. Reproducibility/Quality Control . . . 5-8
      5.2.3. Uniformity . . . 5-13
   5.3. Radiation Damage Studies/Silica Fiber Selection . . . 5-13
   5.4. Future Plans . . . 5-17
      5.4.1. Fiber Connectors . . . 5-17
      5.4.2. Radiation Damage . . . 5-17
      5.4.3. Light Yield . . . 5-19
   5.5. Optics System References . . . 5-20

6. Test Beam Results 6-1
6.1. Calorimeter Test Station Module 6-1
6.2. Test Beam Setup 6-5
6.2.1. Scintillation counters 6-8
6.2.2. Finger hodoscope 6-9
6.2.3. Cerenkov Counters 6-10
6.2.4. Trigger System 6-12
6.2.5. Drift Chambers 6-12
6.2.6. Electronics and Online DAQ 6-13
6.3. Drift Chamber Reconstruction 6-14
6.4. Calibrations 6-18
6.4.1. Muons 6-19
6.4.2. Electrons 6-21
6.4.3. Sources 6-23
6.5. Electron Resolution 6-35
6.5.1. Lateral Leakage 6-40
6.5.2. e/μ 6-42
6.6. Crack and Spoke Scans 6-43
6.7. Test Beam References 6-45
7. Cost estimate 7-1
8. Summary, Remaining R&D and Schedule 8-1
9. Appendix A: Surface operations at SSCL 9-1
10. Appendix B: Drawings for Vendor Quotes 10-1

1. Acknowledgements

Many persons contributed to this paper and the success of the test beam program. We wish to thank Pat Bautz for helping with the assembly of the calorimeter test station module, R. Kuiper, R. Post and the LBL shops for producing many parts on a tight schedule, L. Robinson for helping with the paste up of the manuscript, and W. Frisken for useful conversations. We also wish to thank Howard Gordon and J. Scadudo for help with the A3 beamline at BNL.

2. Introduction

The endcap electromagnetic (ECEM) calorimeter provides hermetic coverage for the region $1.4 < |\eta| < 3.0$,* with performance objectives similar to that of the barrel EM calorimeter. However, unlike the barrel, the endcap must satisfy these objectives despite a radiation dose that ranges (after ten years operation at design luminosity of $10^{33} cm^{-2} sec^{-1}$) from 5 Mrad at the inner radius to 50 krad at the outer radius. Given the useful lifetime of 1 Mrad for tile/fiber combinations currently used in the barrel, it is important that the design and choice of materials in the ECEM extend the useful lifetime and simplify the replacement of damaged components.

Mechanically, the endcap EM calorimeter differs from the barrel EM calorimeter in two important aspects: all ECEM lead plates are vertical, and the total weight (30 tons) and size (5m diameter) of the ECEM are compatible with construction as a single monolithic unit. Given the differences in radiation exposure and in mechanical constraints, the optimal structure for the barrel electromagnetic calorimeter is most likely not the optimal structure for the ECEM.

We have developed a monolithic endcap EM design with performance characteristics equivalent to the SDC Technical Design Report (TDR) [2-1] baseline design, but with substantially greater acceptance. We have removed all partitions separating towers and have devised a low mass, diffuse support structure (largely hidden behind the barrel EM section) that obscures less than 0.15% of the fiducial area of the ECEM. Thus, there are no ϕ cracks between sectors and no η bulkheads. The elimination of these gaps is especially important in the ECEM, where cracks of finite size subtend larger intervals in ϕ and η. As a result, the calorimeter has high acceptance for electrons and photons, and is uniform, allowing for a low constant term. To contend with the high radiation doses, the design incorporates two longitudinal segments, $9X_o$ and $13X_o$ thick, which allows one to make corrections for possible radiation damage in the case of isolated electrons and photons. As in the barrel, a layer is reserved for a shower-max detector at $\approx 6X_o$. In addition, a rebuildable core in the highest

* We follow the standard SDC convention for defining a cartesian coordinate system: the z axis is along the beam line, y is vertical and x is chosen to form a right handed coordinate system. Pseudo-rapidity (η) is then defined by $\eta = -ln(tan(\theta/2))$ where θ (and ϕ) have their usual definitions for a spherical coordinate system.

radiation region ($2 <| \eta |< 3$) allows the replacement of radiation damaged components near the inner radius without disturbing the remaining 80% of the ECEM.

We describe below the design of the ECEM and the results from our ECEM calorimeter test station module, as well as schedule and cost estimates. We begin with a discussion of the physics parameters for the ECEM in Chapter 3. While these requirements are largely repeated from the TDR, the design has evolved and some departures from the TDR need explanation. In Chapter 4 we discuss the mechanical design of the ECEM, including justification for the mechanical parameters, supports, assembly technique and the replacement scenario for radiation damaged scintillator.

In order to test the performance of our monolithic ECEM design, we have constructed and tested a 16 tower, 32 channel, calorimeter test station module. The optical tests leading to the design and production of the module are presented in Chapter 5. This calorimeter module was tested in the Brookhaven A3 test beam and the results of the test beam work are presented in Chapter 6. This chapter incudes a description of calorimeter test station module, the beam line instrumentation and related electronics, as well as the calibration, resolution, linearity, light yield, and transverse uniformity of the calorimeter module.

In Chapter 7 we discuss an updated WBS outline and cost estimate for the ECEM. Chapter 8 summarizes the work completed and discusses the remaining R&D effort and the schedule for the ECEM fabrication.

2.1. Introduction References

[2-1] SDC Collaboration, Technical Design Report,SDC-92-201, SSCL-SR-1215,(1992).

3. Physics Parameters

The performance requirements of the ECEM as taken from the TDR are summarized in Table 3-1. Most of these numbers need no special justification here. However, the role of the massless gap, the longitudinal segmentation and the location of the shower maximum detector are different in the endcap as compared to the barrel. We comment specifically on these areas below, as well as other aspects of the endcap calorimeter.

Table 3-1. ECEM Calorimeter Performance Features.

Calorimeter Property	Requirement
Coverage	$1.4 <\| \eta \| < 3.0$
E_t Resolution	$\frac{\delta E_t}{E_t} < 0.15/\sqrt{E_t} \oplus 0.01$
Pb Absorber Thickness	6 mm
Depth	25 X_o
Longitudinal Segmentation	EM1 ($9X_o$) + EM2 ($16X_o$)
Non-Linearity	< 1% after correction
Dynamic Range	20 MeV < E_t < 5 TeV
"Massless" gap coverage	$1.4 <\| \eta \| < 1.6$
"Pre-shower" detector coverage	$1.6 <\| \eta \| < 3.0$
"Pre-shower" detector depth	$2.2X_o$
"Shower Max" detector depth	$5.5X_o$
Transverse Segmentation	
$1.4 <\| \eta \| < 2.0$	$\delta\eta \times \delta\phi = 0.05 \times 0.05$
$2.0 <\| \eta \| < 2.6$	$\delta\eta \times \delta\phi = 0.1 \times 0.1$
$2.6 <\| \eta \| < 3.0$	$\delta\eta \times \delta\phi = 0.2 \times 0.2$

3.1. Transverse Segmentation

The transverse segmentation of the endcap has evolved since the TDR. In particular, it was observed that the TDR design had five different η boundaries where the segmentation changed in the hadron and EM compartments. The number of electromagnetic tower per hadron towers was less than optimal and changed as a function of η without any coordination between the two compartments.

In the new configuration there are always four EM towers per hadron tower, except for $| \eta |> 2.6$. The transverse segmentation in the endcap is shown in Fig. 3-1. Near $| \eta | = 1.4$

both the EM and hadronic segmentation is consistent with the barrel at $\delta\eta \times \delta\phi = 0.05 \times 0.05$, and the segmentation in the hadron calorimeter behind it is $\delta\eta \times \delta\phi = 0.1 \times 0.1$. There is a boundary at $|\eta| = 2.0$ where both the EM and hadron tower sizes double. Above $|\eta| = 2.6$, the EM size doubles again to $\delta\eta \times \delta\phi = 0.2 \times 0.2$, but the hadron segmentation remains at $\delta\eta \times \delta\phi = 0.2 \times 0.2$.

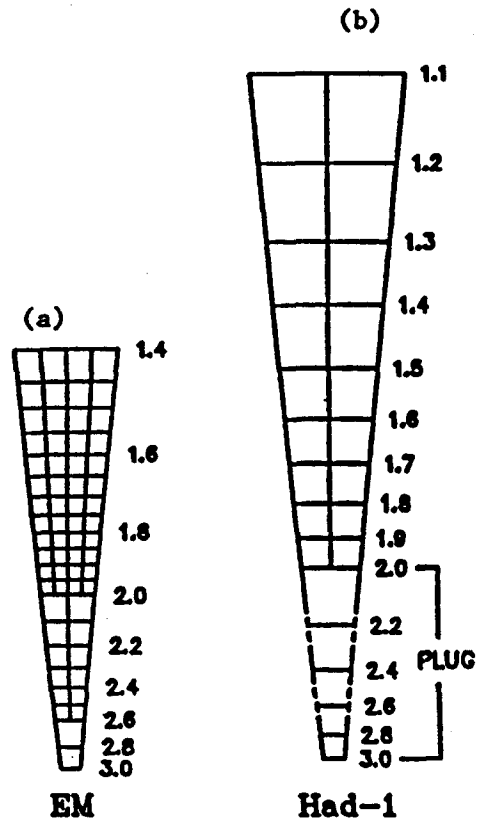

Fig.3-1. Transverse segmentation in the endcap (a) electromagnetic and (b) hadronic towers

3.2. EM1/EM2 Longitudinal Segmentation

The endcap calorimeter is divided into two longitudinal components to aid in correcting for radiation damage induced predominately by low energy photons from π^0 decays in minimum bias events. In the TDR, this boundary is coincident with the location of the shower maximum position detector at about $7X_o$. A recent report [3-1] indicates that the effects of radiation damage can be better compensated if the transition between the EM1 and EM2 sections occurs at $9X_o$. Figure 3-2, taken from this report, shows the change in constant term in the resolution as a function of the boundary between the EM1 and EM2 sections. There is a clear minimum at about $9X_o$, independent of the total amount of radiation damage.

Since 2 GeV photons (typical of the energy of photons from π^o decay in this region of the detector) have their maximum shower development at $4 - 5X_o$, the boundary is selected so that most of the radiation damaged scintillator is incorporated into EM1 section. We have put the boundary between the EM1 and EM2 sections at $\approx 9X_o$.

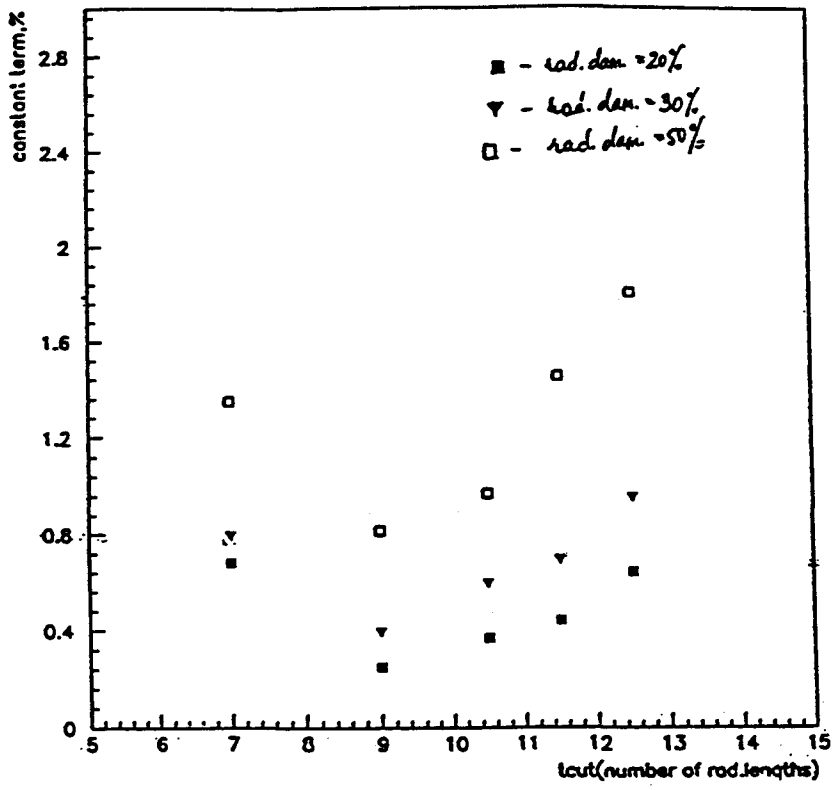

Fig.3-2. Constant term in the resolution function as a function of the boundary between the EM1 and EM2 compartments. This result of a EGS simulation, assumed the radiation damage in the calorimeter had the same profile as a 2 GeV electron showers. The different points are for 20%, 30% and 50% light loss [3-1].

3.3. Massless Gap

Like the barrel, the endcap EM calorimeter has a leading "massless gap" tile layer to compensate for the energy lost in the coil. This tile is foreseen to be a double thickness (8 mm) tile with two fiber readouts. One fiber is routed to the tower sum, the second fiber to a multi-channel photodetector. Other than the coil there is no absorber in front of the massless gap tile. It is possible to add Pb here, should one want to compensate or "even out" mechanical structures inside the coil cryostat.

3.4. Pre-shower detector

Above $|\eta| = 1.6$ there is no coil in front of the endcap EM calorimeter and, hence, the massless gap is not needed. In Fig. 3-3 we show the tile layering configuration we have chosen.

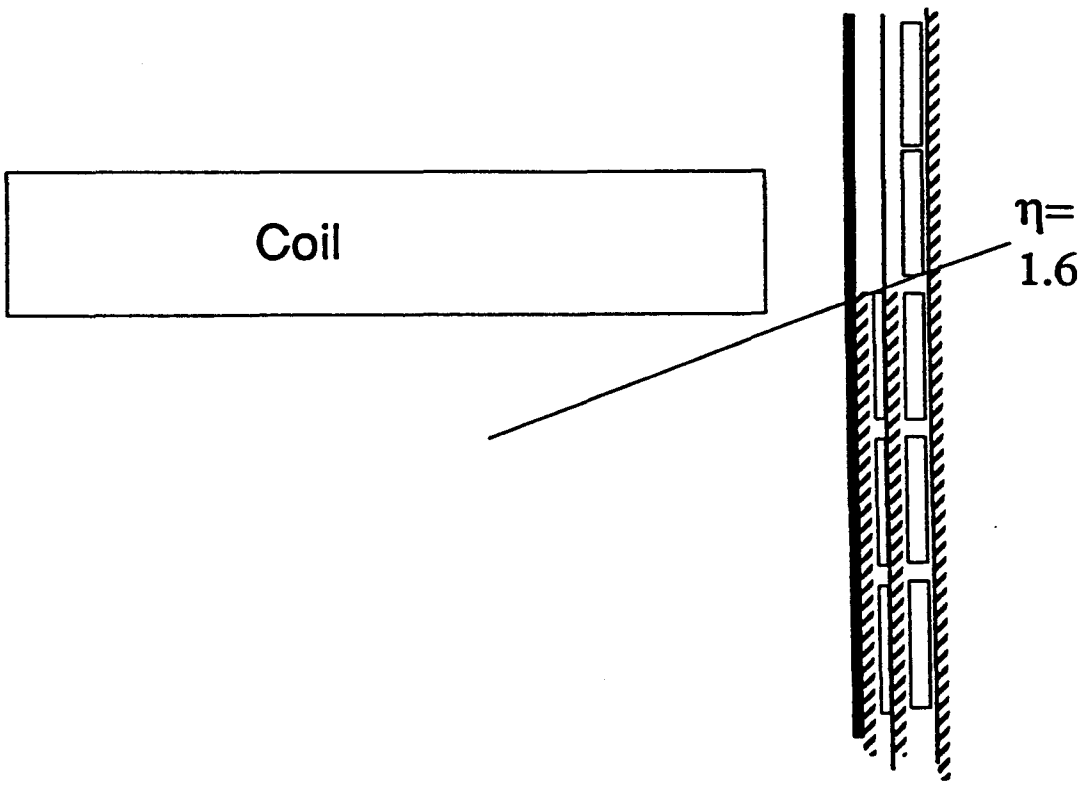

Fig.3-3. "Massless" gap pushed back deeper into the ECEM structure so that beyond $|\eta| > 1.6$ it serves as a pre-radiator but without interrupting the sampling fraction of the calorimeter.

The special massless gap/pre-shower layer is located in the mechanical structure of the ECEM so that for $|\eta| > 1.6$ it appears after the second absorber plate in the calorimeter. In this configuration 1) no material is added in the tracking volume, 2) the massless gap is at the correct depth behind the coil and 3) the pre-shower is at about the right depth in the remainder of the ECEM calorimeter. The pre-shower tiles will be implemented as either a single 8 *mm* thick tiles with two readout fibers; or as two independent tiles, one for the tower sum and the second for the pre-shower readout.

3.5. Shower Maximum Detector

The shower maximum detector is essentially as described in the TDR except for two changes. First the number of tiles has been upgraded to reflect the new transverse segmentation as discussed above. Figures 3-4 and 3-5, taken from Revision F of the SDC parameters book [3-2], shows the mechanical segmentation and electronic segmentation of the shower maximum detector.

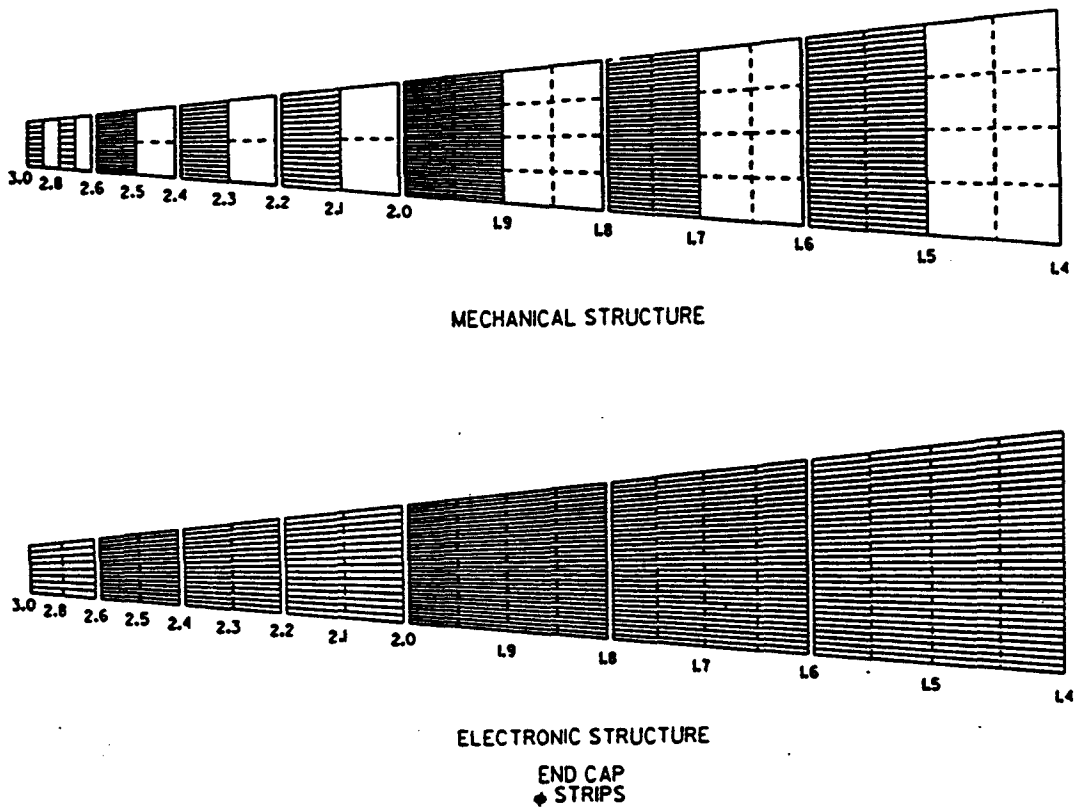

Fig.3-4. Mechanical and electronic segmentation of the ϕ strips in the shower maximum detector in the endcap. The dotted lines represent the η boundaries of the EM towers.

As in the barrel, each readout channel corresponds to two physical shower maximum tiles. Each tower in the EM calorimeter is crossed by 8 strips in the ϕ direction and 8 strips in the η direction. In the readout of the ECEM, each η channel covers $2\pi/32$ units in ϕ; and each ϕ channel covers 0.1 unit in η. This segmentation is consistent with the segmentation of the barrel.

Compared to the parameters book, we have moved the shower maximum detector forward in the ECEM from $7X_o$ to $\approx 5.5X_o$ deep (after 5 Pb plates). Simulation studies have shown that one can obtain better $\pi^o - \gamma$ separation with the shower maximum detector at this

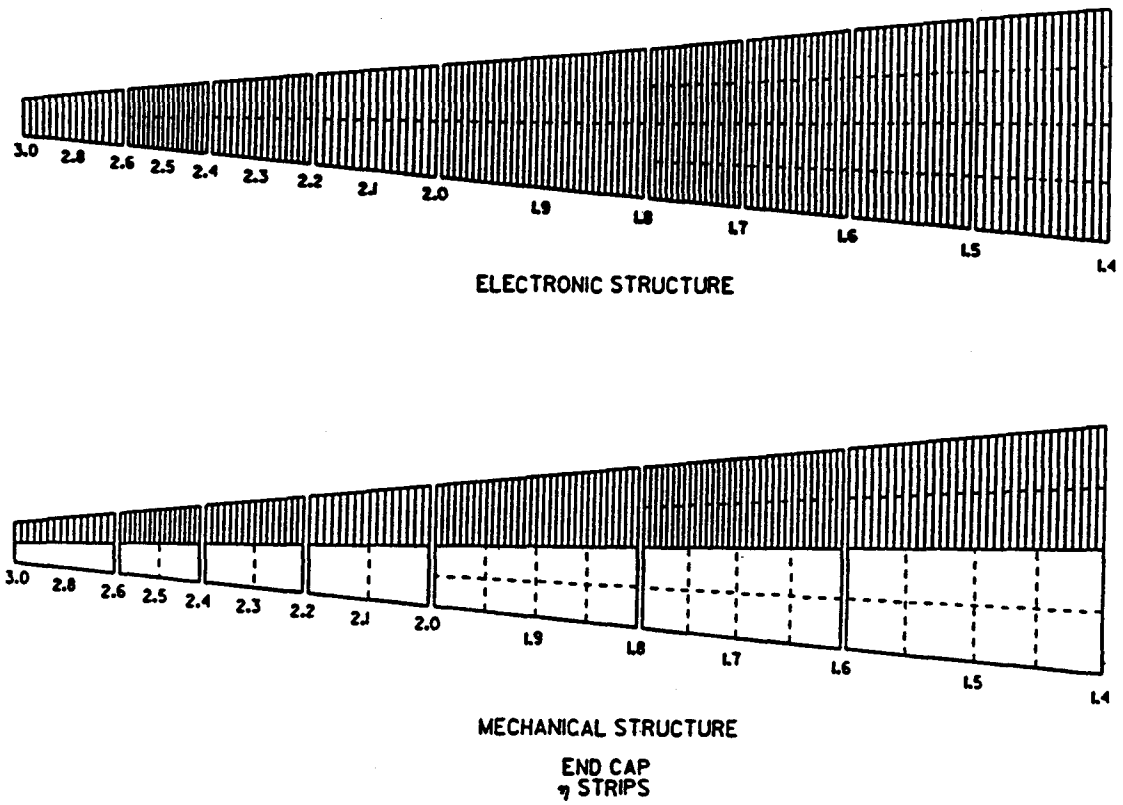

Fig.3-5. Mechanical and electronics segmentation of the η strips in the shower maximum detector in the endcap. The dotted lines represent the η boundaries of the EM towers.

location as compared to previous locations deeper in the calorimeter [3-3]. This result is shown in Fig. 3-6 where the identification efficiency for a single photon is plotted versus P_t for two depths of the shower maximum detector inside the calorimeter.

3.6. Radiation Damage and Replaceable ECEM Core

The critical issue for scintillator calorimetry is the finite lifetime and consequent reduction in light yield of the scintillators and fibers in the radiation field of the detector. In the acceptance of a calorimeter based on scintillating plastic, one of the mitigating factors acknowledged by the SDC collaboration was that the volume of the calorimeter expected to experience radiation damage is small. It seems prudent, therefore, to design the system so that the small sections of the calorimeter where damage is anticipated can be rebuilt with minimal impact on the rest of the experiment or schedule .

Figure 3-7 shows the expected radiation dose in the endcap region due to minimum bias events after 10 years of running at a luminosity of $10^{33} cm^{-2} sec^{-1}$ [3-4]. The radiation dose in the endcap is greatest at electromagnetic shower maximum, between 5 and 6 radiation

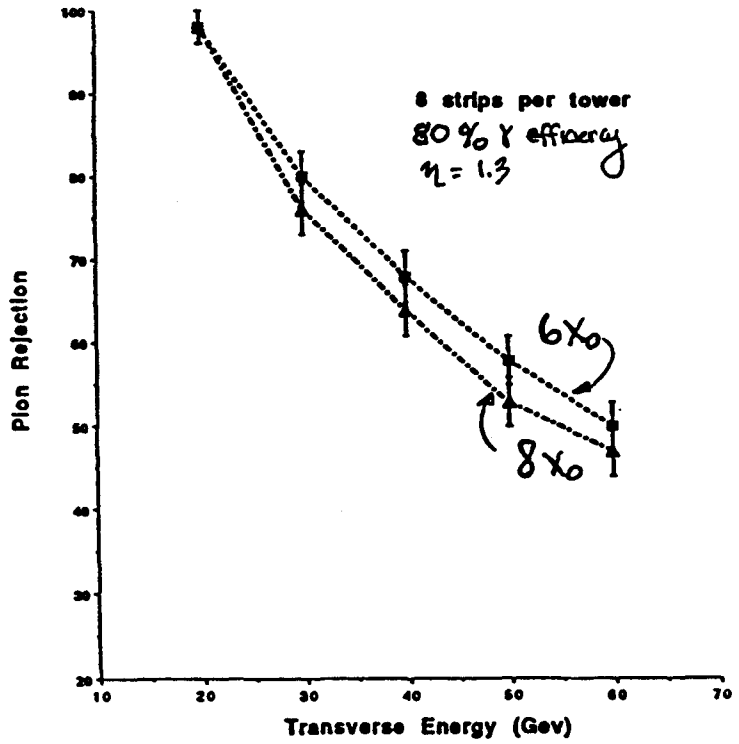

Fig.3-6. Probability of detecting a single photon as a function of P_t. The two curves are for a shower maximum detector at 6.0 and 8.0 X_o, respectively [3-3].

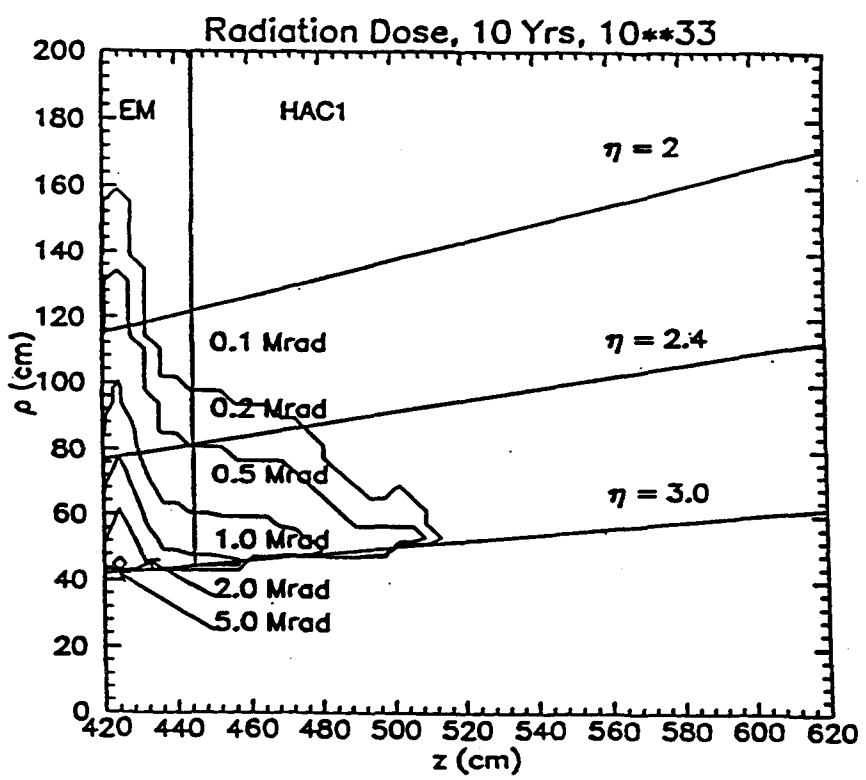

Fig.3-7. Contour plots of radiation dose in the ECEM and hadron compartments. The horizontal axis is the distance from the interaction region in meters, and the vertical axis is the radius measured from the beam line. The dose is calculated for 10 years of running at $10^{33} cm^{-2} sec^{-1}$.

lengths deep into the EM calorimeter. For any given angle with respect to the interaction point, the maximum radiation dose in the hadronic calorimeter is about 4 times less, and is greatest at the front of the hadron calorimeter. Over the surface of the calorimeter, the maximum radiation dose varies as $sin^{-3}\theta$ or about a factor of 100, from 5 Mrad at $|\eta| = 3$ to 50 Krad at $|\eta| = 1.4$, after 10 years of running at a luminosity of $10^{33} cm^{-2} sec^{-1}$. Hence, the sections of the calorimeter closest to the beam line receive the by far highest dose, and the total volume of the calorimeter receiving a high dose is relatively small.

The sensitivity of plastic scintillator and fibers to radiation damage has been measured, and is shown in Fig. 3-8. After about 1 Mrad of radiation, the scintillator tile/fiber combinations have lost about 35% of their total light yield. This result is for scintillating tiles made from SCSN81 [3-5], BCF91A wave length shifting fiber and BCF98 clear readout fibers [3-6]. Comparing the maximum radiation dose from Fig. 3-7, and the light output from Fig. 3-8, it is reasonable to conclude that the scintillator in the electromagnetic calorimeter for $|\eta| > 2$ near EM shower maximum will need replacement during the lifetime of the detector, particularly if the accelerator exceeds its design luminosity.

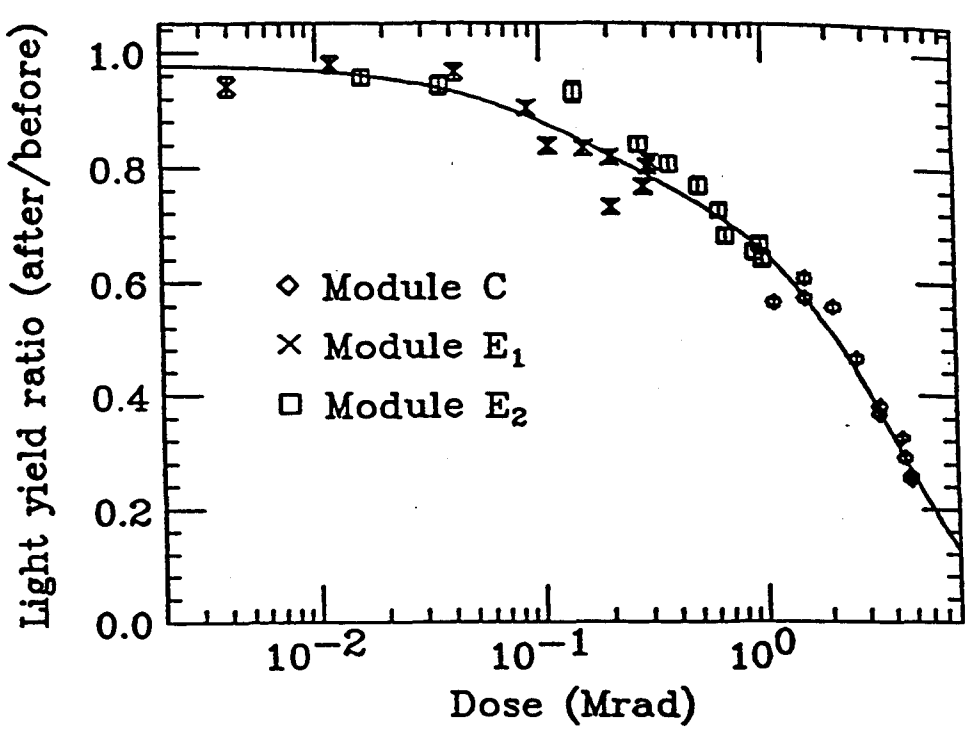

Fig.3-8, Relative light loss in scintillating tile/fiber combinations as a function of Radiation damage. The scintillator used here was SCSN 81 with BCF91a WLS fibers[2-1]

We see several reasons why a segregated, rebuildable section for the ECEM should be integrated into the baseline design:

- Damage to the calorimeter: The volume of damaged scintillator is expected to be relatively small. About 20% of the total number of tiles will require replacement. It seems reckless to tear down all of the endcap calorimeter so that only 20% of it can be refurbished. During such a procedure the potential for damaging the part of the calorimeter system not needing replacement is high.
- Collateral damage: Removal of all the scintillators from the endcap calorimeter (as in the baseline design) implies removal of all of the infrastructure from the calorimeter surface: electronics, PMT's, cooling systems, experimental (400 Hz) power, equipment (60 Hz) power, high voltage and signal cables, trigger hardware, source systems, fire protection and other safety systems, as well as those pieces of other subsystems that rely on the endcap for mechanical support or experimental utilities distributed from the endcap. Given the large number and variety of systems supported by to the endcap, it is possible that a complete disassembly of the endcap calorimeter will cause significant damage or disruption to other systems.
- Schedule: The time needed for replacement of the damaged scintillator can be minimized by thorough preparation of the new scintillator and tile assemblies prior to the removal of the ECEM. In the TDR baseline system of 32 wedge based modules covering the entire endcap electromagnetic calorimeter, the schedule would also have to include time for removal and eventual reinstallation of all the other systems, detector utilities and cables.
- Cost: With a rebuildable section of the ECEM, costs are mainly restricted to replacement of the damaged scintillator, without involving the undamaged portion of the calorimeter or ancillary systems. A design requiring removal of all the scintillator needs to include not only the cost of the scintillator replacement, but of the disassembly of and reinstallation of all other affected systems.

For these reasons we conclude that the design for the ECEM calorimeter should include an accessible, rebuildable core, and in the following we describe a mechanical design for the ECEM having this feature.

3.7. Physics Performance References

[3-1] Julia Yarba, Calorimeter Group Meeting, SSCL meeting, October 22, 1992.

[3-2] SDC Detector Parameters, SSCL Doc Nr.: SDT-000010, September 14, 1992.

[3-3] A. Maghakian, P. Melese and R. Rusack, γ/π^o Separation using the SDC Shower Maximum Detector, SDC note 92-353, 1992.

[3-4] R. W. Kadel, "Radiation Dose Profiles and Activation of the SDC Endcap Calorimeter, SDC-92-176, (1992)

[3-5] SCSN 81 is a scintillator produced by Kuraray International, 200 Park Ave, NY, NY 10166.

[3-6] BCF91a and BCF98 fibers are produced by Bicron Corporation, 12345 Kingsman Rd., Newbury, Ohio, 44065

4. Mechanical Structure

Mechanically, the endcap EM calorimeter differs from the barrel EM calorimeter in one important respect: the lead absorber planes are vertical. The mechanical support of vertical lead plates is a fundamentally different (and somewhat easier) problem than that faced in the barrel EM calorimeter. We have chosen to look at the design from a fresh prospective, with the intent of removing as much inert material as possible and eliminating cracks between towers while still meeting the physics goals.

4.1. Basic Structure

The monolithic design with fiber routing between scintillator layers is conceptually represented in Fig. 4-1.

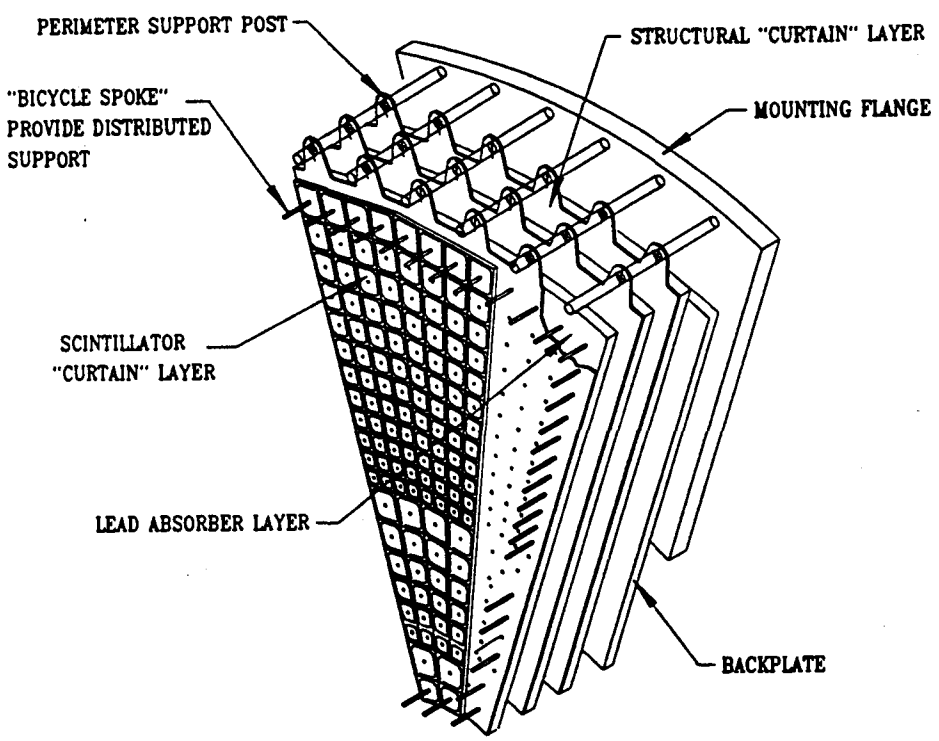

BASIC MECHANICAL STRUCTURE

Fig.4-1. Exploded view of a section of the assembled endcap showing the relative location of the perimeter posts, sheet metal curtains, lead, spokes and scintillator tiles.

In this design, the lead plate absorber layers are continuous, except for joints dictated by material size limitations. The layers of edge to edge scintillating tiles are essentially continuous, with no significant ϕ or η cracks. Support of both absorber and scintillator

is via slender, penetrating axial "bicycle spokes" used in shear, with no compressive force on the tiles. The spokes themselves are supported by interleaving, thin sheet metal disks ("curtains") which are in turn hung from low mass supports at the perimeter. Thus, the weight of absorber and scintillator layers is transferred to these structural "curtains" via the penetrating bicycle spokes, and the load on the curtains is transferred to the perimeter structure, which is hidden behind the last towers of the barrel EM calorimeter.

Support of the lead absorber by the bicycle spokes is made feasible by the use of rolled calcium-tin lead alloy plate (0.065% Ca, 1.3% Sn), which has much better creep properties than conventional antimonial lead. For example, if a single horizontal 1.5 *mm* bicycle spoke supports a 10 *cm* x 10 *cm* area of 6 *mm* lead in the vertical plane, the bearing stress at the spoke is only about 0.73 MPa (106 psi). Although further verification is being obtained in small scale tests, we are confident that this small, localized stress will cause only a very minor creep distortion in this alloy over the life of the calorimeter. It should be noted that spoke tension and interlayer friction is not being relied upon for support of any of the components. Figure 4-2 shows how the support system works. The axial spokes in shear transmit the weight of the lead absorber and the tiles to the sheet metal layers. The span of each spoke beam segment is very short (12 *mm*, the distance between sheet metal curtain layers). The small, shouldered spacer bushings prevent spoke tension from bearing on the scintillator tiles. Overall, the spokes originate through holes on the front plate and terminate in an equivalent set of holes in a floating "spoke" plate at the rear of the calorimeter. The spokes are under only modest tension to keep the stack together axially. Tension is applied via small nuts on either end of the spoke.

At the locations where spokes pass through the scintillator tiles, small, shouldered, aluminum bushings are used to protect the tiles from mechanical stress, and to provide space next to the scintillator layers for direct radial routing of fibers and source tubes. Routing the fibers in a gap adjacent to the tile faces allows for flexibility in the location of the fiber exit from the tile. When the fiber groove is NC machined in a tile, the fiber exit groove can be simultaneously cut in an "S-bend" that eases the transition of the fiber out of the tile into the fiber routing gap. The fiber exit groove is illustrated in Fig. 4-3. There is no need to notch the edge of the tile to create an exit channel for the fibers. With this feature, the overall design becomes hermetic. The layout of tiles, bushing and fiber routing paths is shown in

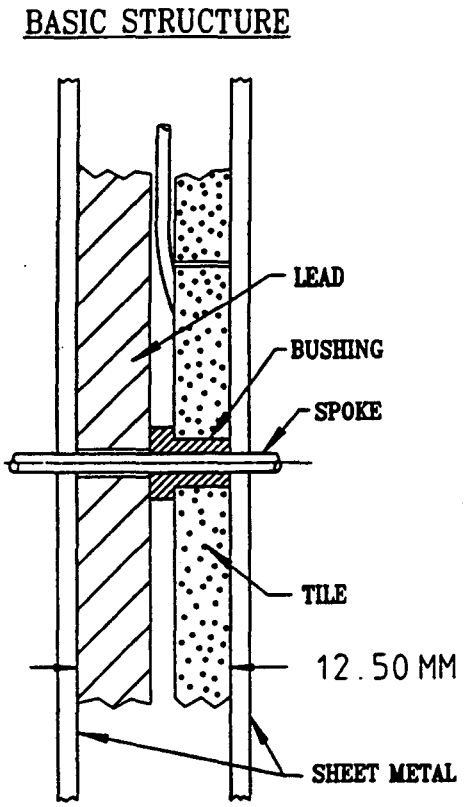

Fig.4-2. Detailed drawing of a spoke penetrating the Pb, scintillator and aluminum curtains. The load bearing function of the spoke is to carry the weight of the Pb to its local sheet metal curtain. calorimeter showing 1/32 of the circumference. See text for explanation.

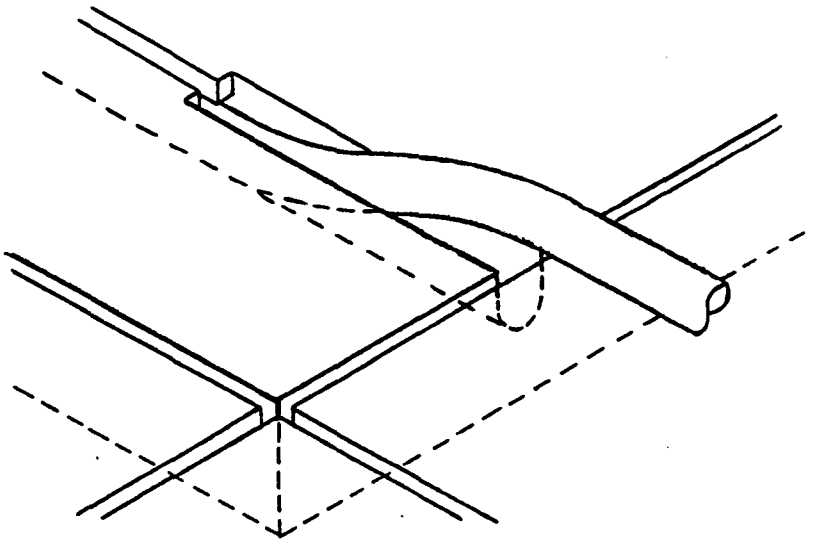

Fig.4-3. Expanded view of a scintillator tile showing the "S-bend" exit groove to ease the exit of the WLS fiber from the tile.

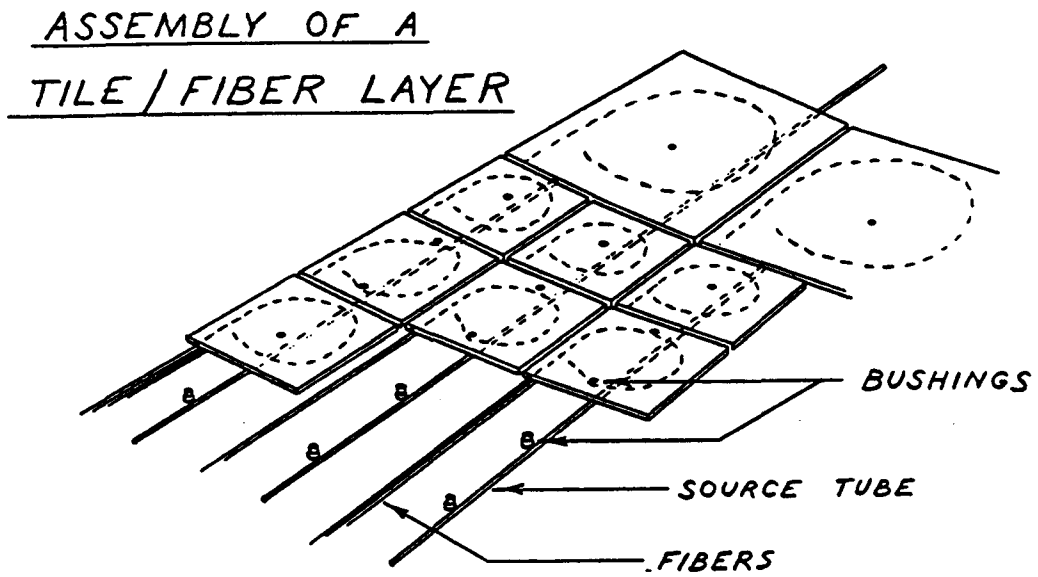

Fig.4-4. Three dimensional view of a single scintillator tile layer during assembly, showing the location of tiles, spokes, bushings and the fiber routing gap.

Fig. 4-4. Figure 4-5 shows an overall view of the completed ECEM. The segmentation of a single tile layer is shown in Fig. 4-6.

4.2. Tile Options

For the production of scintillating tiles, we hope to rely on our Japanese collaborators. The current baseline design is as follows:

Although the lead and aluminum layers are continuous, the scintillator tiles are individual, wrapped with Tyvek or mylar, and assembled into the usual projective towers. Edge gaps are minimized subject to assembly tolerances (0.65 *mm* is a reasonable target). For better structure, simplicity, and non-projectivity, the bicycle spokes are axial. The spoke pattern is designed so that one or two spokes intercept each scintillator tile, at locations which are unique to each tile size and shape. The 20 ring x 23 layer projective tower geometry already commits us to no less than 460 tile shapes (not counting shower maximum, layers); each of these shapes will include one or two 4.0 *mm* spoke holes. *There is no increase in the number of different tiles in our design.* Adhesives are not used anywhere in the structure, as the penetrating spokes fix the tile and absorber locations.

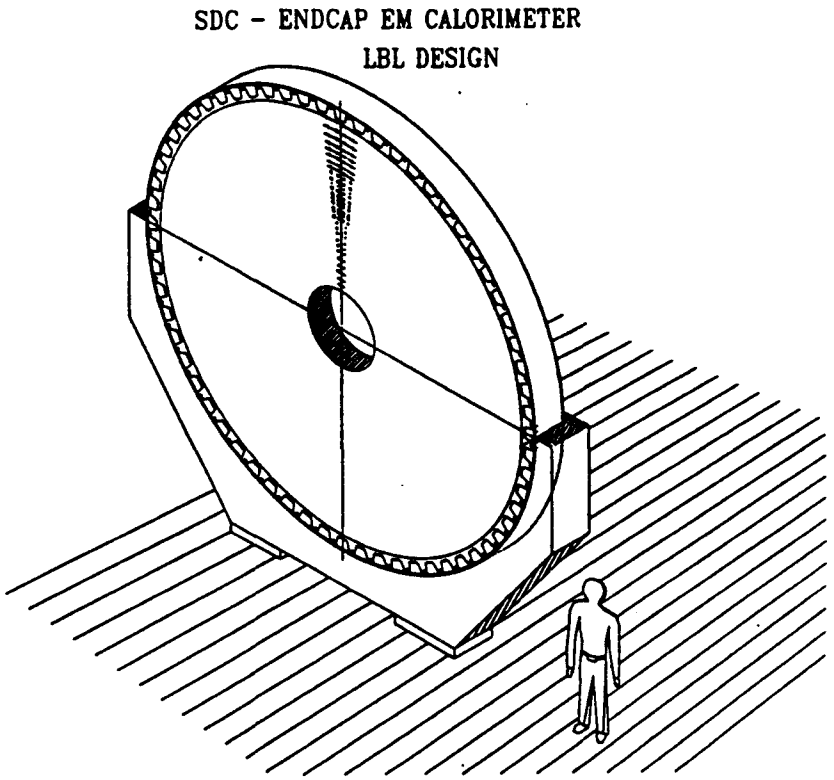

Fig.4-5. Perspective view of one endcap calorimeter module. Visible at the outer perimeter are the access holes for attaching the fiber disconnects. Light tight covers have been removed.

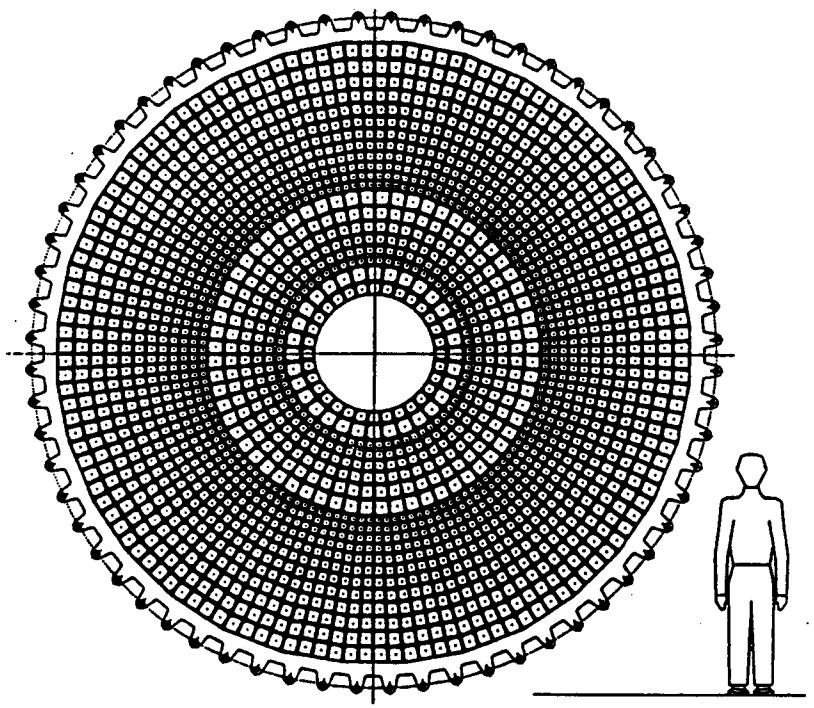

Fig.4-6. Segmentation of the scintillator layers into towers for one plane of the ECEM. Also shown are the ears for attaching to the 64 perimeter posts.

In the baseline design, a wave length shifting (WLS) fiber is inserted into a keyhole cross-section, sigma pattern groove in each tile. Soon after exiting the tile into the fiber routing layer, the WLS fiber is permanently spliced to a more radiation-hard silica fiber. The silica fiber is routed radially outward to a mass termination connector mounted in the perimeter structure, where it is coupled to a clear plastic fiber that carries the light signal out to the "cookie" of a PMT mounted outside the magnet flux return iron.

The monolithic design allows several options for tiles and fibers. For example, there is enough room in the fiber layers to accommodate two fibers per tile either with mirrored ends or a single fiber in a "U" pattern. White painted or mirrored tiles could be used to eliminate wrapping. Saw-cut "multi-tiles" have the potential to make the edge gaps more uniform and reduce the number of spokes required. The layered construction of the ECEM allows these optical components to be somewhat independent of the mechanical structure and optical and production R & D can continue for some time without affecting the mechanical design.

4.3. Perimeter Structure

The minimal structure in the active volume of the ECEM is made possible by concentrating most of the mechanical structure at the perimeter. Fortunately, this perimeter structure can be "hidden" behind the last towers of the barrel EM calorimeter, thus providing continuous EM coverage. The relation of the perimeter structure to the barrel and endcap calorimeters is shown in Fig. 4-7.

The design objective is to confine the low mass, non-projective ECEM perimeter structure to a sacrificial volume in hadronic towers 27/28 only. The current design achieves this goal. This perimeter structure, shown in Fig. 4-8, is a busy place, with functions that include:

- support of the 23 sheet metal curtains.
- access to mounting points on the face of the hadronic end cap
- Sixty-four mass terminated silica-to-plastic fiber connector assemblies.
- space for routing of the radial fibers (and source tubes) to the vertical gap between the barrel and endcap with sufficiently large bend radii for the fibers.
- light shielding of tile edges and exposed fibers.

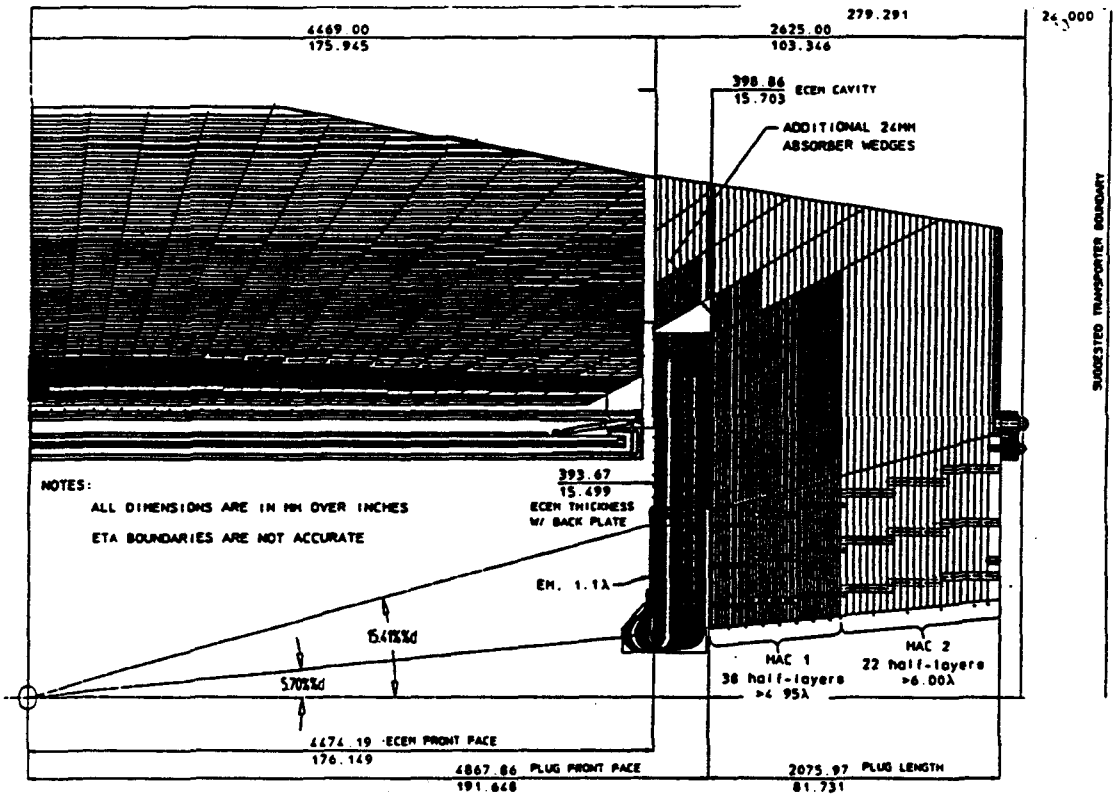

Fig.4-7. Side view of the barrel and endcap calorimeter showing the location of the perimeter supports in hadron tower 28.

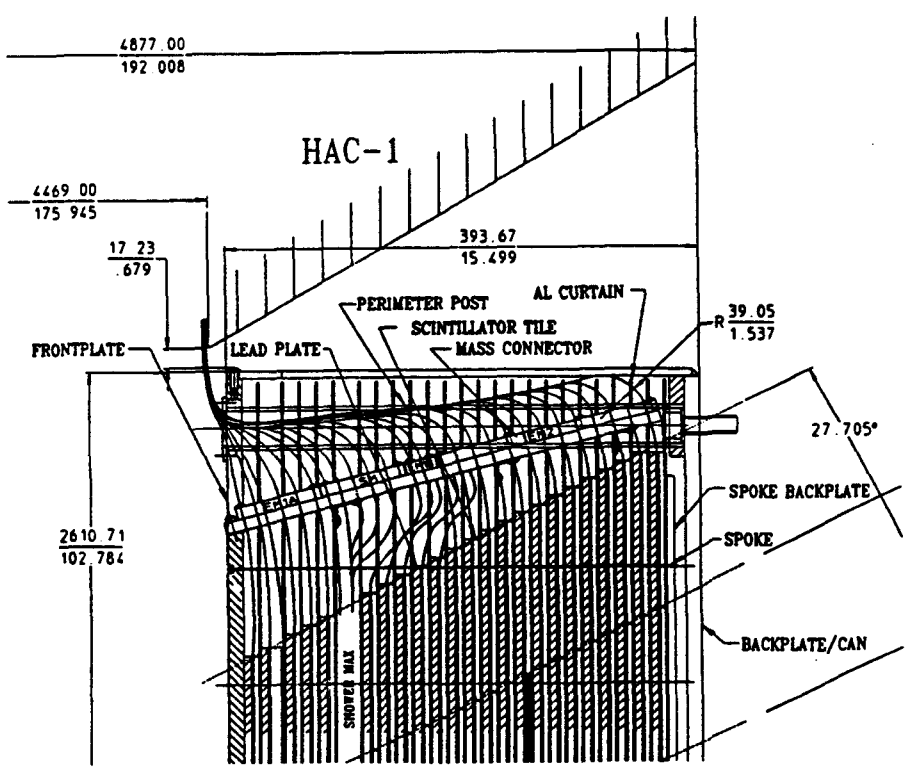

Fig.4-8. Drawing showing the details of the perimeter of the ECEM including the perimeter posts and fiber mass disconnects.

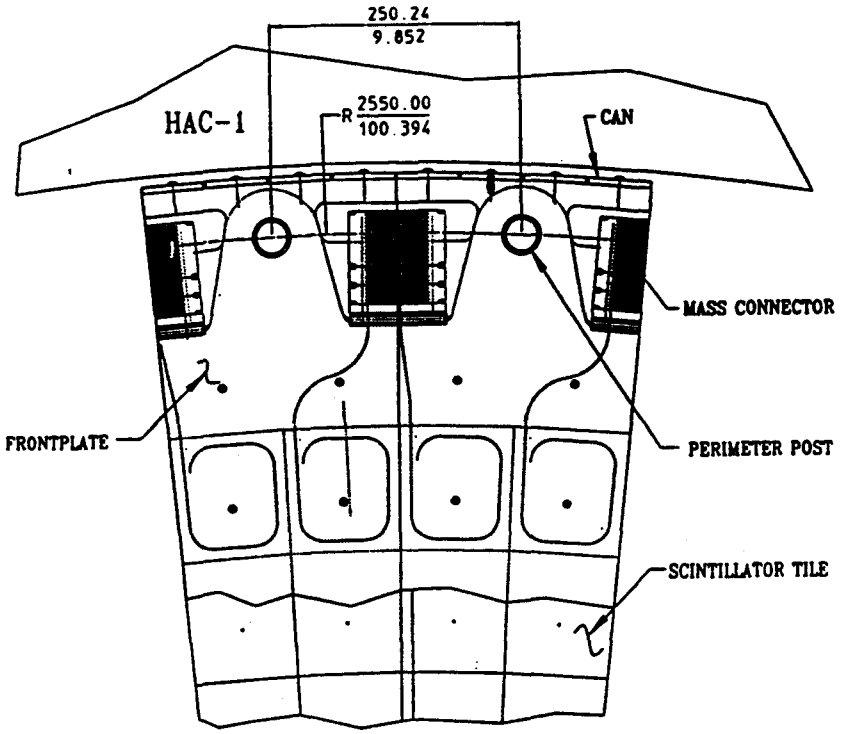

Fig.4-9. Front view of the perimeter showing the relation of perimeter posts and the mass termination for the fibers. The mass termination is extremely foreshortened in this view.

- provision for lifting fixture attachment.

Figure 4-9 shows a front view of the perimeter structure. The size of the mass connector for the fibers is extremely for-shortened in this view. The mass terminating connector has obvious advantages for assembly, handling, shipping, installation and removal. It is recognized that these connectors require development. If necessary, the fibers could be continuous from tiles to PMT's. A well designed means of protecting coiled fiber assemblies during shipping and installation would then be necessary.

The main elements of the mechanical support are the sheet metal curtains, the 64 perimeter posts, the front plate, the back plate and the outer, cylindrical surface of the ECEM. Structurally, the perimeter support design relies on the natural rigidity of this short cylindrical shell, or "can". Gravitational loads are supported as follows: at the rear circumference of the 5.3 m diameter ECEM, the backplate of the "can" is bolted to the heavy steel absorber face of the hadronic calorimeter behind it. Sockets in this backplate support the rear ends of 64 axial perimeter posts. The cylindrical shell is welded to this backplate, and it in turn

Table 4-1 : Material thickness in the ECEM support system.

Element	Thickness	Rationale
Backplate Frontplate	13 *mm* Al	Resistance to compressive buckling loads when supported from the opposite end
Cylindrical Shell	6 *mm* Al	Stresses are low. Bolting and welding considerations predominate.
Perimeter Posts	38 *mm* dia, 3 *mm* wall Al tube	30,000 psi (207 MPascals) stress, 2 *mm* maximum deflection
Curtain Layers	1.5 *mm* Al (1.0 *mm* SS)	Tensile stresses are low. Sized for buckling of 3 O'clock "ears" and screw threads
Backplate Socket Reinforcement Frontplate Socket Reinforcement	13 *mm* Al	Sized for adequate perimeter post bearing area
Spokes	1.5 *mm* Titanium	21,000 psi (145 MPascals) tensile stress when tilted for test beam calibration
Bushings	4 *mm* dia Al (in scintillator)	Sized to limit compressive load at curtain holes during assembly
Rear spoke plate	6 *mm* Al	Rigidity needed to spread spoke loads when tilted for test beam calibration

supports the frontplate, which contains similar sockets for support of the front ends of the 64 perimeter posts. The key structural feature of this design is that it is the cylinder walls acting in shear at the 3 o'clock and 9 o'clock regions that support the frontplate. The frontplate lies in a vertical plane, and carries only vertical loads. Buckling tendencies in the frontplate are resisted by the stiffness provided by the joint with the cylindrical shell. The entire structure will be 6061-T6 aluminum to minimize particle absorption, and to avoid magnetic forces. Finite element analysis is underway for this design. Our preliminary calculations and design considerations indicate the member sizes shown in Table 4-1. We note here that most of the support structure is made from aluminum. We are considering the use of stainless steel supports in order to minimize forces during quenches of the solenoid magnet. The thickness of the support members would be correspondingly thinned to reflect the greater strength of stainless steel over aluminum.

4.4. Calibration Source Tubes

Both the radiation dose and the magnetic field in the endcap are rapidly changing in r and z. The relative radiation doses over the ECEM have already been discussed. Variations of 8% [4-1] in light yield have been measured for scintillators under the influence of magnetic fields up to 2T. For these two reasons we have provided a source tube for every tile in the calorimeter so that its response can be measured in presence of the magnetic field of the solenoid. All source tubes are remotely accessible even with the endcaps closed.

Additionally, the source tubes are routed in the same way as the optical fibers, and for space considerations, the source tubes and fibers share the same disconnect and light-tighting system. There is little room to add a second independent system for the source tubes alone. Due to the geometry of the endcap, source tubes that terminate inside the ECEM boundary would be inaccessible after installation of the ECEM inside the endcap hadron calorimeter.

The source tubes consist of thin wall ($\approx 0.25\ mm$) stainless steel tubes located in the 2 mm wide fiber routing gap, arranged in a radial pattern similar to the optical fibers. The ECEM tower segmentation requires 128 radial tubes per tile layer to provide centerline coverage for all tiles. We hope to use outer tubes made of a flexible, helical spring type material, with funnel joints at the mass-termination connectors in the perimeter structure. Source tubes will be handled very much like fibers, with spring clips to lightly load them against the tiles at the tile centers. Clips on the bicycle spokes can used to align the source tubes with the center of the tiles in the ϕ coordinate. We have surveyed radioactive sources for calibrating the ECEM in reference [4-2]. The best choices for the ECEM are Barium 133 and Rhodium 101.

4.5. Shower Maximum Layers

The ECEM shower maximum (SM) system will be designed, built and tested at Saclay. Self-contained wedge assemblies of a manageable size will be built into the ECEM after the fifth EM layer is completed. Location and support of the SM assemblies will be via the penetrating spokes. It has been agreed that exact spoke locations throughout the ECEM will be determined by the SM layers, so that all spokes will pass through cracks in the 8 x 8 SM segmentation of the EM tower apertures. In this way, there will be no interference

between spokes and SM fiber grooves.

4.6. Barrel/Endcap Overlap

Viewed from along the beam line, the boundary of the barrel EM calorimeter is a 32-sided figure. It is our intention that the tiles at the $|\eta| = 1.4$ boundary of the ECEM "overlap" the barrel EM calorimeter by ≈ 2 *cm*, so that showers that develop near the end of the barrel are captured in the ECEM. Hence, the outer boundary of a tile layer in the ECEM is also a 32-sided figure. Note that we accomplish the overlap by extending the existing, outermost row of tiles another 2 *cm* from their nominal tower edge. We do not add an extra set of towers.

4.7. Light-tighting System

Although many details of the ECEM light-tighting system remain to be worked out, a general concept is in place. Scintillating tile edges at the inner and outer radii are the most vulnerable points for light leaks. Hence, the entire ECEM "can" structure must be light-tight. This light-tight volume will be extended all the way to the PMT's mounted at the outside radius of the endcap. We expect to do this with molded, "zippered", fiber conduits of rubber-like plastic. A rough sketch of this concept is shown in Fig. 4-10.

These conduits will be installed around bundles of fibers emanating radially from the perimeter of the ECEM (a relatively low radiation zone). They will be designed for a rubber grommet type of fit in the fiber ports of the ECEM frontplate, and the PMT mounting boxes. The "zipper" is envisioned as a scaled up zip-lock bag type of linear joint. This system appears to be feasible, but it clearly needs further development and collaboration with potential vendors. The light-tighting system will be refined over the coming year.

4.8. Tolerances and Manufacturing Techniques

Mechanical tolerances will be very important in this close-fitting layer cake assembly of over 50,000 pieces. However, to keep costs in line, only conventional, routine tolerances will be used. Numerically controlled (NC) machining will be heavily relied upon for the many repetitive parts in the design. Match drilling (drilling of many layers at once) will also be

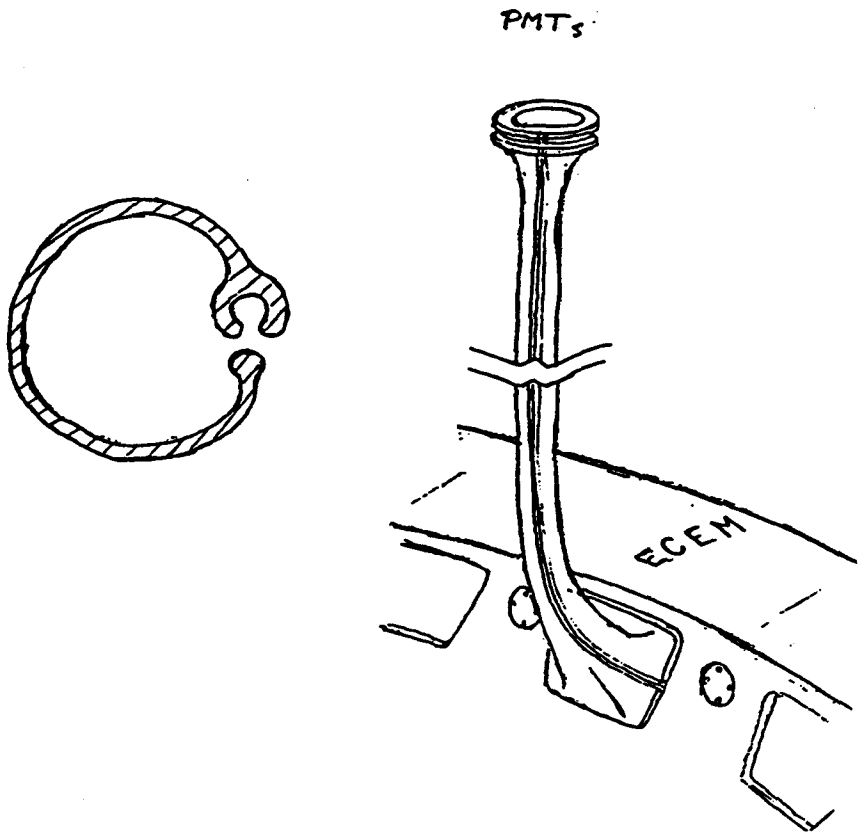

Fig.4-10. Schematic diagram of the flexible, "zippered" enclosures used to keep the readout fibers light tight.

used to guarantee good alignment of spoke holes in the sheet metal curtains. As detailed below, nine individual tolerances combine to dictate a workable tile edge gap. We expect to achieve an average edge gap of 0.65 *mm*.

4.8.1. Curtains

The very large (5.2 m dia.) 1.5 *mm* thick curtain disks (Fig. 4-11) are one of the most demanding components in the design. They must be reasonably flat, with close tolerances on the perimeter post hole locations and on the 3000 spoke holes, which must align with those in the next curtain. Unfortunately, 5.2 m wide rolled sheet is not available, and we are researching minimum distortion butt welding techniques with various vendors. The travel of NC machining tables are not large enough to machine an entire curtain disk in one setup, so a careful indexing scheme is needed. The tolerances we are seeking over these distances will require machining in a temperature controlled environment. Match drilling of spoke holes for many layers at once will give additional assurance that spoke insertion will not be a problem during assembly. In seeking budgetary quotes for these curtains, we have had encouraging discussions of manufacturing techniques with several vendors. It is a challenging component

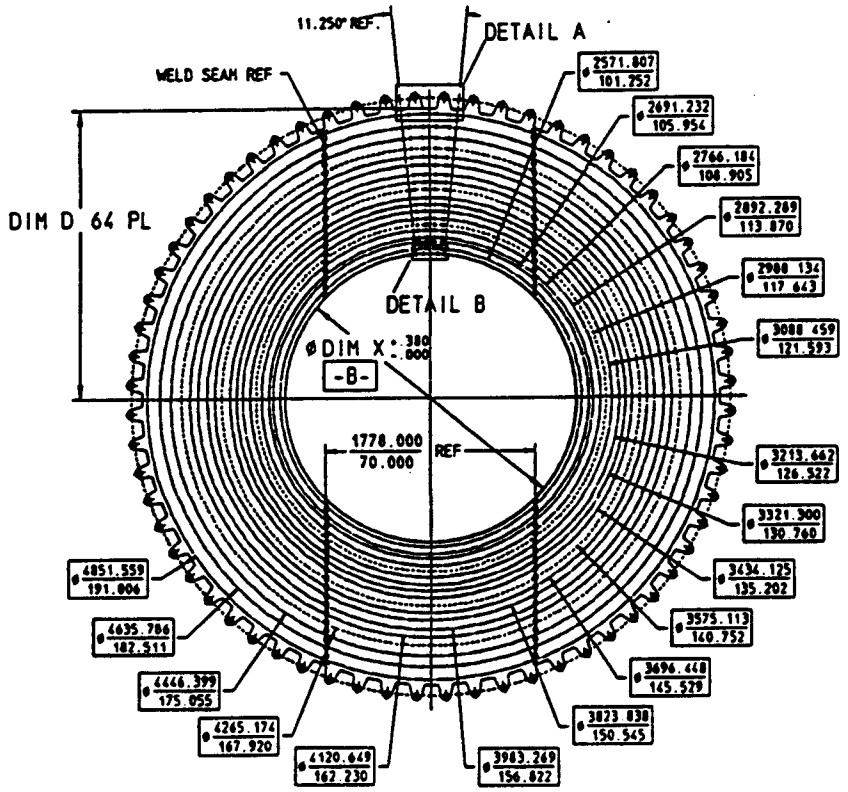

Fig.4-11. Mechanical drawing of one of the 22 identical curtains in the ECEM.

and requires know-how and ingenuity on the part of the successful vendor.

4.8.2. Absorber

The 6 *mm* calcium-tin lead alloy plate will be rolled to our specifications, and will be cut into rectangular blanks by the vendor. To help assure spoke hole pattern alignment, the lead will be machined at the same temperature as the aluminum curtains. Figure 4-12 is a drawing of one wedge or sector of an absorber plate. The distributed support provided by the spoke system gives us freedom to segment the lead for convenience in handling. Our current plan is to divide a typical lead layer into $2\pi/16$ pie slices, with another division at the $|\eta| = 2.0$ boundary. We expect the lead edge gaps to average 0.5 *mm* wide, and a 1/32 wedge staggering pattern would result in these projective gaps occurring only in every other layer. If necessary, the projective alignment of the edge gaps can be further reduced with additional variations on the pie slice dislocation. The spoke holes through the lead absorber layers will be slightly larger than those in the aluminum curtains (2.3 *mm* versus 1.6 *mm*). This is done to facilitate spoke insertion through the layered structure.

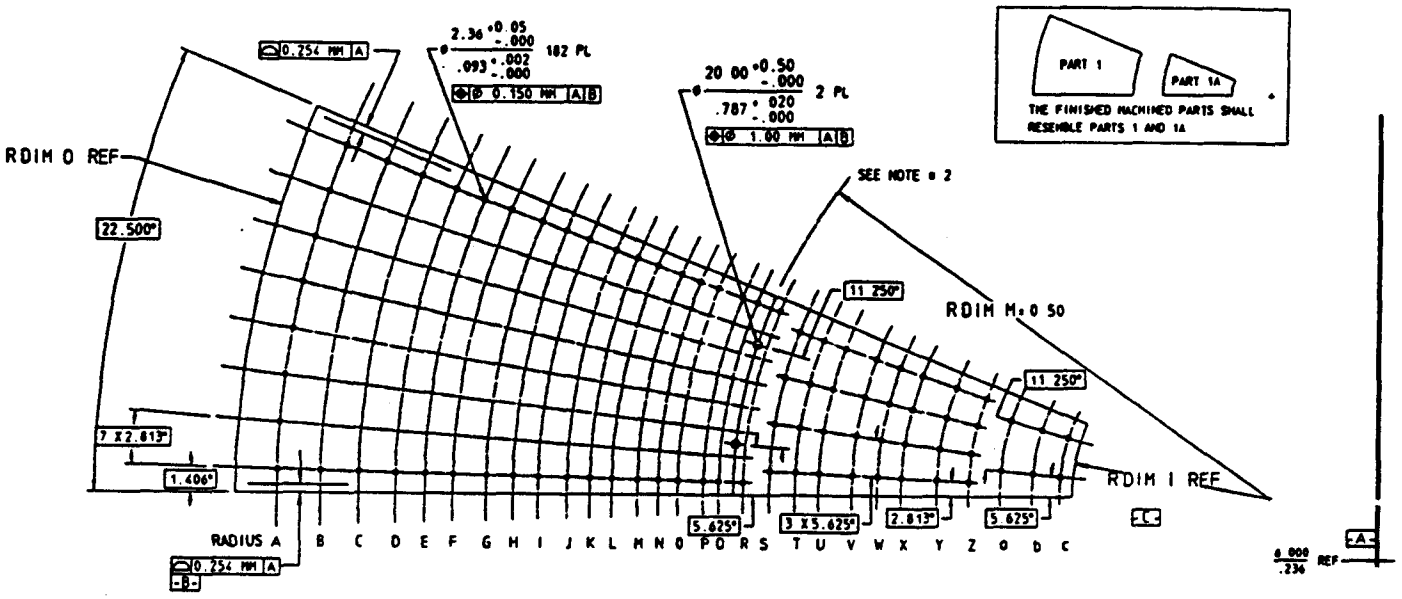

Fig.4-12. Mechanical drawing of one of the absorber plates. The wedge shaped pieces are combined into a 32-sided object to form one layer of ECEM absorber. Note that all the Pb plates are identical, except for the outer/inner boundary.

4.8.3. Tile Gaps and Tolerance Buildup

Our objective is to minimize the tile edge gaps without risking tile to tile interference, which would be extremely disruptive for the assembly process. The individual tolerances which affect the tile edge gaps are shown in Fig. 4-13.

The tolerances noted are achievable and reasonable, in our judgement. When the nine tolerances involved are simply added, the "very worst case" net tolerance on the "half gap" is +425 μm, which implies a design gap width of 850 μm, or .034 inches. If one assumes the various tolerances represent normal distributions, the tolerances added in quadrature result in a design gap of only 300 μm, or .012 inch. Since many of the tolerance deviations will be systematic, reality should lie somewhere between these two extremes. Beyond theory, experience on large, one of a kind projects shows that is is not uncommon to somehow end up with "only slightly out of tolerance, but still useable" parts, as a result of schedule and cost pressures. For these reasons, we have set the design edge gap at 650 μm, or .026 inch, plus reflective wrapping thickness. It should be noted that this represents the average edge gap; individual gaps could vary from zero to twice this amount.

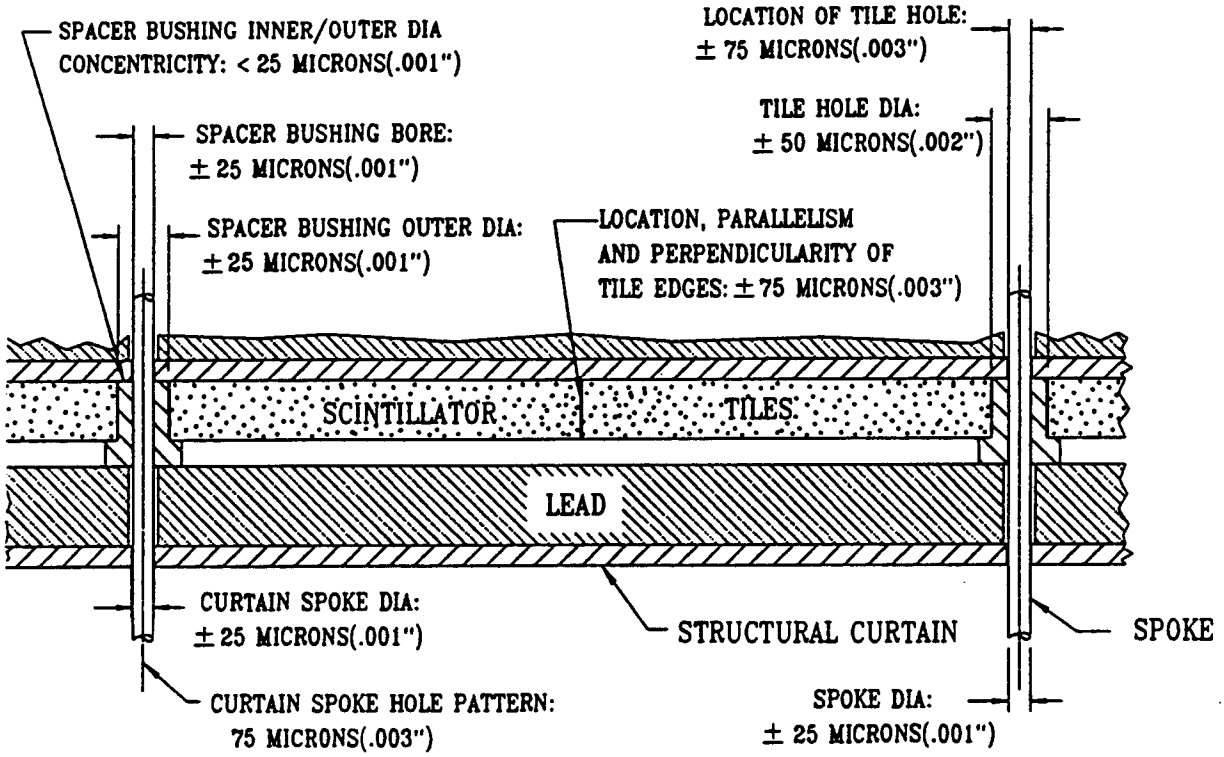

Fig.4-13. Figure indicating the 9 tolerances that combine to determine the tile to tile edge gaps.

Considerable scope for development remains in the design and manufacturing of the scintillator tiles. Many of the challenges are common to the entire calorimeter, but special requirements on radiation damage and tight dimensional tolerances are especially relevant to the ECEM (and the shower maximum detector). Although our baseline design uses individually wrapped tiles, the monolithic ECEM approach allows great flexibility in accommodating scintillator variations. For example, epoxy filled saw-slit "multi-tiles" are an attractive proposition for minimizing edge gaps. In this design, many tiles, optically insulated, are contained in a single, large sheet of scintillator. Tighter control of tile edge gaps is a primary motive for the development of "multi-tiles". However, optical cross-talk and suitable reflective wrapping methods are still being studied. A variation on this scheme has also been suggested: NC machining of spoke holes and fiber grooves on a large sheet of scintillator plate (with inherently good tolerances on spoke to spoke locations), followed by a final saw-slitting into separate individual tiles. With faithful tracking of each tile to its original location, the scintillators will reassemble in the ECEM with most edge gaps of only a saw kerf. In Fig. 4-14 we illustrate the segmentation of the scintillator in this case. The drawing also applies to multi-tiles.

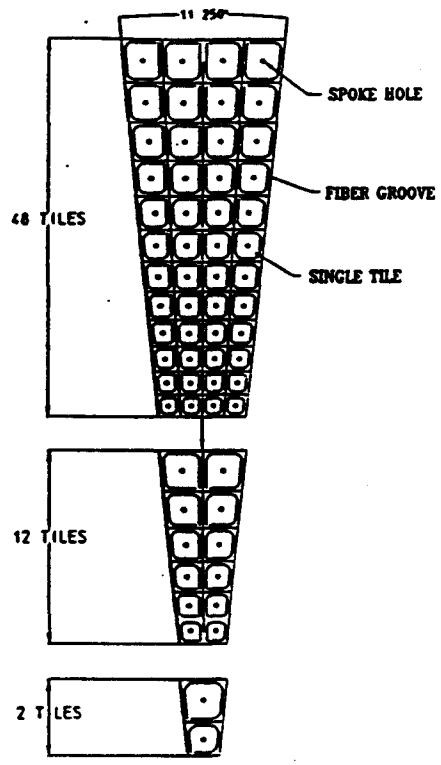

Fig.4-14. Segmentation of $\frac{1}{32}$ of the scintillator tiles. The drawing indicates how the tiles could be saw cut from a single sheets of scintillator. In the event that "multi-tiles" are used, this segment would be broken into 3 "multi-tiles" as indicted.

4.9. Assembly

The 5.1 m diameter monolithic ECEM will be assembled lying flat on its frontplate, with its 64 perimeter posts in place for locating the aluminum curtain layers. The stacking order is lead, fibers (and source tubes), tiles, curtain. Fibers are located below the tiles so the presence of the scintillator traps the fibers below in the fiber routing gap.

The assembly begins by advancing the bicycle spokes about 6 *mm* out of the front plate. We then lay down the bushings for the first layer and attach the source tubes to them. The source tubes are routed radially to the disconnect at the outer diameter of the ECEM. Spliced fiber assemblies are made up and tested remotely. Sorted, pre-tested tile-fiber assemblies (or possibly multi-tiles) are individually installed on their locating spokes, working from the inside to the outside diameter. Each fiber is routed radially outward, avoiding spokes, to a predetermined hole in a connector plate in the perimeter structure. The silica fibers have been pre-polished to length. If needed, up to eight assembly technicians could work simultaneously around the perimeter of the ECEM to install a layer of scintillator tiles.

As each new layer is positioned, the bicycle spokes and perimeter posts are advanced upward to engage the next layer. Each scintillator layer can be optically tested before it is buried by the following layers. This is accomplished by lowering a dark box over the entire assembly. It is foreseen that a photodetector will be used to read out each individual tile and the source driver system will be employed to drive a source past each tile to verify its correct installation and record its light yield.

When the stacking of the 22 layers is complete, the 6 *mm* inch thick aluminum spoke plate is added, and the titanium spokes are moderately tensioned using threaded nuts (size M1.6 x 0.35). The cylindrical "can" with backplate is then lowered over the assembly, and the rear ends of the 64 perimeter posts are advanced into their sockets. Radial bolting of the can to the frontplate completes the structural assembly. Radial bolting is used here because there is no room for a conventional flange with axial bolts. Slotting the can edge for some radial flexibility will allow a tight structural joint with radial bolts. Instead of large diameter, heavy bolts, we have used numerous, relatively small fasteners to maintain a uniform mass distribution. Finally, various light-tighting covers and seals are added and tested, and a suitable fixture is used for up-ending the finished ECEM. A cross section of the completed ECEM in the assembly position is shown in Fig. 4-15.

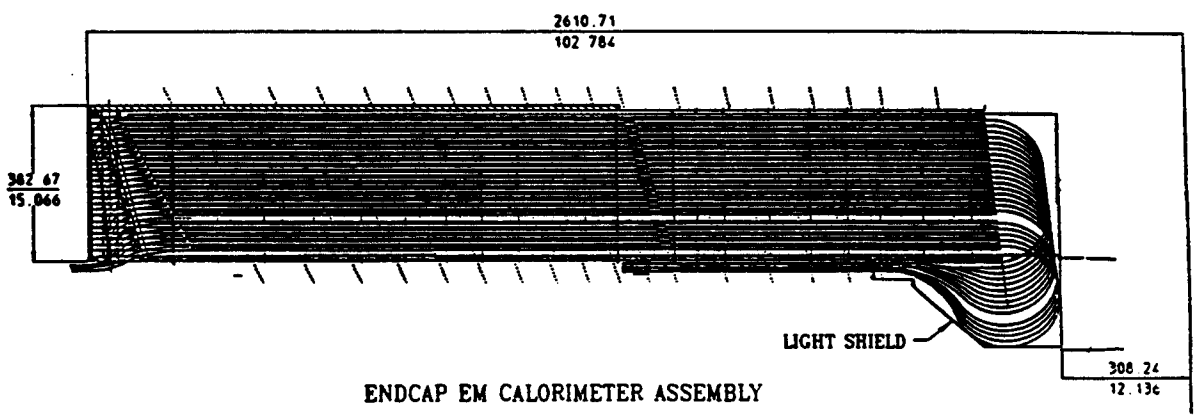

Fig.4-15. Cross-section of the calorimeter showing overall dimensions.

Relatively high compressive stresses will be present in the lead during assembly in the horizontal plane. If a single 6.0 *mm* OD bushing shoulder is used to support a 10 *cm* x 10 *cm* lead area, the 23 layer stack will exert a concentrated stress of about 6.1 MPa(890 psi) at the lowest layer bushing contact area when the assembly is completed. Although the Ca-Sn

alloy has a yield strength of over 48 MPa (7000 psi), minor creep may take place during this time. This creep rate is now being tested.

4.10. Shipping and Handling at SSCL

The 5.3 m (17.5') diameter monolithic ECEM is a moderate challenge for shipping. With a special fixture, a "wide load" permit will be required. The 30 ton weight is not a significant shipping limitation. Rail is also a candidate for long distance shipping, although accelerations are a concern. Wayne Elliot at SSCL has looked at shipping limitations for the design, and advises that this device can be moved, and that none of the state regulations involved will be difficult to satisfy.

At the SSCL, various manipulations of the ECEMs will be required for testing, beamline calibration, and installation. The expected sequence of operations is given in Appendix A.

4.11. Beamline Calibration

Of particular note is the potential requirement for beamline calibration of some or all of the almost 4000 channels of output in each ECEM. Since we want to maintain the vertical orientation of the ECEM structure (no rotation about the Z axis) to avoid mechanical shifting of the various layers, and to simulate particles coming from the interaction point, the entire 30 ton monolithic assembly must be tilted at angles of up to ± 28 degrees (corresponding to $|\eta| = 1.4$) from the horizontal beamline beamline. This requirement is somewhat taxing for the ECEM structure, which has been minimized on the assumption of a vertical operating orientation. However, with high strength titanium spokes and a test fixture which offers distributed, low mass, support across the front face of the ECEM, the structure will be safe at angles of up to 28 degrees.

4.12. Rebuildable Inner Core

Radiation damage profiles have been shown in Fig. 3-7. The most intense radiation fluxes in the calorimeter are located in a small volume in the EM shower maximum layers of the ECEM at $|\eta|$=3.0. Radiation intensity declines rapidly and continuously as η decreases. Locating the boundary of a rebuildable inner core is thus a matter of judgement. The

rebuildable inner core of this design spans the $|\eta|$ range of 2.0 to 3.0, which is 20% of the ECEM volume.

Replacing the scintillator in the inner core requires that each ECEM be removed from its endcap and laid down horizontally on its front plate in a suitable workspace. This ECEM removal and subsequent replacement requires a maintenance period long enough to roll both endcap calorimeters from the detector onto the hall operating floor for crane access. It is currently thought that SDC maintenance periods of several months duration will occur at one to two year intervals. After an ECEM has been removed from its endcap and positioned horizontally, rebuilding can begin.

For the materials used in the ECEM, induced radioactivity is not expected to be a problem[3-4]. A system of simple screw-fastened joints at the $|\eta| = 2.0$ boundary of the aluminum curtain (see Fig. 4-16) layers allows the inner core to be removed one layer at a time from the back side of the ECEM. With power screw-drivers and a vacuum lifting fixture, the disassembly can be done relatively quickly. A partially disassembled ECEM is shown in Fig. 4-17. The core volume is then rebuilt with new scintillator and fiber assemblies. The fiber bend radii at $\eta = 3.0$ are generously sized and the bend radius can be significantly reduced to avoid structures in the tracking volume.

In our baseline design the radial fiber routing system of the outer 80% volume of the ECEM is not disturbed during core rebuilding by virtue of the radially *inward* routing of the expendable inner core fibers. Inward routing is not necessary for the source tubes which share these fiber routing layers, since a simple "funnel socket" joint design will allow easy disconnection at the $|\eta|=2.0$ boundary.

The inward routing of fibers causes some complication for the fiber routing and we are actively pursuing low profile disconnects that would allow all the fibers to be routed inward. A sketch of a disconnect is shown in Fig. 4-18.

4.13. Options: The Case for Spokes

In the LBL Monolithic ECEM calorimeter design, minimization of "cracks" between scintillator tiles is a high priority. No structural bulkheads penetrate the tile layers, and "pizza pans" (see below for a definition) are not used because of their inherent inter-pan

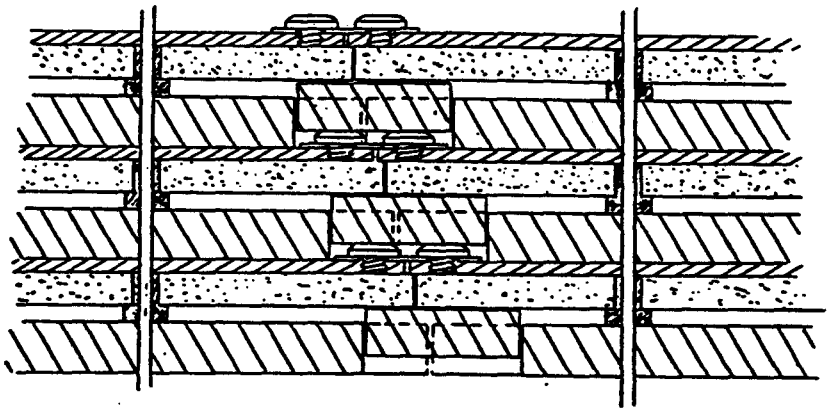

4-16a

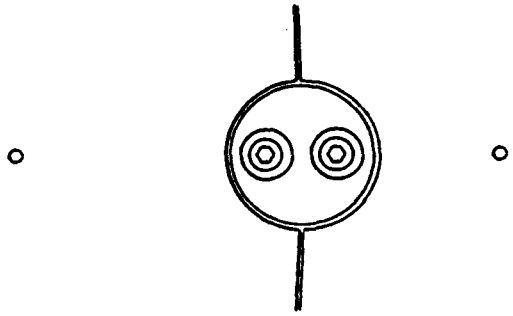

4-16b

Fig.4-16. Detailed view of the the joint at $|\eta| = 2$. showing the screw fasteners a) side view, b) top view.

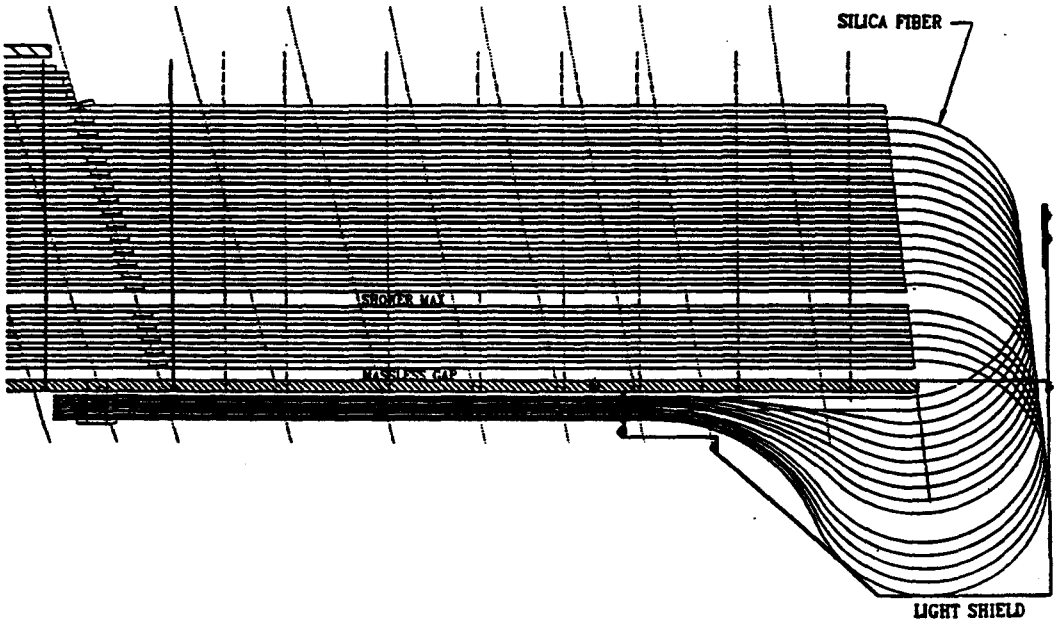

Fig.4-17. Expanded view of the ECEM between $2 < |\eta| < 3$ during disassembly for replacement of scintillator. Three absorber layers have been removed from the back of the calorimeter at this stage in the disassembly. The fiber bend radii at $\eta = 3.0$ are generously sized and the bend radius can be significantly reduced to avoid structures in the tracking volume.

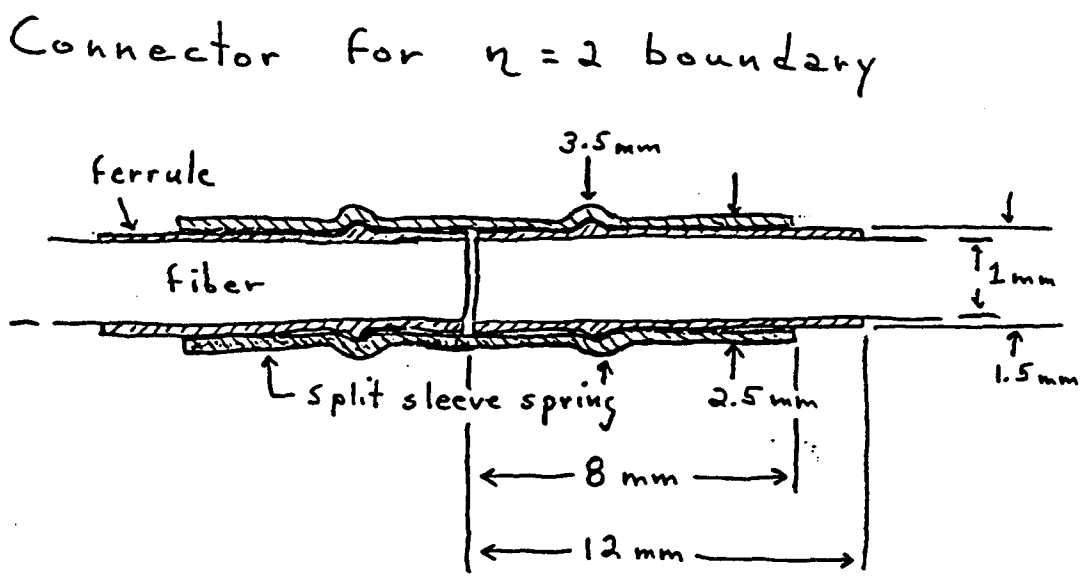

Fig.4-18. A sketch of a low profile disconnect that could be used at the $|\eta| = 2.0$ boundary so that all fibers routed radially outward. Each fiber is glued inside a ferrule, and the two ferrules are aligned by a split sleeve made from copper beryllium spring stock. Small projections on the ferrule and a detent in the split sleeve force the two fibers together axially.

edge gaps. The "curtain" structure which supports the lead and scintillator layers lies in its own planes between lead and scintillator layers. The only remaining structural link needed is a means to tie the lead and scintillator layers to their adjacent curtain layers in a simple, distributed, and unobtrusive manner. "Spokes" perform this function in the current design.

"Spoke" is our terminology for the axial 1.5 *mm* diameter titanium tie rods which penetrate all of the layers in the monolithic ECEM. Their functions are:

- Accurate location and support of the scintillator tiles (or "multi-tiles").
- Distributed support of the considerable weight of the lead absorber layers.
- Axial support of the layered structure when the entire ECEM is tipped at angles up to 28 degrees during fixed particle beam calibration.

The use of a large number of penetrating tie rods is unconventional in scintillating calorimeter design. Even though the volume of scintillator lost to the spoke/bushing penetration (0.12%) is far less than bulkhead structures, some people seem to harbor a basic dislike for this idea of stitching the calorimeter together with fine rods.

Another assertion is that there is an enormous number of these spokes to deal with (close to 3000 per endcap in the current design) during the assembly work. As each layer of the

ECEM is completed, all of these spokes will have to be manually advanced from below to engage the next layer. This is true, but it is a direct result of the inherent granularity of this calorimeter. There are 45,000 individual tiles to be accurately located and supported, and 375 square meters (28 tons) of lead to be located and supported. Doing all this with only 3000 spokes is actually quite an achievement! Conceptually, if one considers the support of a single tile and associated lead absorber by gluing, riveting, or by advancing a spoke, it becomes clearer that spokes represent a very simple, effective structural element.

Yet another concern is that slight tolerance deviations or fabrication errors will make it impossible to advance some of the spokes all the way through the 38 *cm* of stacked layers. In the assembly of our full depth, 4 tower x 4 tower calorimeter test station module, advancing of *one* spoke became difficult (but possible) toward the end of the stack-up. From this experience, we believe that a slight enlargement of the spoke holes in the lead layers (2.3 *mm* vs. 1.6 *mm*) will allow the spokes to "weave" very slightly between their close fits in the curtain layers. This should greatly reduce the frictional force on the spokes.

We now consider possible alternatives to spokes in a monolithic design:

- Glue. In principle it is possible to support the layers by gluing them together with radiation hard epoxy.

  Objections: As a general principle, good mechanical designs avoid the use of glue whenever possible. Glue is messy, time-consuming, and the results depend greatly on conscientious surface cleaning, mixing, de-gassing, control of application and cure conditions, etc.. When something goes wrong, it is usually not known until it is too late to salvage the assembly.

- Rivets. Flush rivets could be used to mechanically join lead and scintillator tiles to the supporting sheet metal curtains.

  Objections: The resulting riveted cell-layer assemblies would be very flimsy and difficult to handle.

- Pizza Pans. "Pizza pan" is the term given to describe the idea of mounting sets of end cap scintillating tiles on pie slice shaped sheet metal substrates. These assemblies are then inserted radially into slots in the absorber structure. The pizza pan assemblies

include radial fiber routing, and perhaps source tubes. We feel that pizza pans are a good idea for the hadronic endcap calorimeter, but not for the ECEM.

The advantages usually cited for pizza pans include:

1) Parallel Assembly. Several assembly stations can be put to work to assemble pizza pan units at the same time to reduce the duration of the overall assembly effort.

2) Dark Box Testing. Pizza pan units are of a size and weight that is amenable to dark box testing as a quality control step, and perhaps as a baseline calibration of tile response.

3) Easier Replacement of Radiation-Damaged Tiles. In the ECEM, it is expected that the inner (high η) tiles will become radiation damaged under high luminosity and that they may require replacement several times during the useful life of the detector. Relatively easy access to the inner tiles by radially removing the pizza pans from their slots is the biggest advantage claimed for the design.

In the ECEM, pizza pans also pose one overwhelming disadvantage: relatively wide edge cracks between pizza pans in a given layer of scintillating tiles. Edge cracks are a particular physics liability in the ECEM, and are the reason we have chosen a monolithic structure. The total edge crack would consist of a pair of edge tolerance zones on the adjoining pizza pans, and an intervening "bulkhead" member which itself would also have a locational tolerance. We would expect the net edge crack to be several millimeter, not much better than the TDR baseline.

We now examine the perceived advantages of the pizza pan concept relative to the LBL monolithic concept for the ECEM:

1) Parallel Assembly. It is true that the LBL monolithic design must be assembled one layer at a time, but azimuthally, there is plenty of room for multiple work stations. With suitable supports, up to eight assembly technicians could have simultaneous access to the layer under construction without getting in each other's way. Availability of qualified workers is likely to be a more limiting constraint than access to the work area.

2) Dark Box Testing. Experience shows (see Chapter 4) that tiles seldom fail to scin-

tillate properly. Problems are typically in the fiber connections and the fibers themselves. Off-line testing of spliced fiber assemblies, and subsequently, tile-fiber assemblies will eliminate deficient components before they are built into the monolithic ECEM. As a QC check, simple light transmission testing will be applied to each tile layer as it is completed. For both pizza pan and monolithic designs, any definitive *calibrations* will need to wait until the completed ECEM can be source tested without any further flexing of fibers or other disturbances.

3) Easier Replacement of Tiles. The monolithic ECEM does not offer random access to individual scintillator tiles once they have been "buried" in the assembly process. But, being buried, *they are also well protected.* Other than for eventual radiation damage, it is difficult to imagine any need to access tiles or fibers in the interior of the assembly. When radiation damaged tiles need to be replaced, the ECEM will need to be removed from the endcap for both the pizza pan and monolithic designs. Once the damaged module has been relocated to a suitable work area, the procedure for dismantling and rebuilding the inner core zone of the monolithic ECEM is comparable to reworking pizza pan assemblies. No significant radioactivation of the materials is expected, and multiple technicians can work on the inner core.

4.14. Responses to Criticisms

4.14.1. Spoke Holes in Scintillator Tiles

Piercing scintillator tiles for the sake of structure may seem repugnant at first glance. In reality, a 4.0 *mm* spoke bushing hole through a 10 *cm* x 10 *cm* tile removes only 0.12% of its volume. We believe that this will hardly be noticeable in Monte Carlo simulations of light ray trajectories inside the tile, and we have confirmed the spokes are invisible in our test beam results (see chapter 5). As removed material, it is negligible compared to previous designs with a fiber exit notch. For those who have visions of crazing around a drilled hole, note that the entire perimeter and about 40 *cm* of fiber groove are to be machined as well.

4.14.2. Spoke hole interference with fiber "sigma" patterns in the tiles

In some layers of a given tower, the axial support spokes will intersect a chosen sigma pattern groove for the wave shifting fiber embedded in the tile. We would therefore distort the sigma pattern very slightly in these tile varieties to avoid the spoke hole. We feel that small deviations from the ideal pattern will not significantly affect signal uniformity.

4.14.3. Mechanical stress on the scintillator tiles

In operation (and under radiation), a 10 *cm* x 10 *cm* tile supported in the vertical plane by a single 4.0 *mm* spoke bushing would see a concentrated bearing stress at the bushing of only about 34 kPa (5 psi). During assembly in the horizontal plane, the bushings protect the scintillator from the weight of the lead.

4.14.4. Rotation of the scintillator tiles on their bushings

The spoke pattern provides two spokes per tile at several intervals. With very small edge clearances between tiles, the periodic two-spoke stabilized tiles will lock the entire tile pattern into alignment.

4.14.5. Increased overall thickness of the EM calorimeter

This design eliminates cracks by routing fibers and source tubes between active layers. This may result in a somewhat increased overall thickness of the EM calorimeter. If the space between each of the 23 layers consists of 1.5 *mm* of aluminum (or 1 *mm* stainless steel) curtain plus a 2 *mm* fiber routing gap, the overall nominal thickness of the EM will be only 7.9 *cm* thicker than the total of the front and rear plates plus absorber and scintillator layers.

4.14.6. Structural mass at the perimeter of the endcap EM module

This design intentionally concentrates its mechanical structure at the perimeter of the module. This is acceptable because this perimeter radius is completely covered by the last barrel EM towers. Thus, its mass will not obstruct continuous EM coverage. Fortuitously, the volume taken from the endcap hadronic section for this structure does not badly compromise

the hadronic absorber depth at these angles; the rear outside corner of the hadronic endcap calorimeter already provides additional depth.

4.14.7. Radiation damage of fibers

This layered, monolithic design does not lend itself to axial routing of the fibers to the back of the EM module. Instead, radiation-hard silica fibers are used throughout the high radiation volumes. We assume that these silica fibers will be used throughout most of the ECEM, at a cost of $5.00 per meter.

4.15. Mechanical Structure Summary

In this section we have described a novel method for supporting the absorber and scintillators in the endcap electromagnetic region. The vertical orientation of the absorber plates allows the use of a system of slender penetrating bicycle spokes which provide a diffuse, local support for the absorber. The entire support system, including the bicycle spokes, is non-projective, and we show in Chapter 6 that the supports are invisible in 10 GeV/c electron showers. The mechanical system is relatively independent of the optical system and can accommodate a variety of different choices, from "multi-tiles" to different types for scintillators or fibers. To provide continuous EM coverage from the barrel to the endcap, the endcap is proposed to be a 32-sided figure with an approximately 2 *cm* overlap with the barrel EM calorimeter.

The design incorporates a complete source system, so that the effects of radiation damage and changes in the scintillation light due to magnetic fields can be directly measured for each tile. Access to the source tubes does not require any movement of the endcap, so the effects of the solenoid field can be measured *in situ*.

To allow for replacement of radiation damaged fibers and tiles at the inner diameter the design includes a rebuildable inner core. Our design shows fibers from this region exiting the calorimeter at the $|\eta| = 3.0$ boundary. We are actively pursuing low profile (< 3 *mm*) disconnects which would allow the fibers to be radially routed to the outer perimeter of the calorimeter.

4.16. Mechanical Structure References

[4-1] J. Mainusch, et,al."Influence of Magnetic Fields on the Response of a Uranium Scintillator Electromagnetic calorimeter",NIM A312 (1992)451.

[4-2] C. Hearty,"Recommended Isotopes for Calorimeter Source Calibration", SDC Note 92-387, (1992).

5. Optical System

The optical system of the endcap EM section is discussed in this chapter. The emphasis is on the system that was used in our calorimeter test station module. This calorimeter module was tested at BNL in the summer of 1992, and the results of these tests are described in Chapter 6. However, estimates of the light yield for the calorimeter module are reported in this chapter. This chapter ends with more general studies of radiation hardness and an outline of future R&D plans.

5.1. Description of the System Used in the Calorimeter Test Station Module

The calorimeter test station module is constructed from 352 tiles and readout fibers. Each of the fibers is identical, and is constructed from 40 *cm* of BCF-91A (polystyrene wavelength shifting fiber) spliced to 1 *m* of silica fiber (3M FT-1.0-UMT), then spliced to 1.3 *m* of BCF-98 (clear polystyrene fiber). All fibers are are 1 *mm* nominal diameter. The intent of using the silica instead of plastic as part of the light guide is to increase the overall radiation hardness in the region of the highest radiation dose. Radiation damage studies are underway to measure the radiation hardness of the optical system. BCF-98 is used outside of the high radiation area for its greater mechanical flexibility.

The plastic fibers were polished on a specially-modified fly-cutter at Fermilab. The silica fibers were polished, sixty at a time, by the LBL optics shop. One end of each WLS fiber was mirrored with sputtered aluminum at the LBL vacuum deposition shop. This was found to increase the light yield by 29% relative to having the end unpolished.

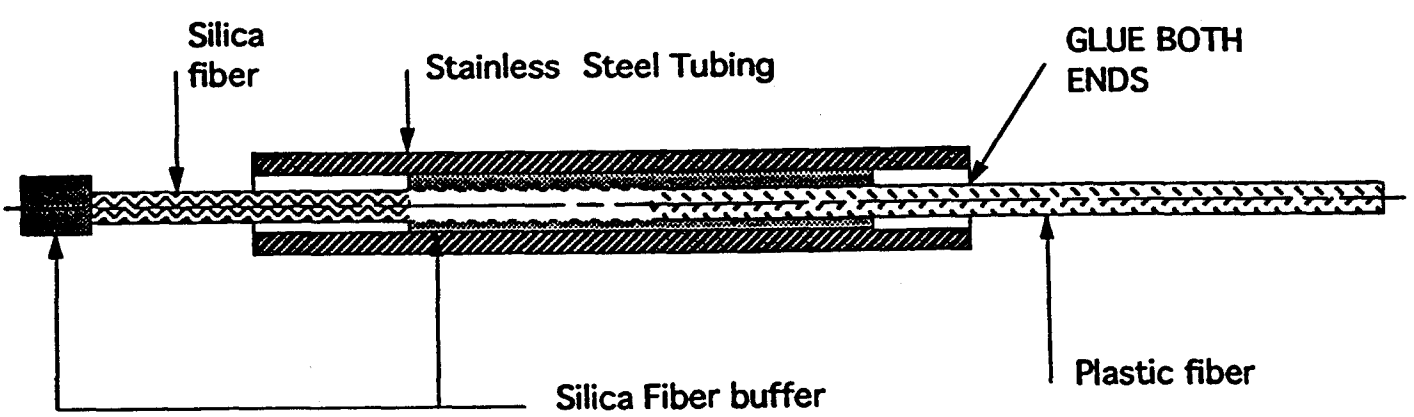

Fig.5-1. Splice joining the plastic WLS fiber to the clear silica fiber. The Tefzel buffer provides fiber alignment, while the stainless steel tube gives mechanical support.

The two splices (WLS/silica, silica/clear plastic) were made in the same way (Fig. 5-1). A Tefzel sleeve, which is a piece of buffer taken from the silica fiber, aligns the fiber ends, and a stainless steel tube (1.52 *mm*, 1.83 *mm* OD) encloses the fibers and is glued (with epoxy) to the fibers to provide mechanical support. There is a minimal air gap between fibers: it was believed that adding optical grease or epoxy to make an optical contact would complicate assembly and introduce problems of aging and nonuniformity with only a small increase in performance.

The tiles within a layer are identical; tiles differ between layers only in the location of the spoke hole. The tiles are 11 *cm* square, 4 *mm* thick Kuraray SCSN-81 scintillator. The edges were fly-cut, then painted with three layers of Bicron BC-620 optical white paint. The groove pattern is shown in Fig 5-2; the groove itself is a key-hole cross-section of 1.3 *mm* diameter. The groove pattern, with four rounded corners, was selected to improve uniformity near all four corners, although at the time of the beam test, a uniformity scan was not available to verity that this was the case. It was frequently difficult to insert the fiber past the final corner. As in our baseline design, the fiber exited the tile along an "s-groove", so that upon leaving the tile the fiber was adjacent to (and parallel with) the surface of the tile at the exit. The WLS/silica splice is located 7 *cm* after the fiber exits the tile. The tile was wrapped in aluminized mylar, 0.012 *mm* thick,to increase light yield; the mylar also served to isolate optically the WLS fiber from the scintillator outside of, and along the surface of the tile. Complete details of the tile construction are given in Ref. [5-1].

The fibers were glued into holes in a PVC cookie and held 1 *mm* away from a light mixer (a $25.4 \times 25.4 \times 76.2\ mm^3$ polished UVA lucite block). The light mixer was, in turn, glued to a Hamamatsu R580-17 green-extended PMT. Laboratory studies indicate that the light yield varies rapidly with the distance between the fiber end and the light mixer if the fiber end is even slightly recessed below the face of the cookie (Fig. 5-3). For this reason, the fiber ends were positioned 0.25 *mm* beyond the face of the cookie.

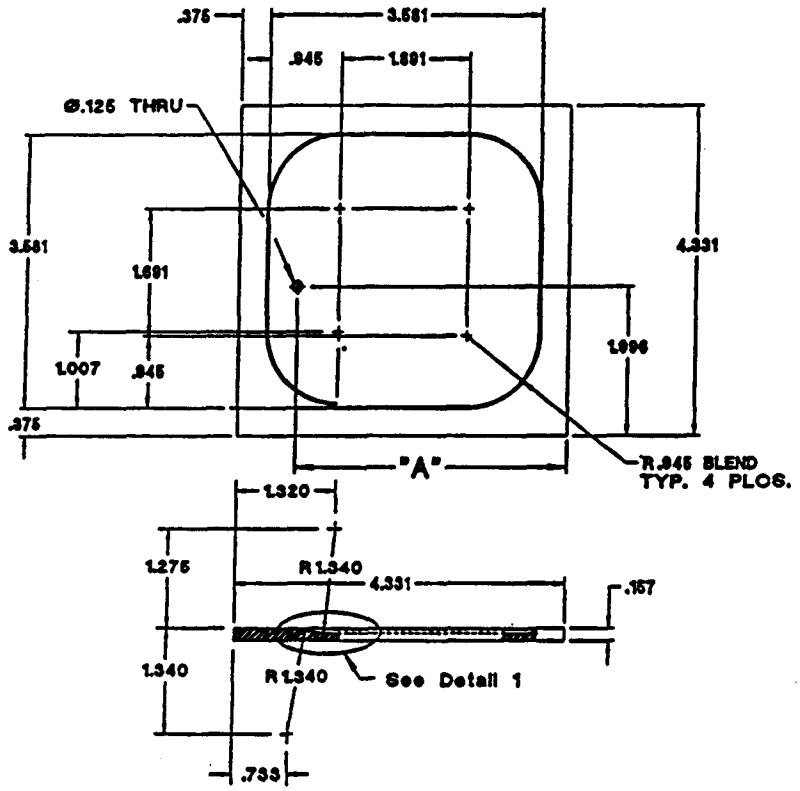

Fig5-2. Groove pattern used in the ECEM test module. The groove has a "keyhole" cross-section.

5.2. Performance

The performance of the optical system for the BNL test module is evaluated below in terms of light yield, uniformity and reproducibility. In this context, uniformity refers to the variation in response across a tile, while reproducibility refers to variations from tile to tile. The subsection on reproducibility also discusses the related issues of quality control and sorting.

5.2.1. Light Yield

The light yield is characterized in two different ways; by the number of photo-electrons per GeV of incident electron energy, and by the number of photoelectrons per minimum-ionizing particle per tile. The first quantity has been measured at the Brookhaven test beam, while the second has been measured both at BNL and in the laboratory.

The energy resolution for electrons at a particular energy can be divided into a component due to photostatistics (σ_p) and a component representing all other effects, such as shower fluctuations, beam momentum spread, and nonuniformities of light yield (σ_o). We define σ_p

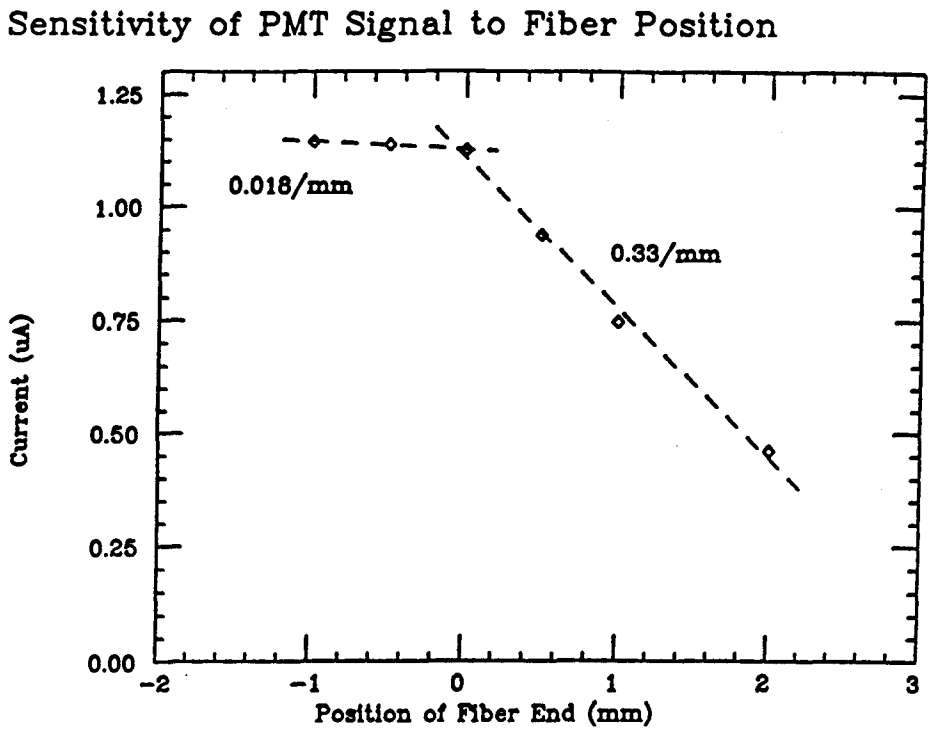

Fig.5-3. Current from the PMT as a function of the distance between the fiber-end and the light mixer face. The cookie is held fixed relative to the mixer. The break in slope occurs when the fiber end is flush with the cookie face.

at the the Poisson fluctuation about the mean value of photoelectrons, N_{pe}. Thus,

$$\sigma_E/E = \sigma_o \oplus \sigma_p = \sigma_o \oplus 1/\sqrt{N_{pe}}$$

The resolution for 10 GeV/c electrons in a single tower was measured twice; with and without a neutral density filter (NDF) having a light transmission coefficient of 0.484 between the optical fibers and the PMT. We obtain $\sigma_E/E = 0.0730 \pm 0.0009$ in the former case, 0.0621 ± 0.0011 in the latter (Fig. 5-4).

The remaining fluctuations, σ_o, are unchanged by the NDF, so the observed increase in σ_E/E is due to a reduction in the mean number of photoelectrons:

$$(\sigma_E/E)_1^2 - (\sigma_E/E)_2^2 = 1/N_1 - 1/N_2$$

Without the NDF, we obtain $N_{pe} = 724 \pm 93$ for 10 GeV/c electrons in a single tower. The test beam data indicate that 93% of the energy is contained within a single tower, so

$$\text{light yield} = 78 \pm 10 \text{ p.e./GeV}.$$

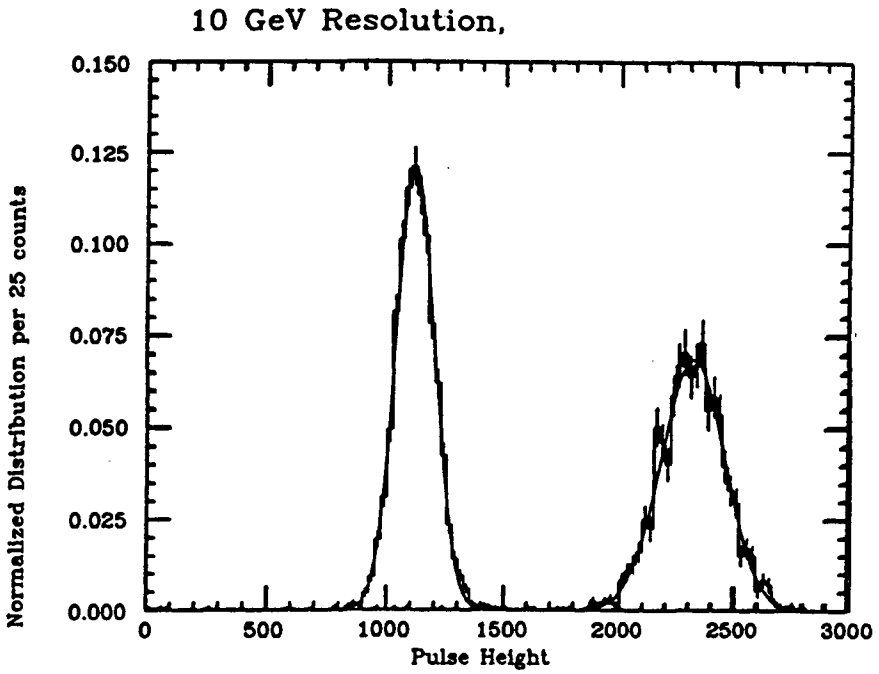

Fig.5-4. Single-tower resolution for 10 GeV/c electrons, with full light and with a 50% neutral density filter between the fibers and the PMT.

The 10 GeV/c electron peak in the tower used to make this measurement is at 2309 ADC counts above pedestal, corresponding to 0.314 ± 0.040 photoelectrons per ADC count. The peak signal for 10 GeV/c muons are at 27.2 counts and 61.3 counts in EM1 (7 layers) and EM2 (15 layers), respectively. Taking these values to represent seven and fifteen times the mip signal gives 1.2 ± 0.2 pe/mip/tile (EM1) and 1.3 ± 0.2 pe/mip/tile (EM2). Overall, the testbeam measurement of the tile response is

$$\text{light yield} = 1.26 \pm 0.16 \text{ p.e./tile/mip.}$$

The number of photoelectrons per tile has also been measured in the laboratory using Ru^{106} and Sr^{90} sources. The experimental setup is shown schematically in Fig. 5-5. The signals from the PMT were digitized in a Lecroy 2249a ADC, with a 200 ns gate provided by a coincidence from the two trigger counters. The HV for the trigger counters was plateaued using the trigger rate; the calculated light yield was sensitive to this HV setting if the HV was too low.

Two different phototubes were used. The R580-17, which has a green extended photocathode and was used in the BNL test module, and an Burle 8875 ("Quantacon"). The

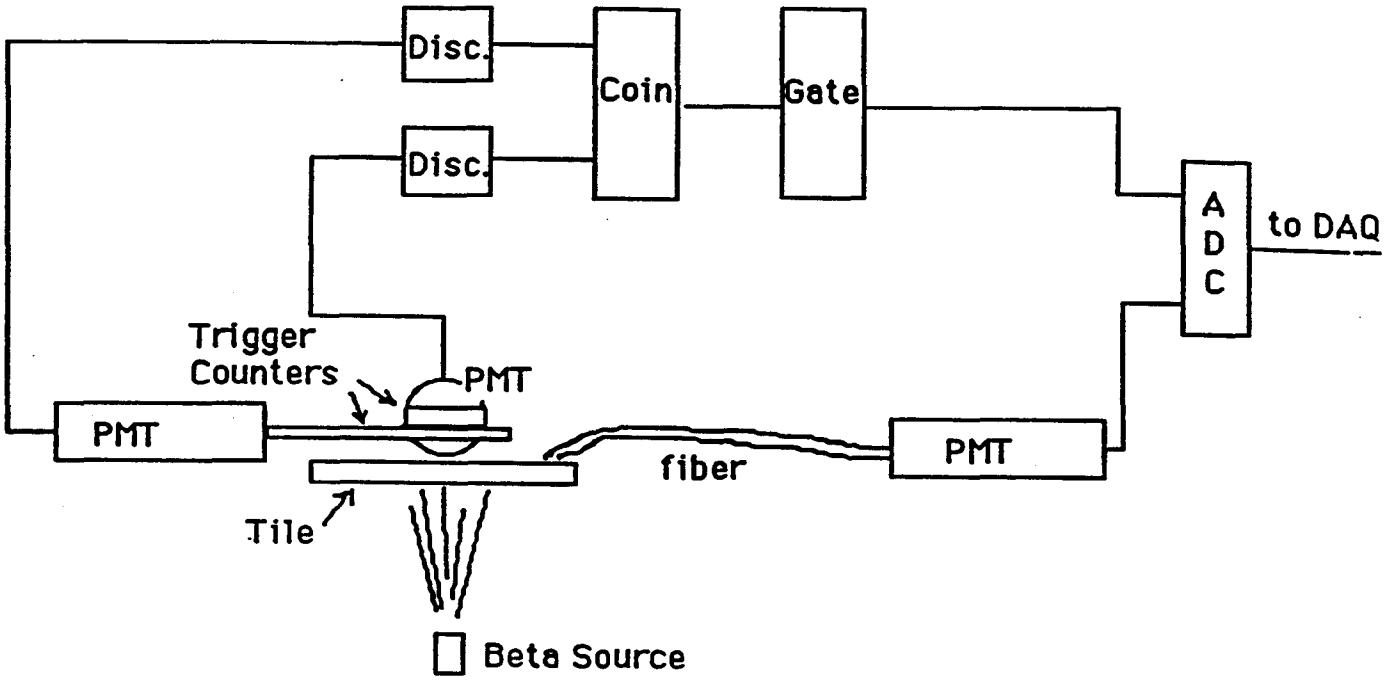

Fig.5-5. Apparatus to measure photoelectrons per tile per mip in the laboratory.

Quantacon has lower quantum efficiency (13%) than the R580-17 (17%) but has higher gain and better single-photoelectron resolution. Although the R580-17 was operated at 1550V, a LeCroy Model 133B 10× linear amplifier was needed to boost the signal into the dynamic range of the ADC. The amplifier was not used with the Quantacon. The pulse height spectra observed in the two cases are shown in Fig. 5-6.

The mean number of photoelectrons is extracted from these spectra in two ways. The first is from the number of entries with zero photo-electrons, while the second uses the ratio of the average response to location of the single photoelectron peak. The results are summarized in Table 5-1. The errors are due to the ambiguity in deciding which events are in the zero peak and the difficulty in locating the single-pe peak. The four source measurements with the R580-17 are reasonably consistent and agree with the value measured in the test beam. The light yield with the Quantacon is only 0.56 ± 0.03 times that with the R580-17, indicating that the actual Quantacon quantum efficiency is lower than the manufacturer's specification (or the R580 is higher, or both).

The light yield depends on a large number of factors. Our laboratory measurements have so far concentrated on the fiber. Based on measurements taken during the assembly of 10

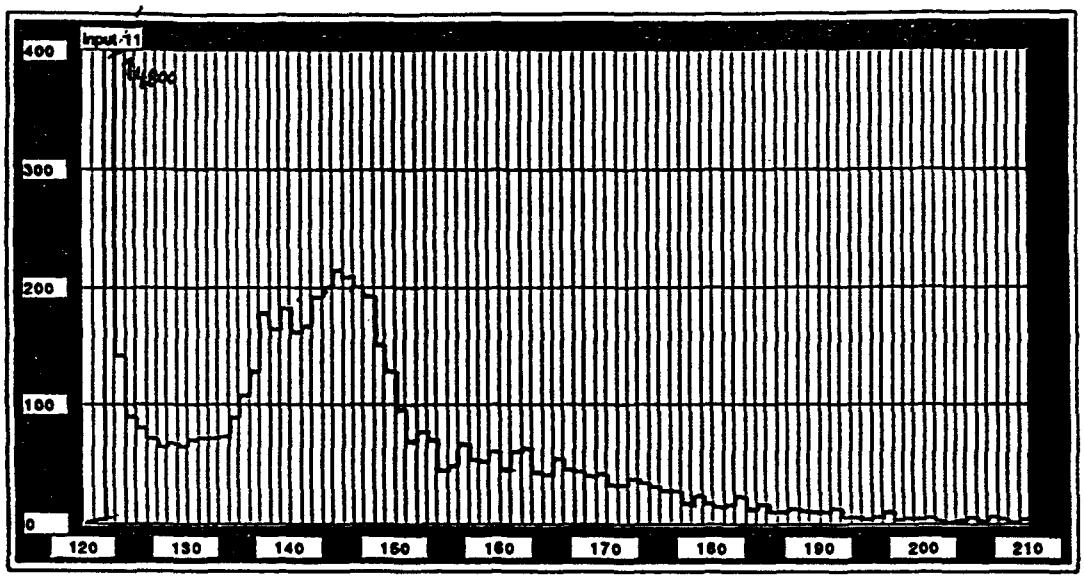

(a)

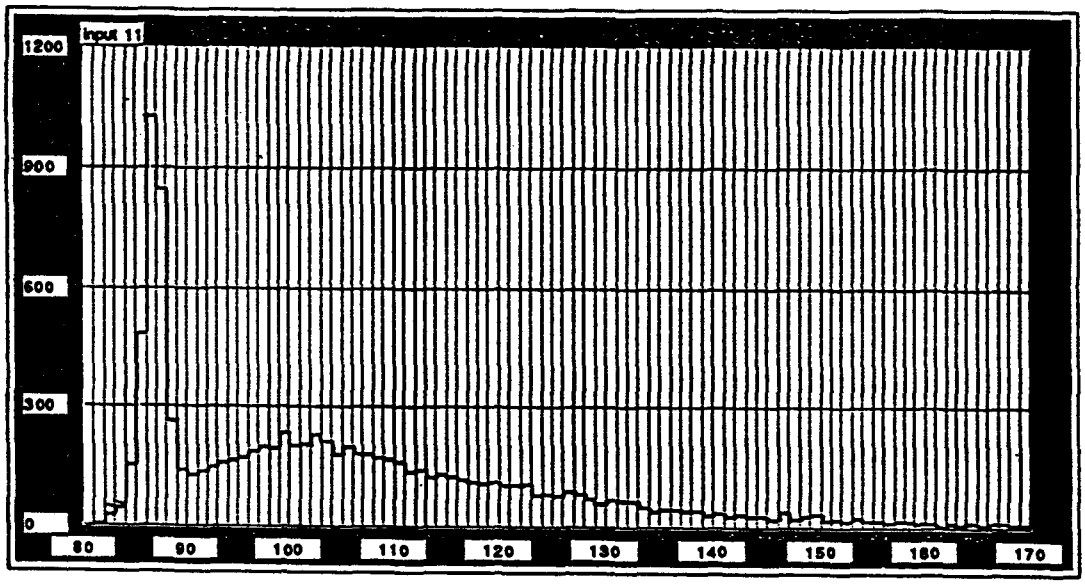

(b)

Fig.5-6. Minimum ionizing pulse height spectra of a tile/fiber used in the ECEM test module, measured with a Ru-106 source and a (a) Quantacon PMT, or a (b) R580-17 PMT. The single pe peak is much clearer with the Quantacon, but the light yield is greater with the R580-17.

Table 5-1. Light yield measurements (photo-electrons per tile per minimum ionizing particle) in the laboratory and in the BNL testbeam. Optical system in all cases is 11 *cm* square, 4 *mm* thick SCSN-81 tile with painted edges, wrapped in aluminized mylar, with a 1 *mm* diameter fiber consisting of 40 *cm* BCF-91a spliced to 1 m of silica, which in turn is spliced to 1.3 m of BCF-98.

Source	Phototube	Light yield from zeros	Light yield from peak
Ru-106	Quantacon	0.68 ± 0.03	0.61 ± 0.07
Ru-106	R580-17	1.21 ± 0.04	1.34 ± 0.08
Sr-90	R580-17	1.33 ± 0.04	1.31 ± 0.08
10 GeV/c μ	R580-17	–	1.26 ± 0.16

fibers, the light output at the end of the silica fiber is 58% of that at the end of the BCF-91a, and the output at the end of the complete fiber is 32%. The major contributions to the losses include two splice transmissions, attenuation in the silica, attenuation in the BCF-98, and numerical aperture mismatch between the silica and the BCF-91a. Using the measured attenuation lengths of 29 m for silica and 7 m for BCF-98, we estimate the transmissions to be 0.97 for 1 m silica, and 0.83 for 1.3 m BCF-98.

The fraction of light captured in going from a larger numerical aperture (NA_1) to a smaller (NA_2) is $(NA_2/NA_1)^2$ [5-2]. The NA of the BCF-98 is 0.584, but the silica NA is uncertain: the manufacturer's specification is $NA = 0.37 \pm 0.02$, but this is inconsistent with the indices of refraction of the core (1.456) and the cladding (1.368), which would imply $NA = 0.50$. Using $NA = 0.50$, the fraction of light captured is 0.73; for the lower, advertized silica NA, the fraction is 0.40.

We do not have a direct measurement of the splice transmission. However, the product of the splice, the BCF-98 attenuation, and any NA loss in going from silica to BCF-98 is 0.55.

5.2.2. Reproducibility/Quality Control

The BNL test module required 352 tile/fiber combinations for which a total of 359 were produced. The light yield of all 359 were measured by exposing each tile/fiber assembly to a source and measuring the current induced in a standard PMT. The gain of the PMT was monitored with a standard tile and fiber. There were three goals for these measurement: quality control (to reject combinations out of tolerance); to quantify and understand sources of variations; and to sort tiles to minimize the impact of variations.

Quality Control

The response of the 359 combinations is shown in Fig. 5-7. Seven tile/fiber combinations were rejected during the measurements of the 359, and several more would have been rejected had additional spares been available. In all cases, the fiber was faulty. An additional three fibers were rejected before they were placed in tiles. This failure rate of 3% is acceptable, but could have been reduced with better quality control on the components—particularly the BCF-98 fibers—before the complete fiber was assembled. No tiles were rejected by optical measurements.

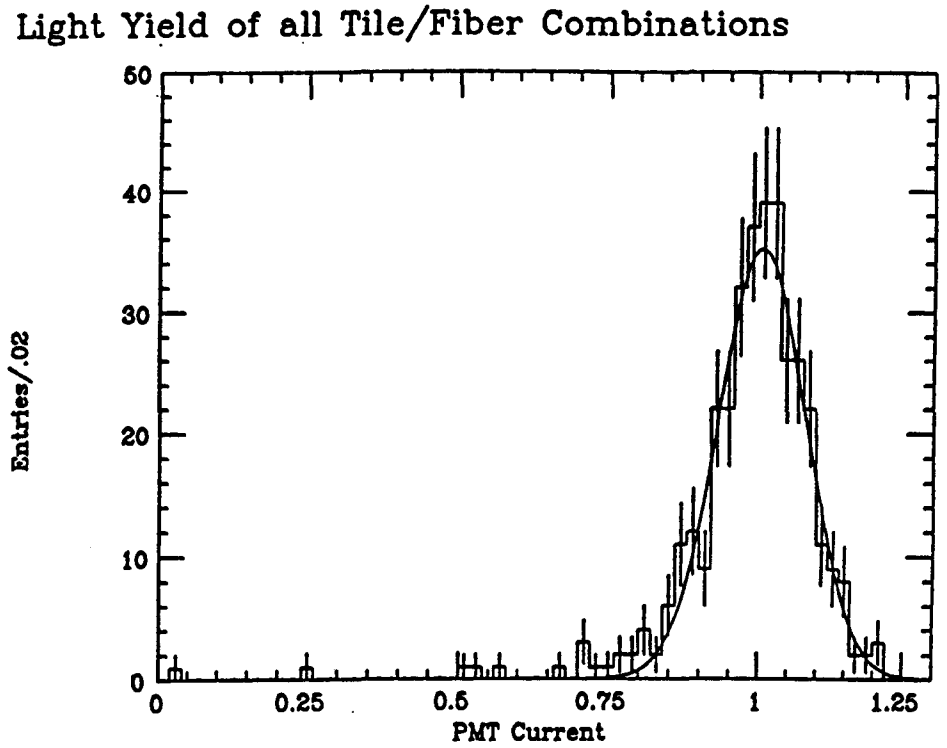

Fig.5-7. Light output of the 359 tile/fiber combinations produced for the ECEM test module. The current induced in an R580-17 PMT was measured while the full face of the tile was exposed to a Ru-106 source.

Reproducibility

A gaussian fit to the response of the tile/fiber assemblies actually used gives an *rms* of 7.4% (Fig. 5-7). Without longitudinal masking, this result satisfies the SDC requirement that tile-to-tile variations be less than 8% in order that the induced constant term be less than 0.5%. To extract the different contributions to this variation, sixteen tiles were weighed, then measured with the same fiber, and 38 fibers were measured using the same tile. The *rms* of the response of the sixteen tiles is $2.1 \pm 0.4\%$. The weight variation is 1.4% with a 44% correlation with the light yield. Other effects—edge painting and wrapping, for example—account for the remainder. The *rms* of the tile area is 0.06%, indicating that the weight variation is due to thickness variations not machining tolerances. The 38 fibers showed a much larger variation (Fig. 5-8).

The distribution is non-gaussian; the *rms* is 5.1%–8.1%, depending on which fibers are included. Various fiber subassemblies, including mirrored BCF-91A, BCF-91A plus silica, silica only and BCF-98 only, were tested in order to determine the sources of this variation. The testing consisted of illuminating one end of the fiber with light from BCF-91A (or directly

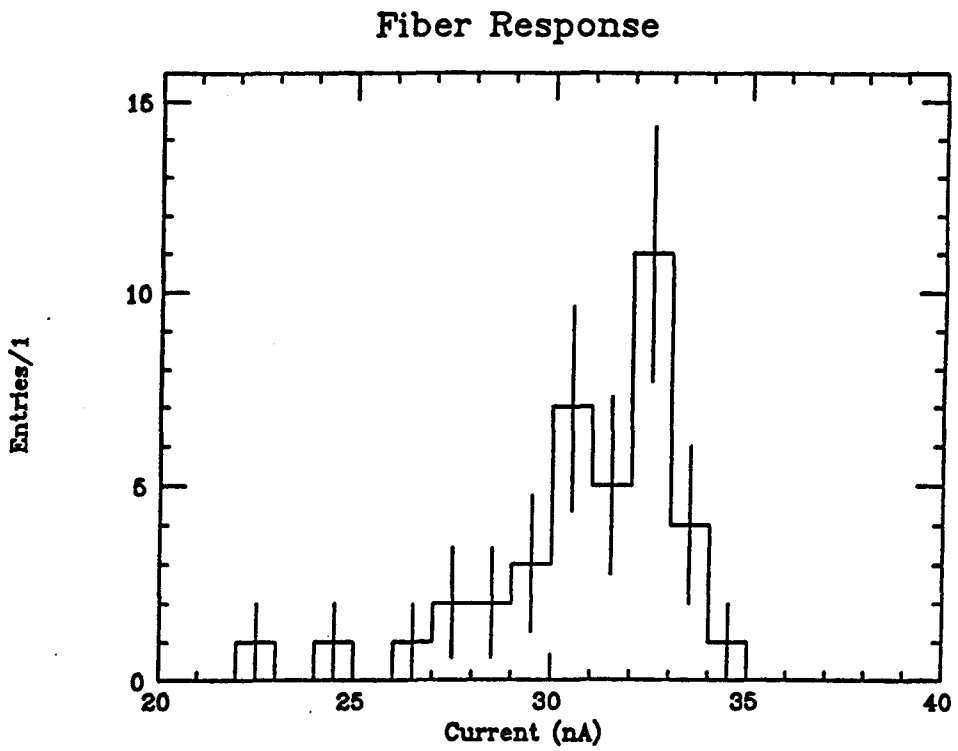

Fig.5-8. Current measured from an R580-17 PMT for each of 38 fibers inserted in the same tile and exposed to an Ru-106 source.

with a blue LED) and measuring the light output from the other end with a photodiode or PMT (Fig. 5-9). (To test mirrored BCF91-A, we used a blue LED to excite WLS. Transmission tests are not possible in this case.) The variability observed in each component of the complete fiber is summarized in Table 5-2.

Table 5-2. Variability of subcomponents of the complete fiber used in the ECEM test module.

Item	Number Tested	*rms* (%)
Mirrored BCF-91a	10	3.1 ± 0.7
Silica	20	1.0 ± 0.2
BCF-98	20	2.5 ± 0.4
Mirrored BCF-91a + Silica	10	3.8 ± 0.8
Silica + BCF-98	10	2.9 ± 0.6

From the last two entries in this table, the predicted overall *rms* would be $4.8 \pm 0.7\%$, which is reasonably consistent with the measurement of the 38 complete fibers. By comparing the spliced and individual fibers, and the mirrored vs unmirrored plastic cases, we can deduce that each splice contributes approximately 2% to the *rms*, and that the mirroring

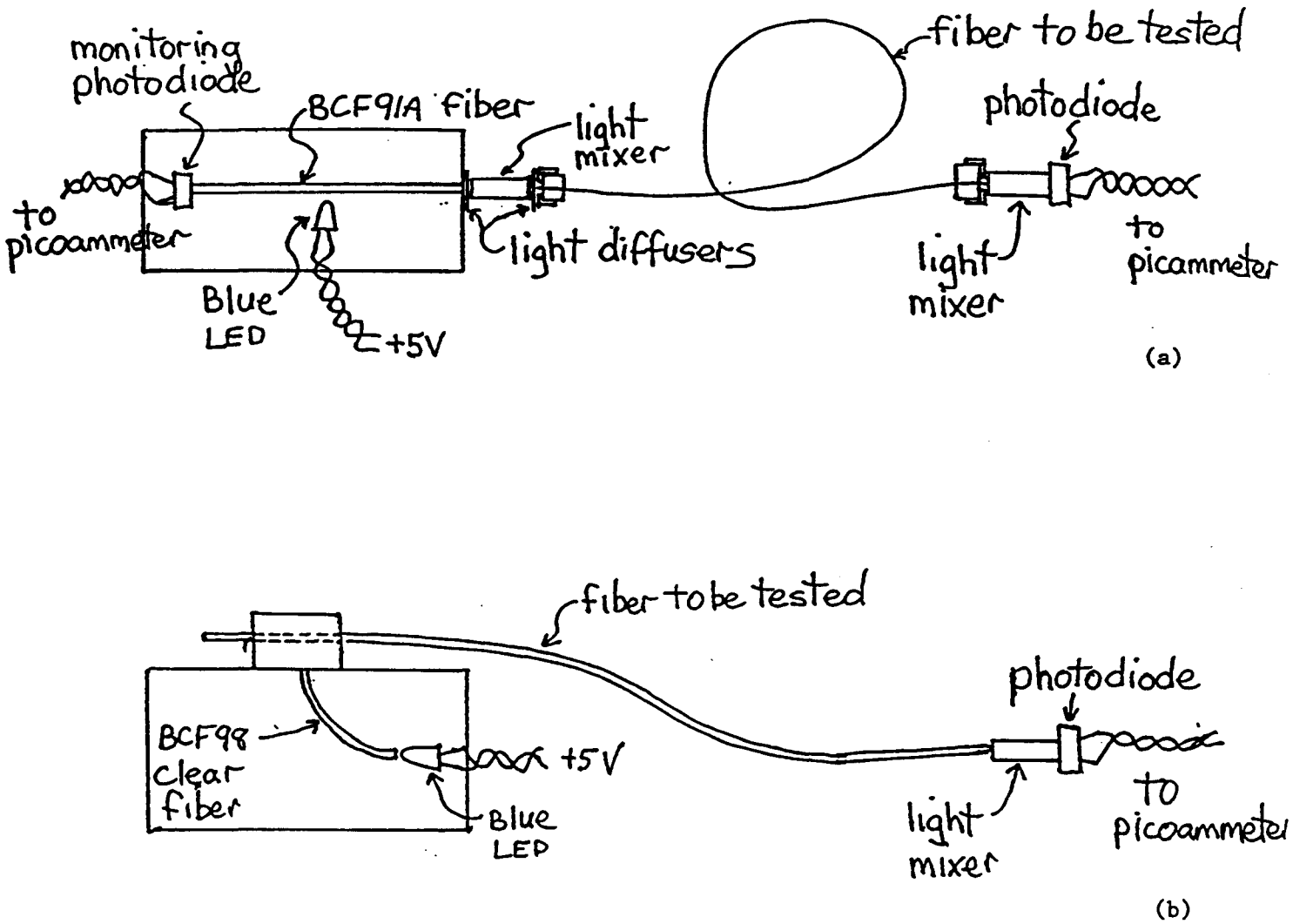

Fig.5-9. (a) Apparatus to test fiber transmission. A blue LED excites a BCF-91a wavelength shifting fiber. The light from this fiber passes through two diffusers and a light-mixer and enters the fiber being tested. A photodiode monitors the light output of the other end of the excited BCF-91a fiber. The test fiber is held at both ends by a precision brass fixture, with the fiber end extending approximately 0.5 *mm* beyond the fixture. The light exiting the test fiber is measured either with a photodiode or with an R580-17 PMT. (b) The WLS in fibers can be excited directly with blue light from the LED.

also contributes approximately 2%. Therefore, the fiber variability is due to five nearly equal contributions: the two plastic fibers (BCF-91a and BCF-98), the two splices, and the mirroring.

The low end tail observed in the 38 fibers has not been studied in detail, but in cases where failures were studied, the cause was almost always a chip on the end of the BCF-98. There are other effects that contribute to the overall variability. The test did not illuminate the entire WLS fiber, so variations in the surface quality of the BCF-91A are not reflected

in Table 5-2. Also, three different batches of BCF-91A and two batches of BCF-98 were used. Differences in light yield as large as 8% were observed between different batches of BCF-91A. We did not, however, monitor differences in light yield within a batch. The small samples used in Table 5-2 would not reflect these differences.

Tile Sorting

Sixteen of the measured fibers were inserted into the sixteen measured tiles. The response of the combination was very well correlated with the response predicted by the separate measurements of the tiles and fibers: the correlation was 0.98 (Fig. 5-10).

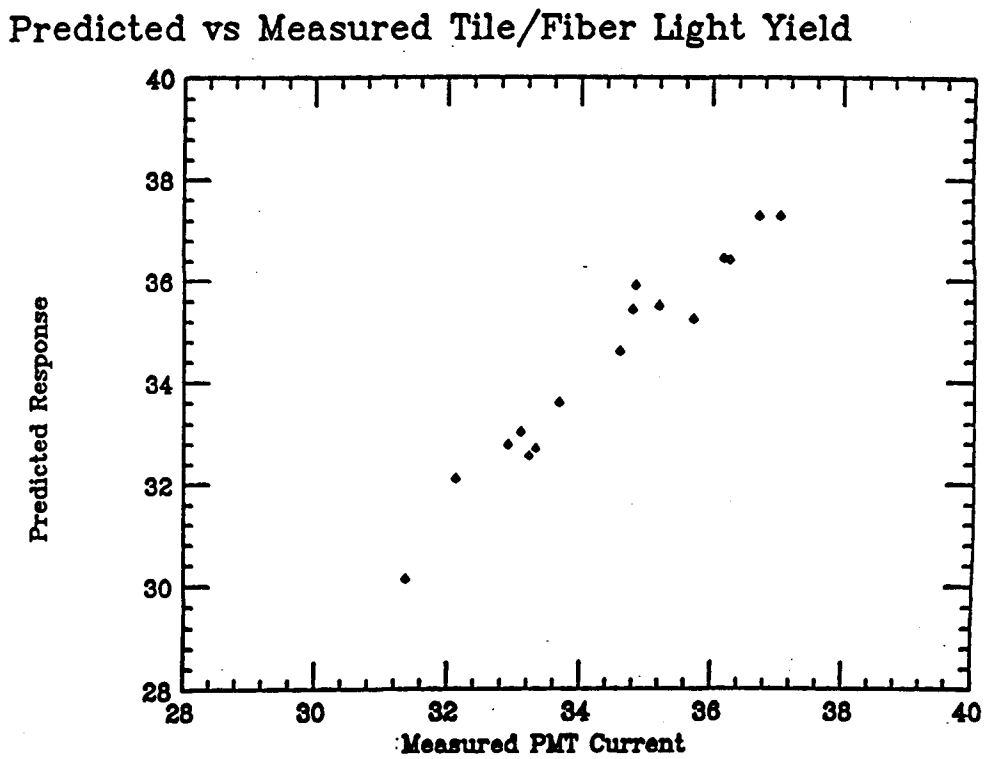

Fig.5-10. Correlation between light yield measured for tile/fiber combinations and the value predicted from separate measurements of the tile and fiber.

The implication is that measurements of the fibers alone could be used to do sorting in the future, since they are responsible for essentially all of the variation

For the BNL device, the sixteen tile/fibers in a layer were ordered by brightness then assigned to towers by this rank. The brightest tile was placed in tower 16, the dimmest in tower 1, and the tile/fiber assemblies closest to the average were placed in towers 6, 7, 10 and 11—the central four towers. This sorting increases the differences between towers and

decreases the differences within towers. The effective tile-to-tile *rms* for the central four towers was decreased from 7.4% to 4.1%; for the full sixteen towers, it was reduced to 5.0%.

5.2.3. Uniformity

The uniformity of a single tile-fiber combination was measured in the laboratory using a Sr^90 source collimated by a 3 *mm* hole in a 15 *mm* thick lucite plate. The tile was manually located to within 0.5 *mm* on the apparatus. A one-dimensional cross-section of the beam at the tile, determined by the response near the tile edge, is shown in Fig. 5-11. 98% of the energy is deposited within ±3.5 *mm*. Figure 5-12 is the tile response, as determined by the current from an R580–17 PMT at 1250 V, in a 5 *mm* square grid on the face of the tile. Figure 5-13 is a scan across the center of the tile. Qualitatively, the uniformity is good within the fiber loop, but shows a 6–9% higher response at the fiber and outside the loop. The response in the corners is low by 6–9%. Locating the fiber groove closer to the tile edge is expected to improve the uniformity.

The uniformity of the calorimeter was evaluated in the test beam by a number of position scans with 10 GeV/c electrons. Figure 5-14 shows the average energy measured as a function of position for a vertical scan through two adjacent towers. The overall structure is very similar to that seen in the laboratory scan. (Note that the bin size reduces the impact of the crack between the towers). Data was not taken at all locations in a tower to measure the overall uniformity.

5.3. Radiation Damage Studies/Silica Fiber Selection

Radiation damage studies have so far concentrated on silica fibers, which have been measured using the apparatus shown in Fig. 5-9a. Six different 1 *mm* diameter silica fibers have been tested, one from 3M and five from Ensign-Bickford. The fibers were coiled into a seven-inch diameter circle and irradiated in a Co-60 source at a rate of 0.61 Mrad/day. and compared to a set of four standard fibers (all 3M). The measurements were generally performed 4–24 hours after irradiation. The fibers showed no significant annealing in four months.

The transmission as a function of dose is shown in Fig. 5-15 and summarized in Table 5-3. Most of the damage occurs in the first two Mrad, and the two fibers being

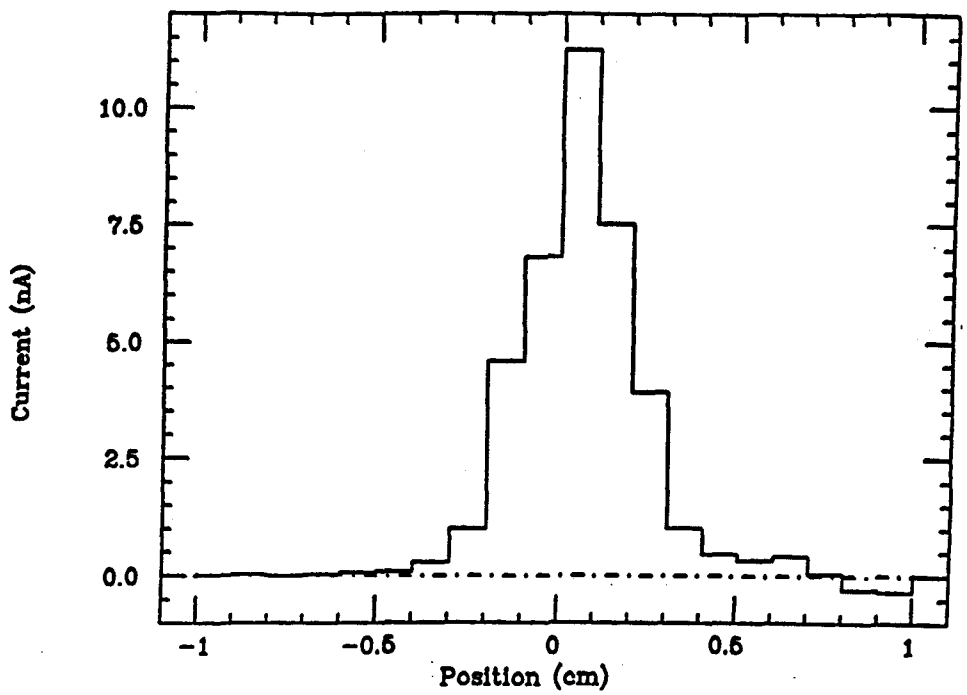

Fig.5-11. One-dimensional cross section of the collimated Sr-90 beam used to measure tile uniformity. Plot was derived from a scan over the edge of the tile.

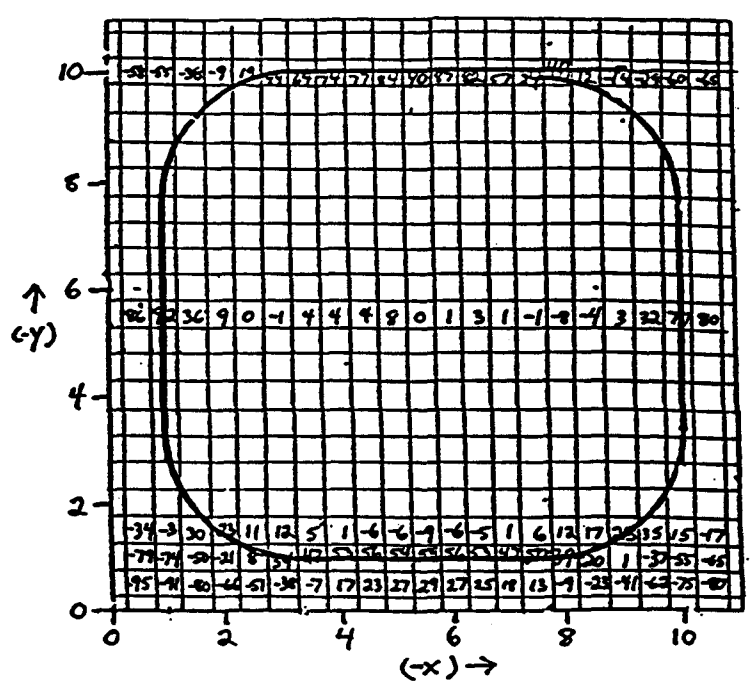

Fig.5-12. Deviation of the light yield of an ECEM test module tile/fiber from the value at tile center, in parts per thousand. Each bin is 5 *mm* by 5 *mm*. Measurement was made with a collimated Sr-90 source.

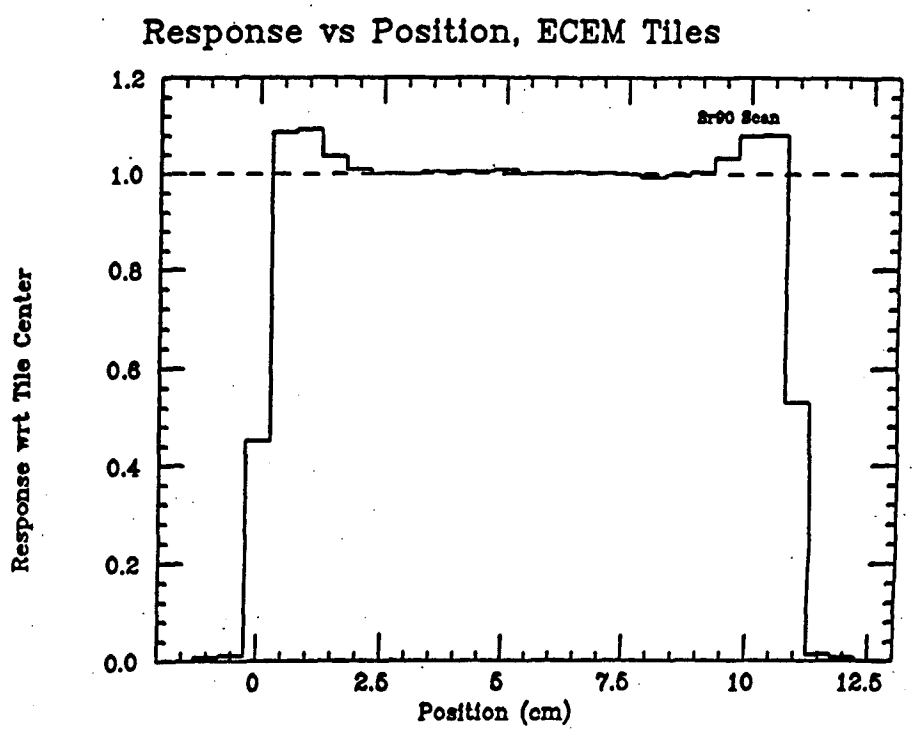

Fig.5-13. Light response as a function of position in the tile. Scan is parallel to the tile edge, through tile center.

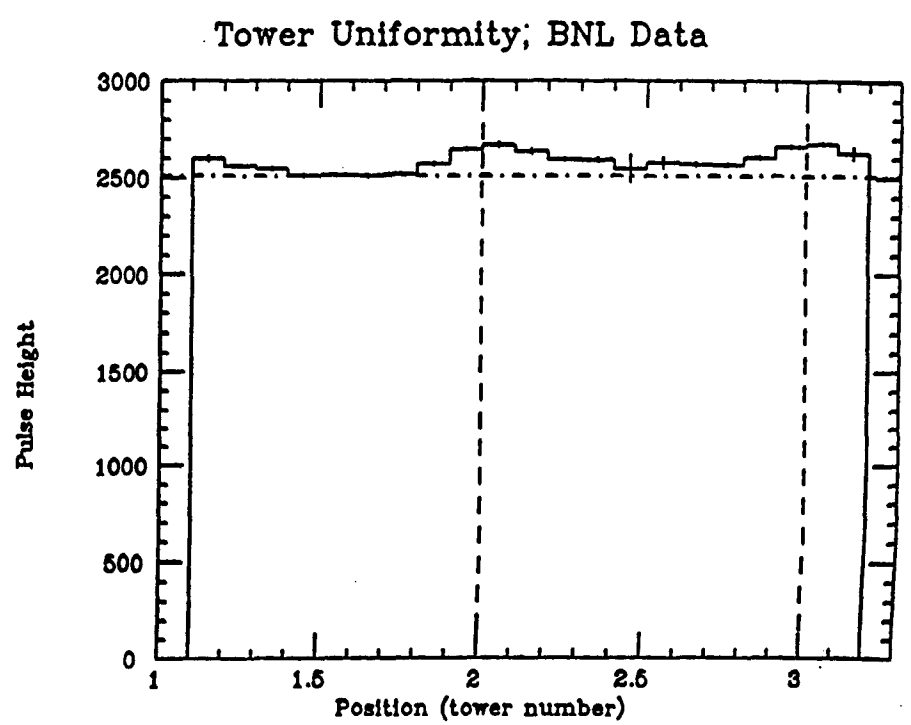

Fig.5-14. Uniformity of the ECEM test module response to 10 GeV/c electrons. The scan is through the centers of two of the four central towers. The dashed lines indicate tower boundaries; the dotdash line is the nominal value at tower center. Quantity plotted is pedestal-subtracted ADC counts, summing the nine towers closest to the shower.

considered for further use — 3M FT–1.0–UMT and EB HCR–H1000 — appear nearly stable after 4 Mrad.

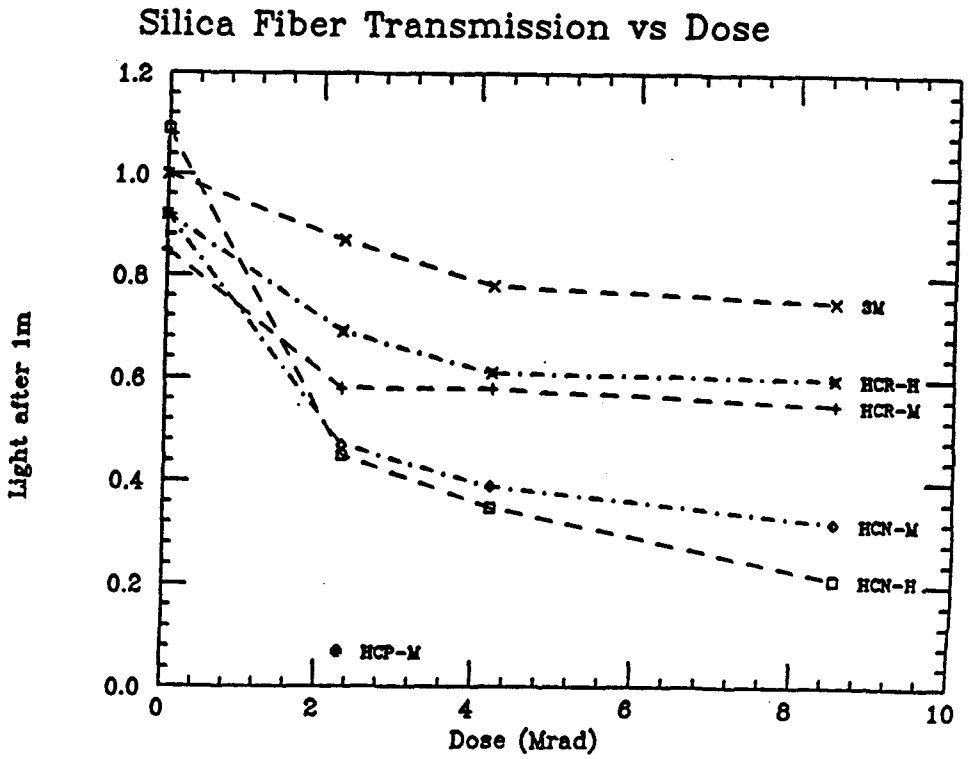

Fig.5-15. Light transmission through 1 m long samples of several types of silica fiber as a function of Co-60 radiation dose (1.5 m sample for HCR-M). The light is from BCF-91a emission, which is peaked at 500 nm.

Table 5-3. Summary of radiation hardness studies of silica fiber. Entry in table is the light measured at the end of a 1 m long, 1 *mm* core diameter, fiber exposed to a standard light source. For HCR–H1000, values are interpolated from light yield for longer and shorter samples. The sample length for HCR–M1000 is 1.5 m. D is the radiation dose in Mrad from ^{60}Co exposure.

		Relative light after Dose D			
Manufacturer	Fiber Type	$D = 0$	$D = 2$	$D = 4$	$D = 8$
3M	FT–1.0–UMT	1.00	0.87	0.78	0.75
Ensign-Bickford	HCN–M1000	0.92	0.47	0.39	0.32
	HCN–H1000	1.09	0.45	0.35	0.21
	HCR–M1000	> 0.85	> 0.58	> 0.58	> 0.55
	HCR–H1000	0.92	0.69	0.61	0.60
	HCP–M1000	–	< 0.07	–	–

5.4. Future Plans

R&D is continuing with the goals of increasing light yield, improving uniformity and ease of use, and decreasing the cost of the system. This work is outlined below.

5.4.1. Fiber Connectors

To simplify the assembly and transportation of the ECEM, we plan to have a connector instead of a splice between the silica and the clear plastic. The eight-fiber connector shown in Fig. 5-16 has been built and tested in the laboratory.

The fiber is glued into a ferrule then polished flat with the ferrule surface. The ferrules are aligned with a beryllium-copper split spring and pushed together by the spring on one side. A total of twelve 1 m long 3M silica fibers were polished with ferrules. The light transmission through 30 combinations of two fibers was measured using the apparatus shown in Fig. 5-9a and compared to a 2 m fiber. The same eight-fiber connector was used for all measurements. The average transmission is 84%, and the *rms* is 3.5% (Fig. 5-17).

The transmission may be improved by polishing one end to a physical-contact (PC) finish. With a PC finish, the fiber end is not square but is domed in the center. The spring forces the fibers together to exclude the air, eliminating the light loss due to the air gap. Tests of the silica/BCF-98 transmission are underway.

A commercial connector produced by the Ensign-Bickford company—the "Versalink"—is also being evaluated. This is a relatively cheap injection molded connector that could potentially be supplied with the fibers.

The splice between the WLS and the silica could be improved by combining the functions of alignment and mechanical support. Custom produced PEEK tubing is a possibility that is being investigated.

5.4.2. Radiation Damage

The full optical system—tiles, tile wrap, fibers, and splices—must be evaluated for radiation hardness. The results of these tests may indicate directions for more work.

The WLS fiber, BCF-91A, is known to not be rad-hard to the levels that will eventually be reached in the ECEM. We are studying replacing the BCF-91A with WLS-coated silica

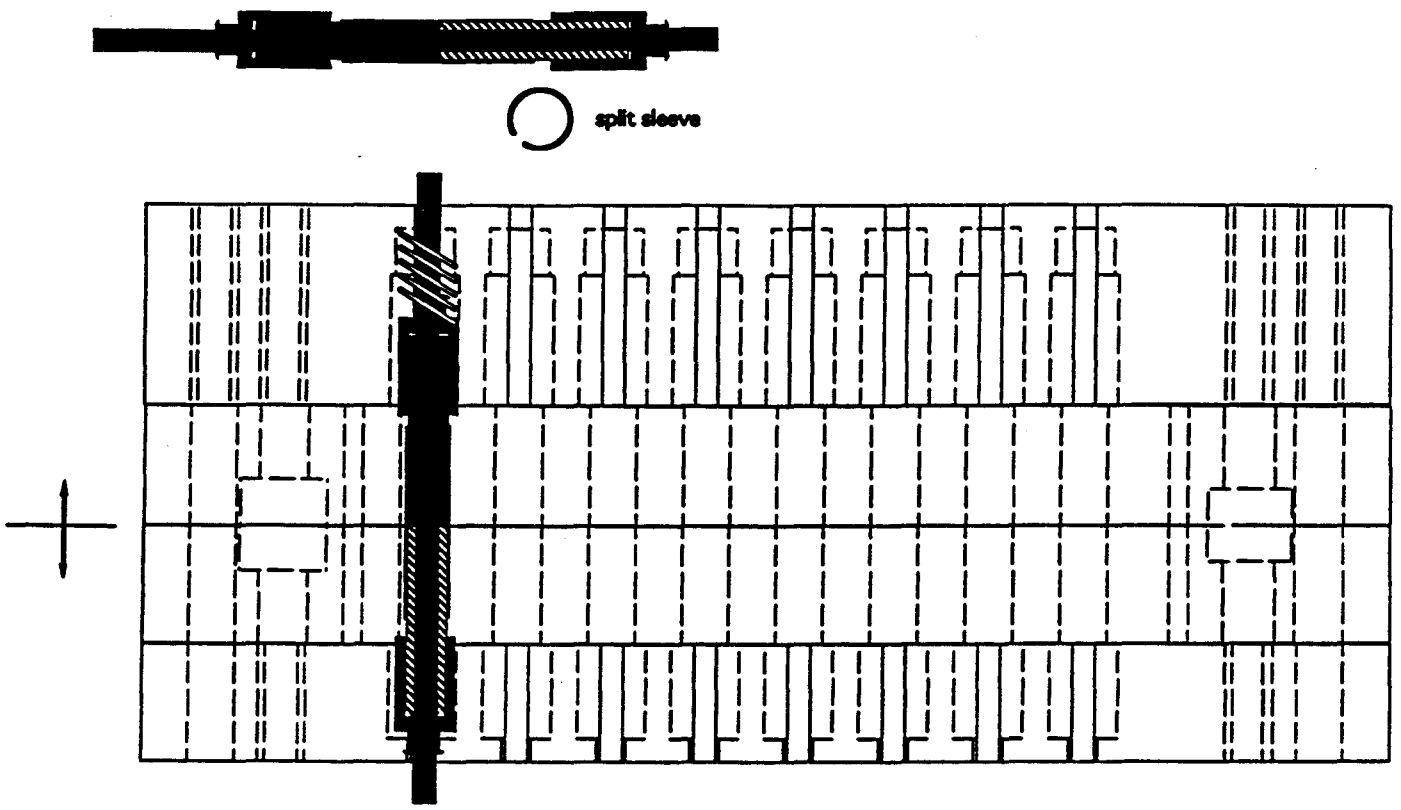

Fig.5-16. Multifiber connector prototype. Each fiber is glued into a stainless steel ferrule. The outer diameters of the ferrules are aligned by the copper-beryllium spring.

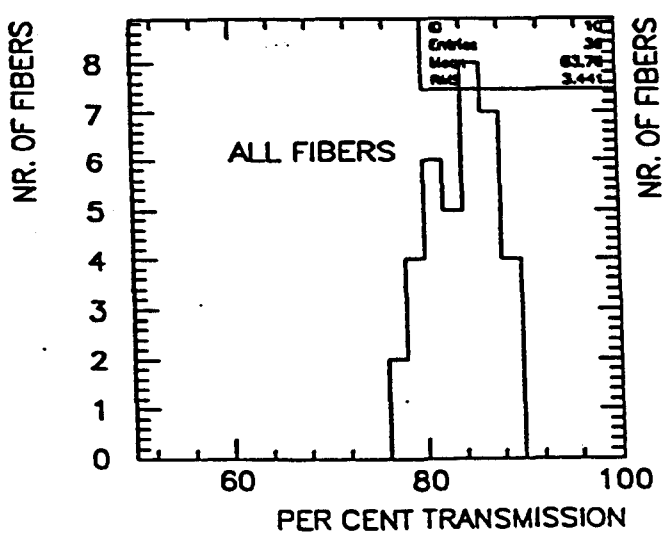

Fig.5-17. Transmission of the multifiber connector. Transmission is measured by comparing light transmission through two 1 m long silica fibers joined by a connector to the transmission through a 2 m long sample.

fiber. In addition to investigating how to coat the silica, we will study the mechanical strength of the resulting fiber; it may be too brittle to sustain the forces when coiled in a small loop in the tile, particularly after irradiation. If so, several smaller diameter fibers may be used per tile. We further speculate that smaller fiber may have added benefit of being flexible enough to be run directly to the phototube, eliminating the connector and the clear plastic fiber.

5.4.3. Light Yield

The amount of light detected can be improved by increasing:

- the amount produced
- the efficiency of capture by the WLS fiber
- the efficiency of transmission to the PMT, or
- the quantum efficiency of the PMT.

The first of these is not easily achievable: it requires either a higher scintillator-to-lead ratio, and therefore a change in the baseline design, or brighter scintillator. We will use better scintillator when it becomes available, but are not actively researching this area ourselves.

The capture efficiency may be improved by better wrapping (such as Tyvek) and edge painting. More substantial improvements are possible with two loops of WLS fiber instead of one. The tradeoff may be greater sensitivity to radiation damage.

Since a factor of 3 in light yield is lost in transmission from the end of the WLS fiber to the end of the clear plastic, substantial improvements are possible. Acrylic fiber or high numerical aperture polystyrene fiber (multiclad) have a significantly longer attenuation length than BCF-98 and will be studied as replacements. The connector/splice loss between this fiber and the silica due to fiber misalignment may be reduced by using a slightly larger diameter for the plastic.

Much of the loss in transmission is due to numerical aperture mismatch between the BCF-91A and the silica. Replacing the BCF-91A with coated silica, as discussed above, will not regain this light (there would be no mismatch, but the fraction of light captured in the WLS part of the fiber would be less), but would eliminate the transmission loss at the splice.

The shower-maximum group is investigating several readout possibilities, such as APD's and PMT/APD's, that have higher quantum efficiencies than the green-extended phototubes now in use. These devices could be used if they are cost effective and satisfy all other requirements.

5.5. Optics System References

[5-1] M. Hoff, "Scintillator Fabrication of the 4x4 Calorimeter Test Station Module", LBL-SD-020209,(1992)

[5-2] C. M. Miller,*Optical Fiber Splices and Connectors* (Marcel Dekker, New York, 1986), p. 95.

6. Test Beam Results

To test our ideas about the calorimeter structure and to create a test station for optical, electronic and calibration issues we constructed a $25X_o$ deep test station module with 16 towers. This calorimeter test station module has been tested at the A3 test beam at Brookhaven National Laboratory. Some of the measurements on components for this module have been described in the previous section on optics. In the following sections we describe the mechanical structure of the calorimeter module, the test beam setup, track reconstruction in the beam line chambers, results of source calibrations, electron resolution and uniformity scans across spokes and cracks between towers of the calorimeter module.

6.1. Calorimeter Test Station Module

The principle design requirement for the test station module was that it reproduce all of the essential physical parameters of the endcap monolithic EM calorimeter design as follows:

- The module should be 25 X_o deep.
- Two longitudinal compartments per tower
- Realistic optical system with BCF91A WLS fiber, in a sigma patten inside a 4 *mm* thick tile of SCSN81. The WLS fibers were required to be spliced to clear silica fiber, which was in turn spliced to a clear plastic fiber.
- Nearly exact reproduction of the "unit cell" in the ECEM including lead, scintillator tiles, aluminum curtains and fiber routing spaces
- Towers tilted in at least coordinate.
- Space and materials simulating a realistic shower maximum detector
- A bicycle spoke plus bushing penetrating each tile
- Well defined gaps between towers to measure the effect of cracks on the calorimeter response

Items *not* considered essential to the module were:

- Trapezoidal tiles. We used tiles with a square 11 *cm* x 11 *cm* area.

- Mechanical support: While all the pieces for the mechanical support were present, the weight of the lead was carried on an external box, rather than on the bicycle spokes.
- Shower Maximum simulation: The materials of the shower maximum detector were simulated. However, there was no requirement for an "active" shower maximum detector.
- Photodetectors: We used commercially available 38 *mm* diameter Hamamatsu R580-17 photomultiplier tubes with extended green photocathode.
- Fiber and source tube routing: These were done as convenience dictated rather than simulating the ECEM. We tried to keep the total fiber length as appropriate for the ECEM. The source tubes were placed so as to cross the center of each tile.

The final design for the test station module is shown in Fig. 6-1, and the parameters of module are listed in Table 6-1. In the plan view we see the edges of the 22 6.35 *mm* thick absorber plates, alternating with gaps for the scintillating tiles and fiber routing paths. The separation of the absorber plates is determined by aluminum bushings around the bicycle spokes. The edges of the four scintillator tiles in each layer can also be seen, offset progressively further to the left, as the figure is viewed from bottom to top. The tower boundaries are parallel to the edges of the scintillator. The "stair step" of each successive tile in a tower follows an angle of $\approx 13°$, approximating a pseudo-rapidity boundary of $\mid \eta \mid = 2.2$. The 16 tiles in each layer are identical, including the 3 *mm* diameter hole for the bicycle spoke. However, because the tower boundary is stepped by 13° in one coordinate, the location of the spoke hole in each layer of the calorimeter changes linearly with its depth inside the calorimeter.

In the elevation view (Fig. 6-1 b) the tiles are arranged into a 4 x 4 array of 16 towers, each tower $25X_o$ deep. The spokes penetrate both the absorber and scintillator tiles and the spokes are perpendicular to the absorber plates. The horizontal tower boundaries are perpendicular to the face of the tiles. Here we purposely introduced three well defined cracks of 0.4 *mm*, 0.2 *mm* and 0.6 *mm* between the four rows of towers (top to bottom). Our intent was to measure the energy lost as a function of the width of the crack between towers. The 0.2 *mm* crack was simply the thickness of the two painted surfaces of neighboring tiles when butted up against each other. The other two cracks were made by inserting 0.2 *mm*

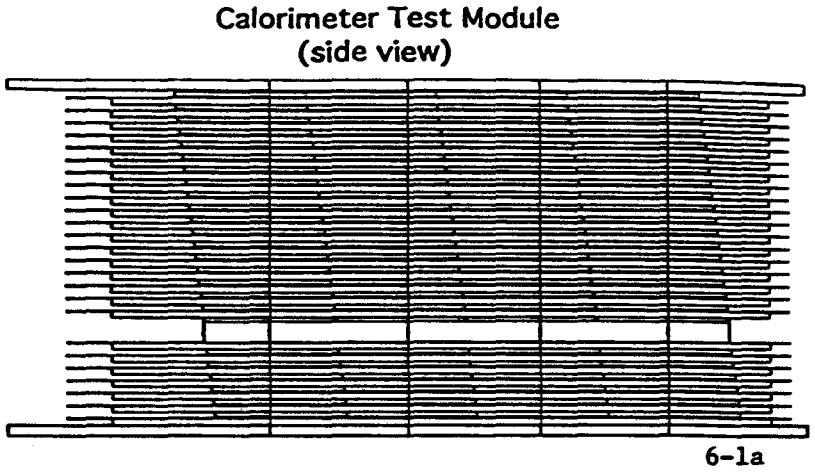

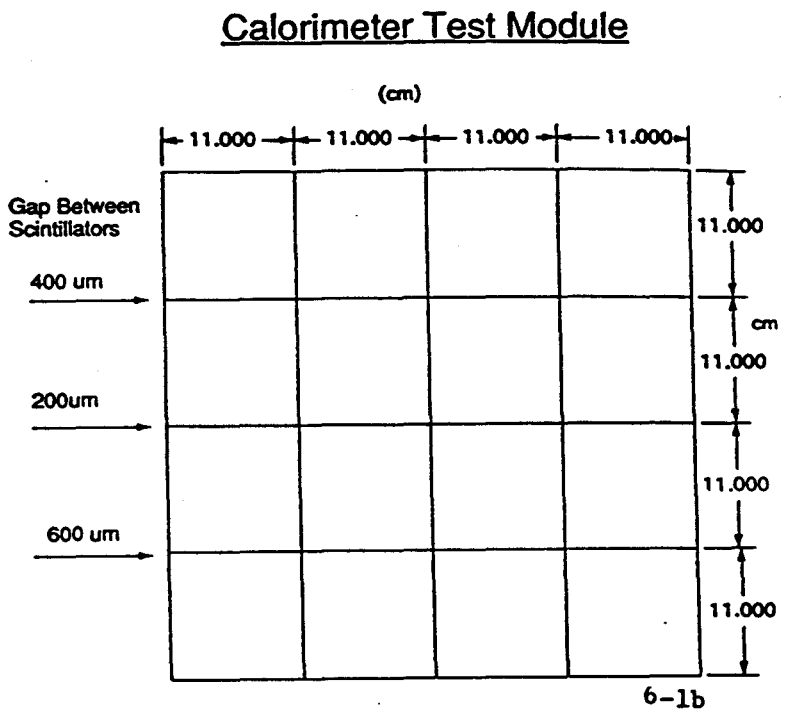

Fig.6-1. a) Plan view of the calorimeter test station module. b) elevation view of the calorimeter module.

and 0.4 *mm* mylar between neighboring tiles. The location of the tiles and mylar inserts were maintained by spring loading the tiles with a neoprene elastomer at the outer edges of each 4x4 tower layer.

The optical design of the tiles has been previously described. Recall that the fiber routing groove in each tile is identical, consisting of a keyhole cross-section groove 10 *mm* from the edge of the tiles and 1.6 *mm* deep. The clear plastic readout fibers, already polished, were glued into 1.066 diameter holes drilled in a circular pattern in a PVC "cookie", as shown in Fig. 6-2.

External light was excluded from the entire assembly by putting the calorimeter, readout

Table 6-1: Parameters of the Calorimeter Test Station Module

Parameter	Value
Depth	$25X_o$
Number of Towers	16
Depth of Front EM1 (Back EM2) section	$5.6X_o$ ($19.4X_o$)
Absorber	97.9% Pb - 1.5% Ca - 0.6% Sn
Thickness of Absorber	6.35 *mm*
Scintillator	Kuraray SCSN 81
Thickness of Scintillator	4.0 *mm*
Tile Size	11 x 11 cm^2
Aluminum curtain thickness	1.5 *mm*
Bicycle spoke diameter	1.60 *mm* Al
Bushing diameter (inside scintillator)	2.54 *mm*
Fiber diameter	1.0 *mm* nominal (all fibers)
WLS Fiber	Bicron BCF 91A
WLS Fiber length	40 *cm*
Light Enhancement due to mirror at end of WLS fiber (measured at end of clear fiber)	29%
Clear Fiber	Bicron BCF 98
Clear Fiber Length	1300 *mm* nominal
Silica Fiber	3M -1.0 -UMT
Tile edge paint	Bicron BCF 620, 3 applications
Tile Wrapping	0.12μm aluminized mylar
Silica Fiber length	1000 *mm* nominal
Fiber routing gap height	2.0 *mm*
Diameter of spoke hole in Scintillator	3.17 *mm*
Depth of WLS groove	1.65 *mm*
Diameter of groove at bottom	1.30 *mm*
Distance from edge of tile to groove	9.52 *mm*
Minimum WLS fiber bend radius	25.4 *mm*
Photomultiplier Tube	Hamamatsu R580-17
Light Mixer	25 x 25 x 75 mm^3 UVA Lucite
Cookie	40 *mm* dia x 10 *mm* thick Grey PVC
Extension of fibers beyond cookie	0.25 *mm*
Air gap between fibers ends and light mixer	1.0 *mm*
Splice tube material	Stainless Steel
Splice tube ID (OD)	1.52 (1.83) *mm*
Source tube material	Brass
Source tube ID (OD)	0.86 (1.57) *mm*
Small Tube Supplier	Small Parts, Inc, Miami,FL

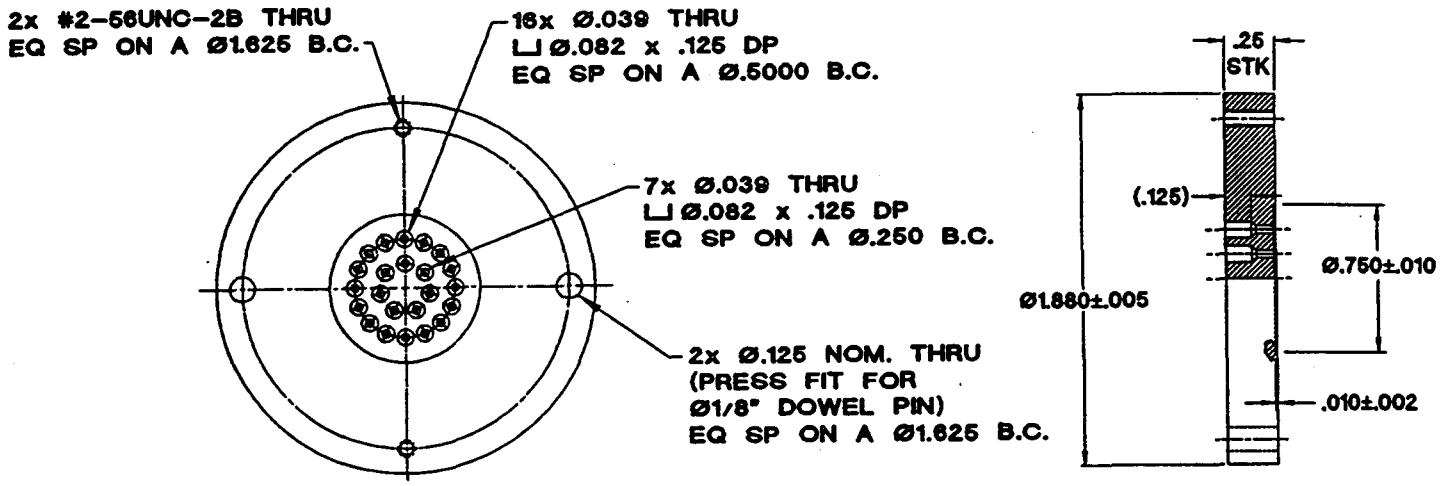

Fig.6-2. Drawing of a "cookie", manufactured from PVC. The fibers were polished prior to insertion into the cookie. The slight recess allows the fibers to extend a pre-determined distance out of the cookie. In their final configuration a 1.0 *mm* thick spacer is placed to space the fiber ends away from the light mixer

fiber and photomultipliers in a common light tight box. The box, shown in Fig. 6-3, was designed to allow access to both ends of the PMT's, a feature needed for dressing of fiber bundles and installation of the phototubes.

Each tile in the calorimeter is crossed by a source tube located in the fiber routing gap. Every source tube successively passes by the geometric center of 4 tiles in a row. There are, therefore, 4 tubes x 22 layers = 88 source tubes in the calorimeter.

In Fig. 6-4 we show a sideview of the calorimeter module indicating the routing of the fibers and the source tubes. The $\approx 13°$ tilt of the tower boundaries is also visible. Fig. 6-5 shows a detailed view of an individual tile in the stack. Fig. 6-6 shows the full calorimeter assembly including the 32 photomultiplier tube housings. Finally, in Fig. 6-7 we show the numbering scheme used to identify the 16 towers.

6.2. Test Beam Setup

We tested the EM calorimeter test station module at BNL using the A3 beam line during the summer of 1992. We took data mostly at 10 GeV/c (triggering on electrons and muons) except for a few runs taken at 1, 2, 5, and 15 GeV/c for an energy scan. The orientation of the calorimeter module in the test beam is shown in Fig. 6-8.

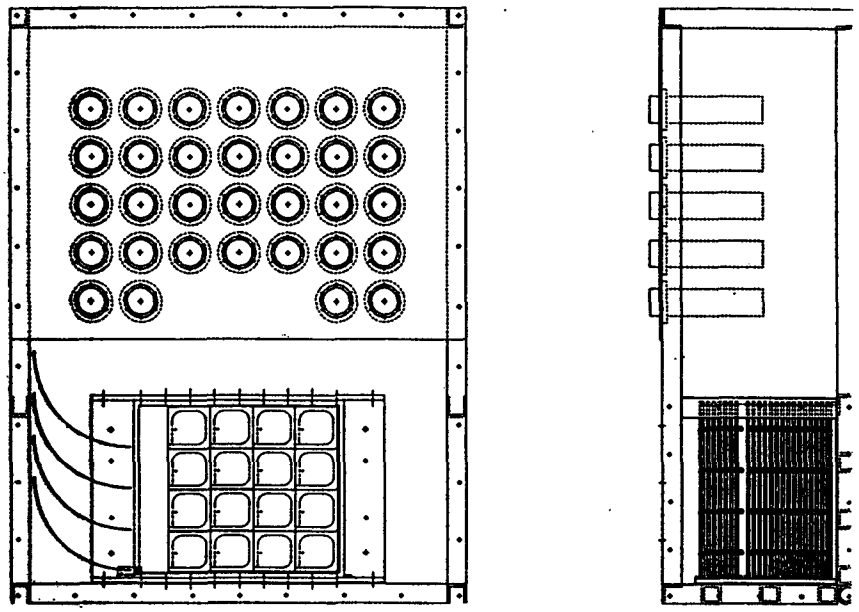

Fig.6-3. Mechanical drawing of the light tight box holding the calorimeter. The box was designed to allow access to both ends of the PMT's, needed for dressing the fibers and installing (or replacing) the photomultipliers.

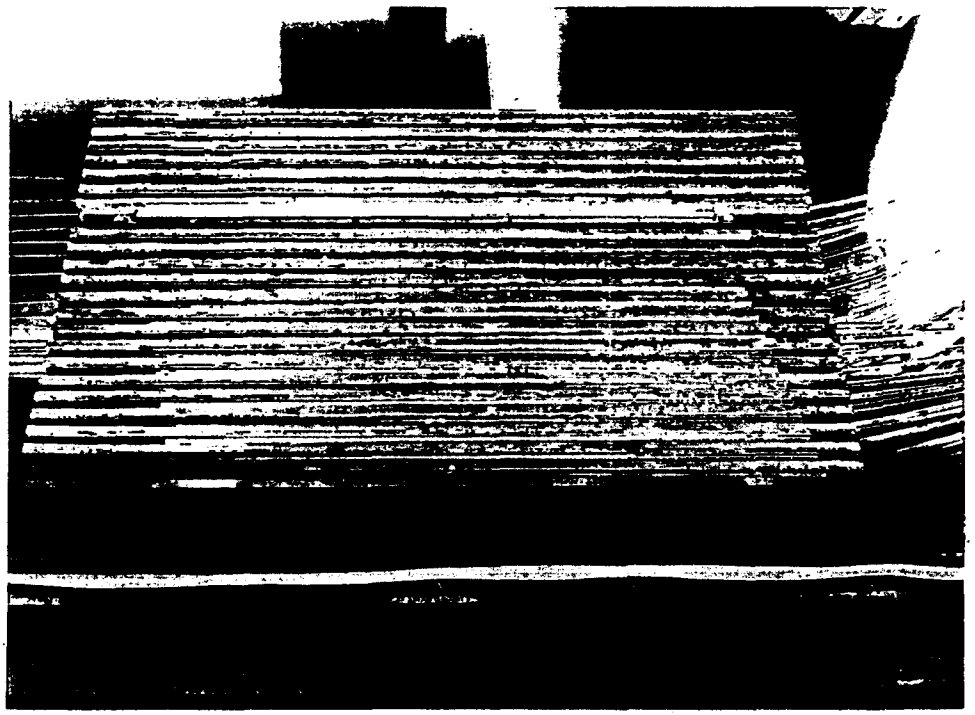

Fig.6-4. A picture of the side of the calorimeter showing the routing of the silica fibers (LHS) and the source tubes (RHS) on either side of the calorimeter (center).

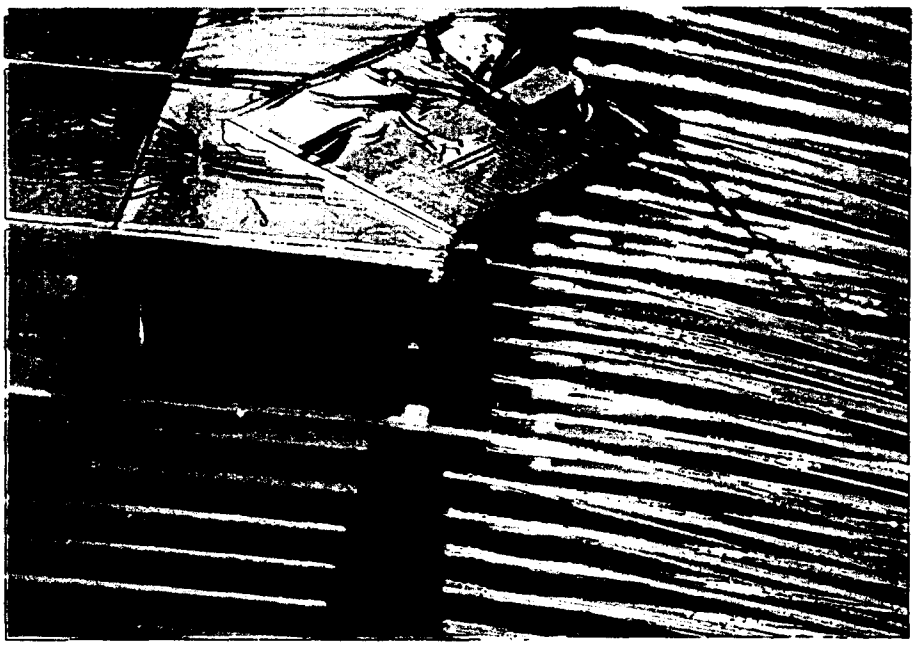

Fig.6-5. Picture of an individual tile just before placing it into the calorimeter stack. Visible are the bicycle spoke with its bushing and the brass source tube. Just barely visible at the RHS of the tile is the hole through which the bicycle spoke penetrates the tile.

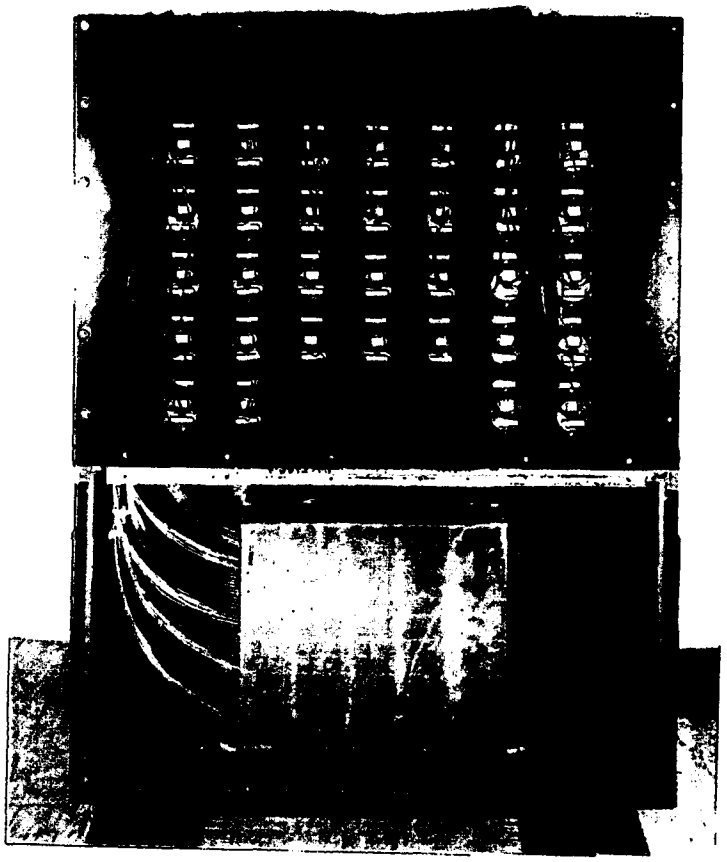

Fig.6-6. Picture of the front of the calorimeter module with its front plate removed. The calorimeter stack is in the center at the bottom of the light tight box The silica fibers are visible on the LHS of the module, and the source tubes are on the RHS.

Top

1	2	3	4
5	6	7	8
9	10	11	12
13	14	15	16

Beam into page

Fig.6-7. The numbering scheme used to identify the 16 towers of the test station module.

The calorimeter modules is at $\approx 13°$with respect to the beam, so that beam particles enter the face of the calorimeter in a direction analogous to the geometry of the ECEM as it would be installed in SDC. The module was supported by a transporter* that could be remotely moved in the horizontal (x) and vertical (y) directions, as was necessary for crack scans and tower to tower calibrations. The A3 beam line layout included scintillation trigger counters, a finger hodoscope, two Cerenkov counters to tag electrons and muons and drift chambers located before and after the dipole magnets to reconstruct the particle trajectories and momentum. We did not use the upstream drift chambers and relied instead upon the nominal beam momentum to test the linearity of the calorimeter. A schematic of the beam line is shown in Fig. 6-9.

6.2.1. Scintillation counters

Four different scintillator paddle detectors ($S1, S2, S3, Veto$) were used in the trigger. Counter $S1$ was made large enough (7.5 cm x 7.5 cm) to cover the beam spread, $S2$ was made of the same dimension (5 cm x 2.5 cm) as the hole in the $Veto$ counter and positioned

* The transporter table was provided courtesy of the GEM/Sulak/Bromberg group.

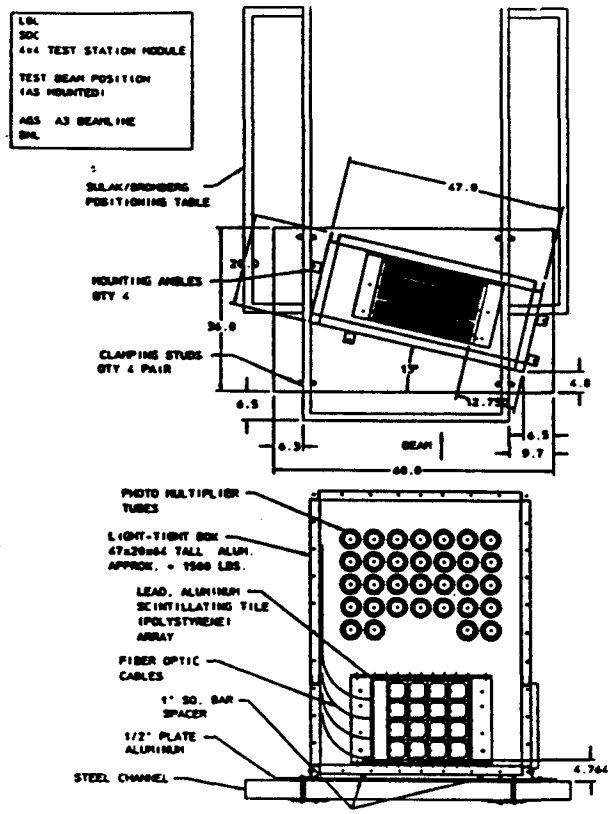

Fig.6-8. Plan and elevation views of the calorimeter test beam module in the A3 beam line at BNL. Note that the beam line is parallel to the edges of the tiles and the bicycle spoke supports are at an angle of $\approx 13°$ with respect to the beam direction.

to cover it. The *Veto* counter was made of 16 individual paddle detectors. The hole in the middle measured 5 *cm* wide and 2.5 *cm* high. Counter $S3$, the muon tagging counter, was located behind the calorimeter and $\approx$ 5 *cm* of lead. It was made larger than the other two paddle detectors (10 *cm* x 10 *cm*) to shadow the beam after taking into account the effects of multiple scattering. The analog output from this counter was also recorded in one of our ADC channels. Signals from the phototubes connected to the four trigger counters were discriminated and the generated NIM pulse was used in the trigger logic. In addition the output from $S3$ was split into two discriminators indicating the low threshold and high threshold for this counter to be used in the trigger. Counter $S2$ defined the timing for the experiment on an event by event basis.

6.2.2. Finger hodoscope

The finger hodoscope was made with 1 *mm* diameter scintillating fibers in two orthogonal layers in the x and y directions. The number of fibers per photodetector varied with distance to the center of the hodoscope; with the finest granularity of 1 fiber per PMT near the center

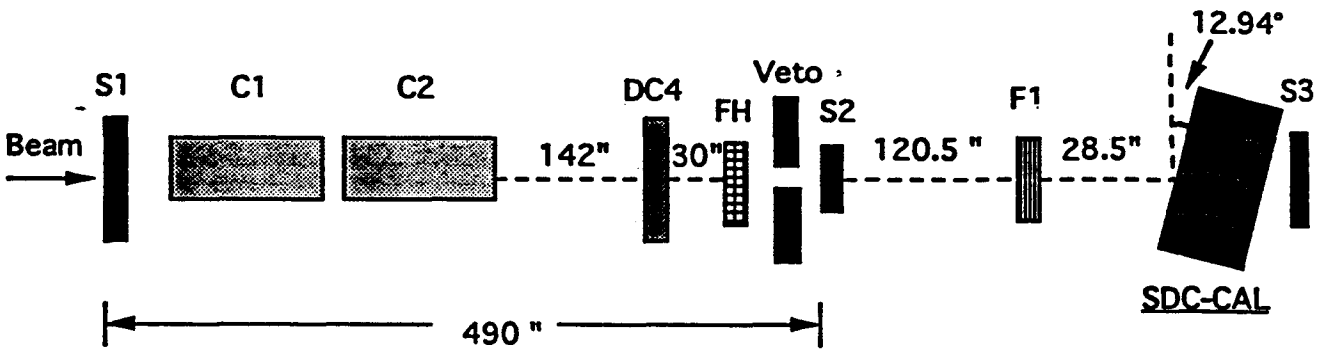

Fig.6-9. Schematic drawing of the A3 beamline at BNL, defining the names of the scintillation counters S1, S2, S3 and the veto counter, as well as the relative locations of the Cerenkov counters C1 and C2.

of the beam line. The fibers (or groups of them) were coupled directly to photomultiplier tubes. There are 28 channels in the x direction and 12 in the y direction. Figure 6-10 shows the channel mapping and the correspondence between fibers and channels.

The spatial resolution of the hodoscope is better than 1 mm in the central region where there was 1 fiber per photomultiplier tube. The finger hodoscope was located at about 4.24 m in front of the calorimeter and 30 cm downstream of DC4. The information obtained from the hodoscope together with the data from the tracking chambers, DC3 and DC4, were needed for full, unambiguous reconstruction of the events.

6.2.3. Cerenkov Counters

Two identical Cerenkov detectors were used in the test. They were made of an Aluminum pipe, 15 cm in diameter and 335 cm long, and with mylar windows on both ends. The pipe contained CO_2 gas at a pressure which could be remotely adjusted. A mirror placed inside the aluminum pipe reflected and focused the Cerenkov radiation onto a PMT.

Figure 6-11 shows the threshold pressure for the case of CO_2 as a function of the mo-

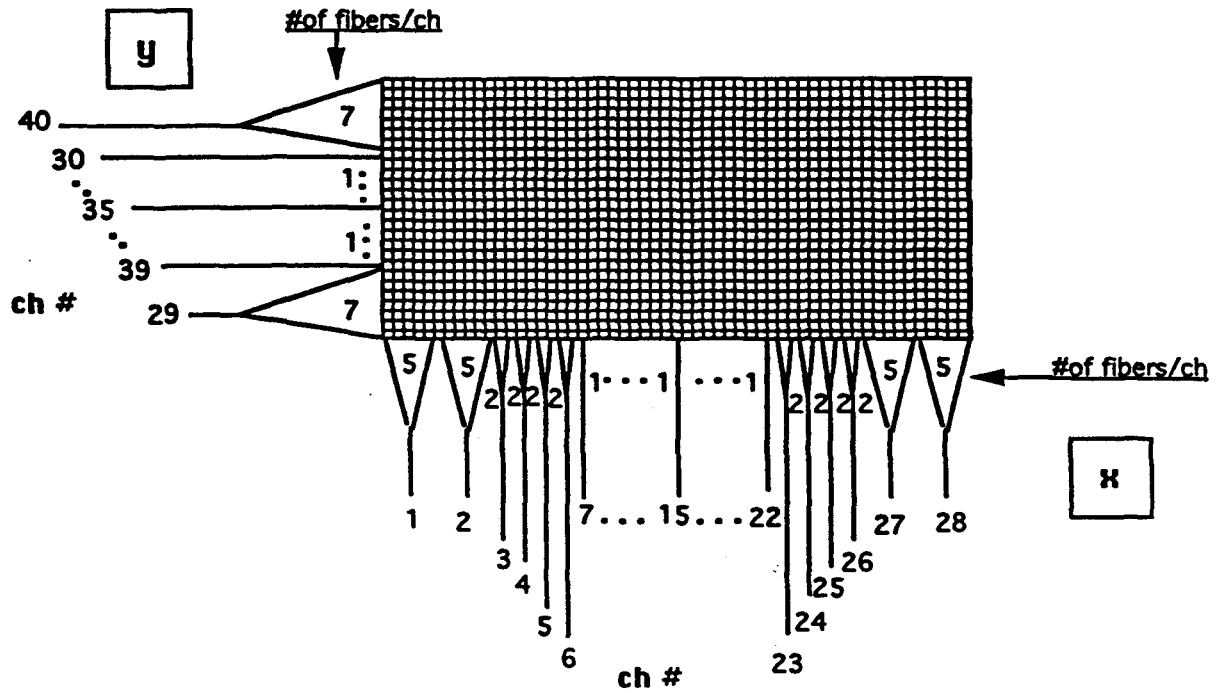

Fig.6-10. Schematic diagram of the finger hodoscope, showing the grouping of the fibers into the electronics channels

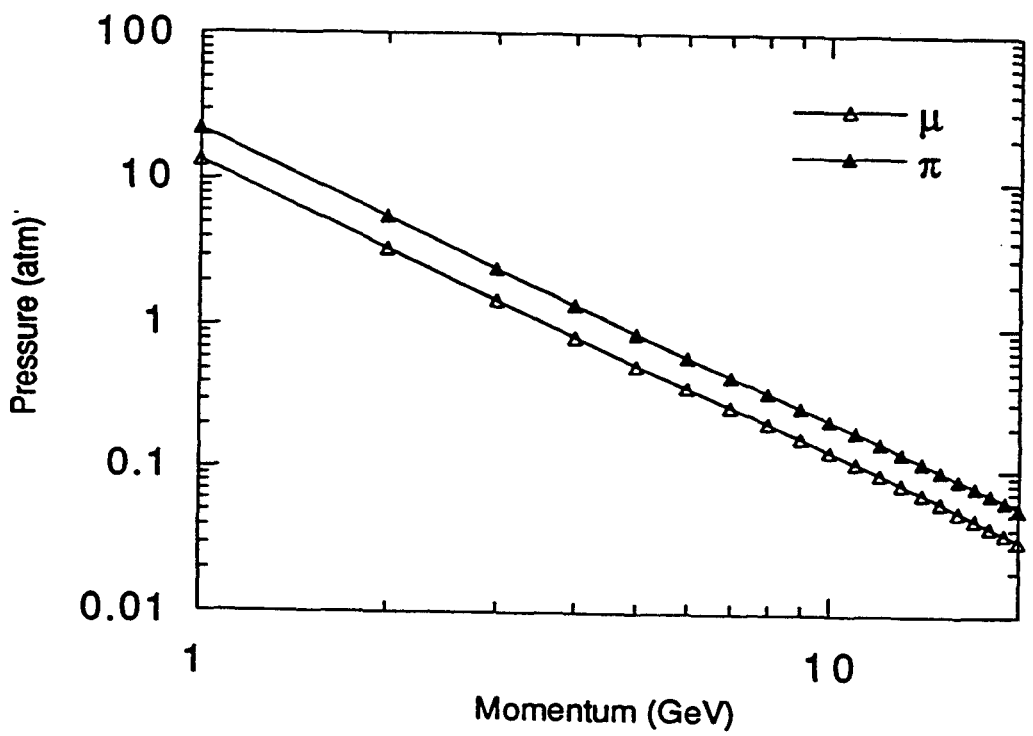

Fig.6-11. Threshold pressure for pions and muons in the CO_2 Cerenkov counter.

mentum for pions and muons. The pressure of the gas in the counters was set above or below the muon, electron or pion threshold pressure depending on the required trigger. In particular, for the electron trigger we set the pressure in the Cerenkov counters below the pion and muon threshold so that only electrons produced Cerenkov signals. Electron events are then separated from pion simply by requiring a signal in both counters. Table 6-2 shows operating points for C1 and C2.

Table 6-2 : Cerenkov Counter Operating Conditions

PMT Voltage	Pressure (kPa) Momentum			
C1 (C2)	5	10	15	20 (GeV/c e-)
2700(2400)	60.6	91.0	97.5	99.0

6.2.4. Trigger System

The mechanical layout of the trigger detectors was shown in Fig. 6-9. The basic coincidence consisted of $S1 * S2 * \overline{Veto}$ and was defined as the $BEAM$ trigger. The trigger for electron was defined as $BEAM * C1 * C2$. The trigger for muon was defined as $BEAM * C1 * C2 * S3_{low}$. The pressure of the gas in both Cerenkov counters was set at 91 kPa for 10 GeV/c electrons and at 80 kPa for muon trigger.

6.2.5. Drift Chambers

Four sets of drift chambers (DC1, DC2, DC3, DC4) were located along the beam line to provide the direction of the incident particle. DC1 and DC2 were not used in this analysis. DC3 (DC4) was located about 21 m (5 m) upstream from the calorimeter.

In Fig. 6-12 shows a schematic drawing of a drift chamber. Each chamber consists of 3 double planes of wires at 60 degrees from each other, forming a hexagon. Each chamber plane (s, t, or u) had 16 wires, which were offset by $\frac{1}{2}$ the wire-to-wire spacing in the neighboring (s', t' or u') plane. At 16 wires per plane, the total number of wires per chamber is 96. The distance between pairs of sense wires is 16.51 mm in the plane of the wires. The gas mixture used was 90% argon and 10% methane. The voltage applied to the sense wires was 1.66KV.

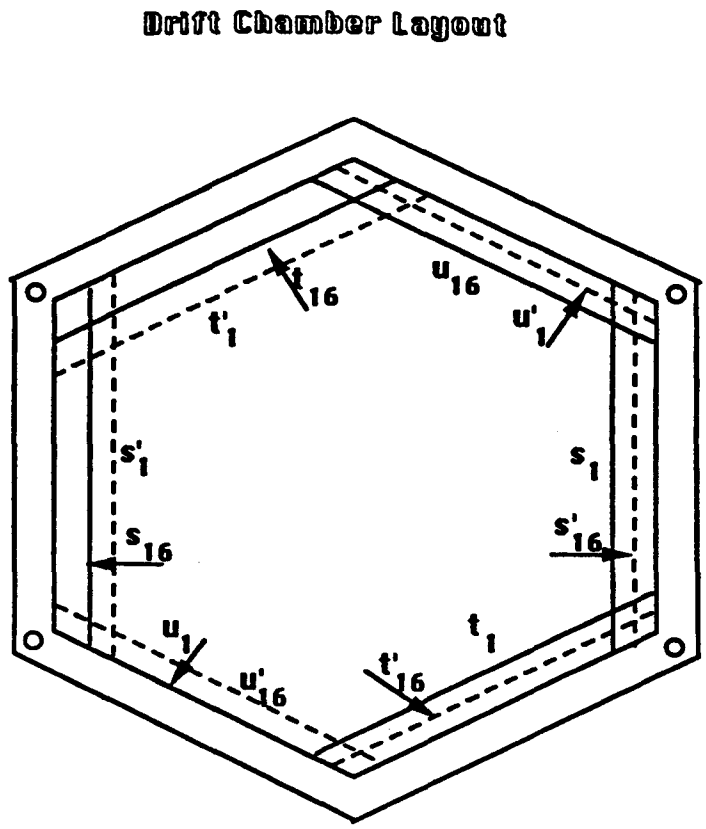

Fig.6-12. Schematic drawing of a drift chamber double plane.

6.2.6. Electronics and Online DAQ

In Fig. 6-13 the data aquisition electronics is shown. The signals from the 32 photomultiplier tubes of the calorimeter were digitized by a CAMAC based LRS 2280 system employing a LRS 2282A a 12 bit, current integrating ADC. To match the dynamic range of the ADC's, the photomultiplier signals were first amplified by a set of LRS 222 10× linear amplifiers. The drift chamber signals were read out by the LRS 4290 Time Digitizing System specifically designed for multiwire drift chambers. The system used in this test consisted of a TDC controller (model 4298), 12 channel time digitizers (model 4291B) and a databus interface/buffer (model 4299).

The trigger bits (Cerenkov counter, trigger counters, particle type, etc) and the finger hodoscope bits were read through four LRS2349 registers. The trigger module used in this test was a programmable, custom made CAMAC module from SACLAY ("Porte Rapide") for controlling the generation of the gates for the ADCs and latches. In Fig. 6-14 a schematic of the electronics is shown.

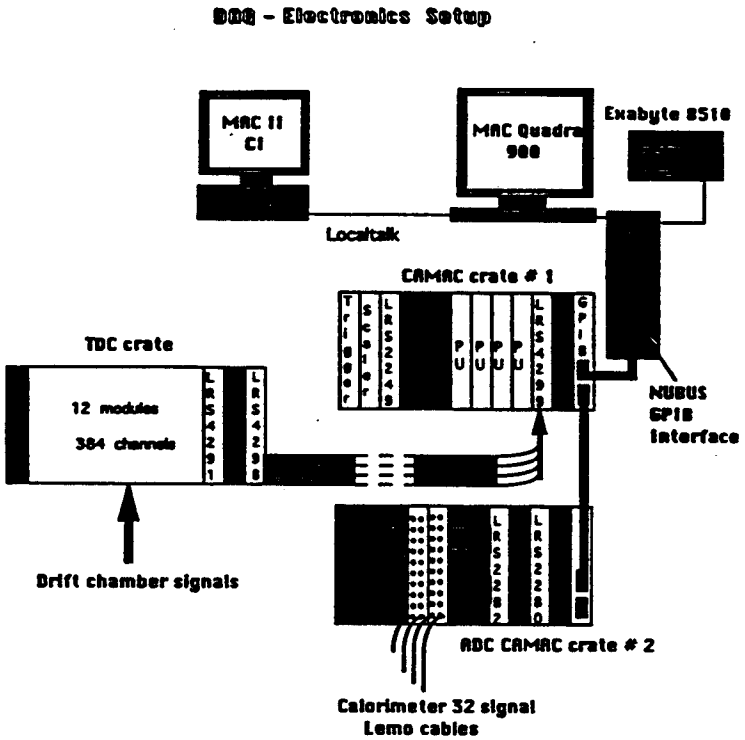

Fig.6-13. Schematic diagram of the DAQ electronics and online computer.

6.3. Drift Chamber Reconstruction

For this analysis only the chambers DC3 and DC4 were used to reconstruct the trajectory of beam particles downstream of the bending magnets. Since the beam is very nearly perpendicular to the chambers (typically no more than 1 or 2 mrad away from the perpendicular), no corrections are made for track angles. Each set of chambers has wires in 3 coordinates (s, t and u) at 60° to each other. The s wires are vertical and measure the x coordinate directly. The t and u wires are at $\pm 60^o$ to the vertical.

Reconstruction of the drift chamber information was a five step process:

1) Figure 6-15 shows the measured time on one drift wire plotted against the time on the neighboring wires in the adjacent plane. As can be seen, the drift time relationship is bi-linear with a break point at roughly 1/4 the cell width. The average drift velocity is about $37\mu m/nsec$. After subtraction of wire to wire t_o's the drift time information was converted into distance using the bilinear time to distance relationship determined from Fig. 6-15.

2) Data from neighboring pairs of wires in the same drift chamber coordinate were exam-

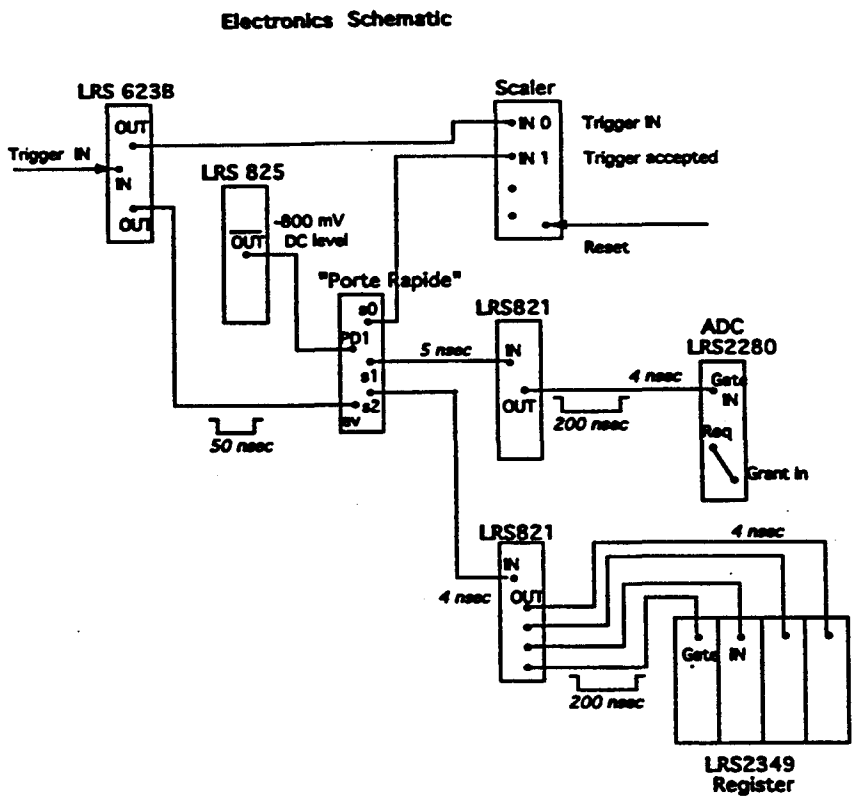

Fig.6-14. Schematic diagram of the trigger electronics, indicating the gate widths to the integrating ADC's.

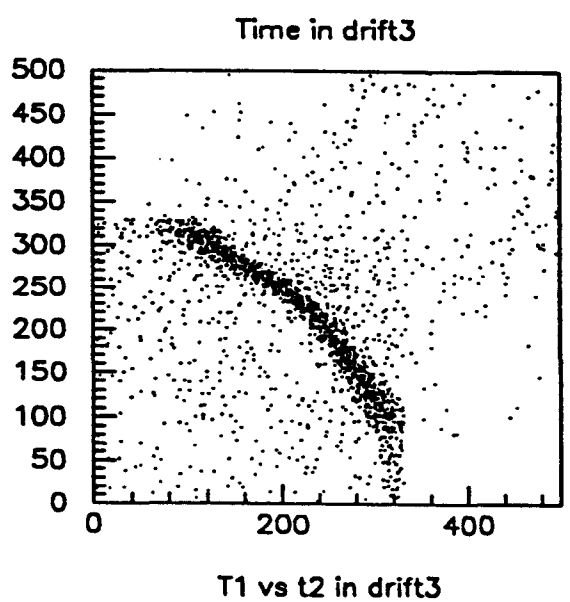

Fig.6-15. A scatter plot of the time measured on one wire versus the time measured on its neighbors in the adjoining plane. The time to distance relationship appears to be non-linear, with a kink at the center of the cell.

ined to see if the sum of the distances measured on these wires corresponded to 1/2 the wire spacing. Valid pairs, where this distance sum was within the expected value of 8.25 $mm \pm 1.0$ mm were retained.

3) Each chamber can produce pairs of hits along three coordinates rotated by 60°. Hence, when all the data is available, the point were the track intersected the chamber is over constrained. Figure 6-16 is a plot of $x(s) - x(u \text{ and } v)$, where $x(s)$ is the horizontal or x coordinate of the track measured from the s wires, and $x(u \text{ and } v)$ is the value of x calculated from the u and v wires. From this plot, the resolution of the chambers is estimated to be $\approx 200\mu$m. In the event that only two coordinates are available, the location of the track in x and y is calculated from the available information.

4) Track coordinates in DC3 are paired with the coordinates in DC4 to compute the particle trajectory. The event is classified into one of three groups:

   - No track
   - Track in the x coordinate only
   - Track in both the x and y coordinates

5) After reconstruction, we determined that in about 1/2 the events the drift chamber information did not appear to correspond to the finger hodoscope information. Figure 6-17 shows the extrapolated position of a track at the finger hodoscope versus the position calculated from the finger hodoscope data. In this plot we see a narrow diagonal band with significant background. Similar effects are seen when comparing track impact points on the face of the calorimeter with the position of a track estimated from tower sharing information in the calorimeter. For this reason we placed a cut on the tracking data, requiring agreement between the finger hodoscope data and the track location at the position of the finger hodoscope. The cut depends on the number of fibers hit, as shown in Fig. 6-18. With this information we are then able to predict the impact of the tracks on the face of the calorimeter.

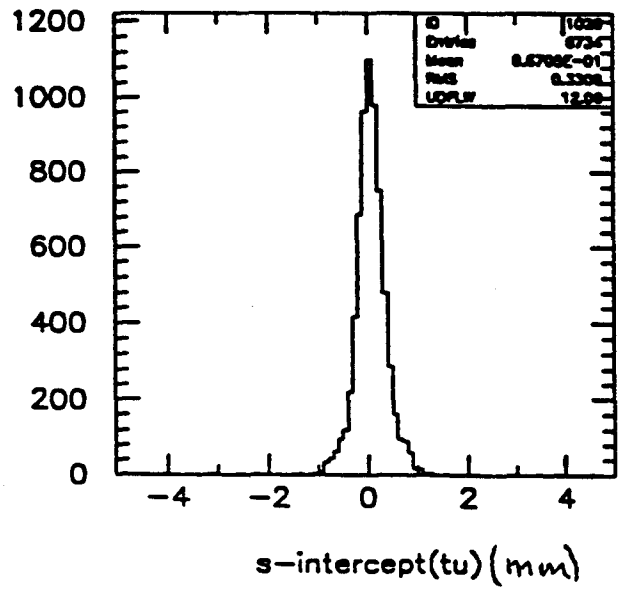

Fig.6-16. Residuals for tracks with positions reconstructed in all three coordinates. The horizonal axis corresponds to $x(s) - x(u$ and v), where $x(s)$ is the horizontal or x coordinate of the track measured from the s wires, and x(u and v) is the value of x calculated from the u and v wires.

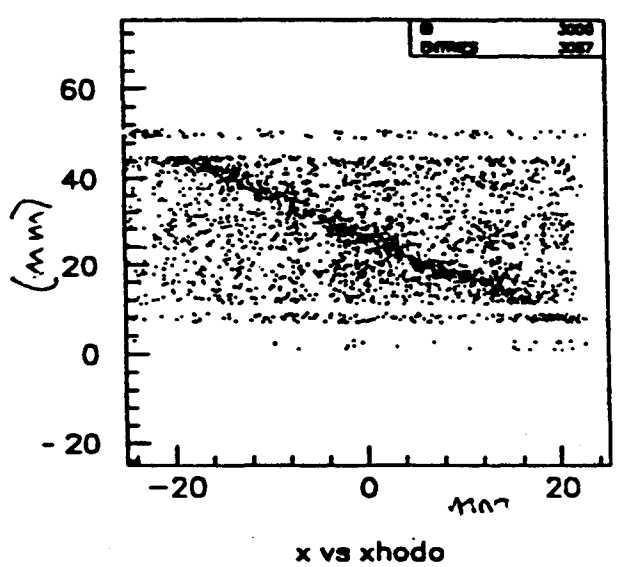

Fig.6-17. A scatter plot showing the position of the track at the finger hodoscope vs the position in the hodoscope. There is a correlated diagonal band of data with a large background.

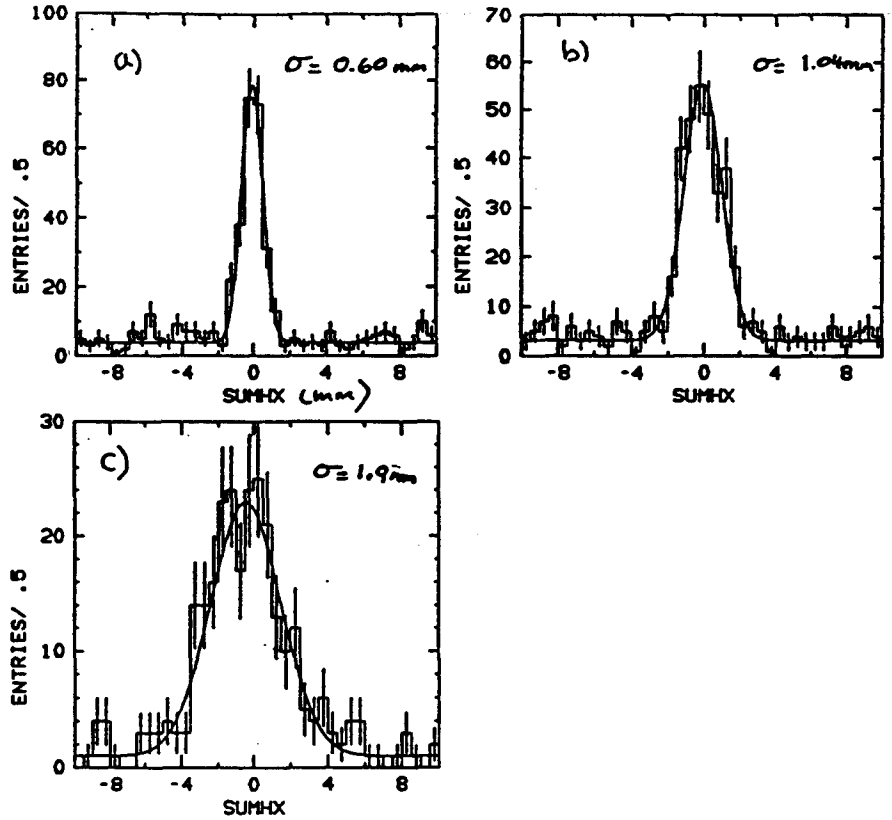

Fig.6-18. Calculated position of the track minus the position of the track as calculated from the finger hodoscope data. The three plots correspond to a) events with 1 fiber, b) 3 fibers and c) 5 fibers.

6.4. Calibrations

Three methods were used to calibrate the calorimeter module and monitor performance: Muons, electrons and source calibrations. We used the muon signal to establish the relative gain between the EM1 and EM2 longitudinal sections of each tower. The tower to tower relative gains were then set using 10 GeV/c electrons. We also tested a radioactive source system for monitoring the overall gain of the detector.

The gain (and gain versus high voltage) of the 32 individual photomultipliers was measured using a standard scintillating tile and Ru^{106} source. The operating voltage of the PMT's was typically 1350V, and the gain varied by about 0.5% per Volt. Pairs of photomultiplier tubes with high voltage operating points close together were matched and used on the EM1 and EM2 sections of the same tower. Our HV distribution system allowed the voltage to be set to ±10 Volts, and two tubes corresponding to the same tower were run at the identical high voltage setting.

6.4.1. Muons

The calibration of the calorimeter with muons is complicated by the dependence of the muon energy deposition as a function of its depth into the calorimeter. Figure 6-19 is a GEANT calculation of the *average* energy deposited by a muon in a scintillator plate as a function of its depth in the calorimeter. There is a rise of about 15% in the energy deposition from the first to the seventh scintillator the front of the calorimeter and the energy deposition per scintillator tile reaches a constant value thereafter.

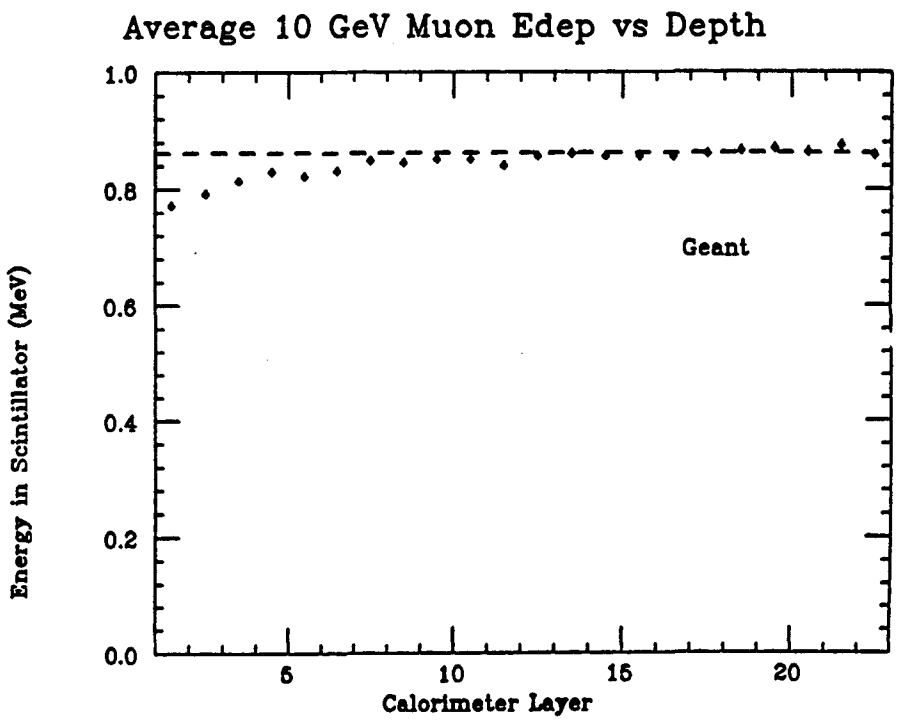

Fig.6-19. GEANT calculation of the *average* energy deposited by an muon versus the layer number in the calorimeter. The horizontal dashed line represents the asymptotic response per layer.

The initial rise in the response near the front of the calorimeter is due to penetrating delta rays and photons whose flux gradually increases versus depth before reaching an asymptotic value. Therefore, the relative gain of the EM1 and EM2 sections is set by fitting the distribution around the *peak* of the energy deposited in each section, rather than the *average* value. This procedure excludes the tails of the distributions and thereby reduces the sensitivity to this effect.

After smearing the Monte Carlo data for the average number of photons and PMT resolution, $peak(\mathrm{EM2})/peak(\mathrm{EM1}) = 2.25 \pm 0.05$ compared to the naive value obtained from

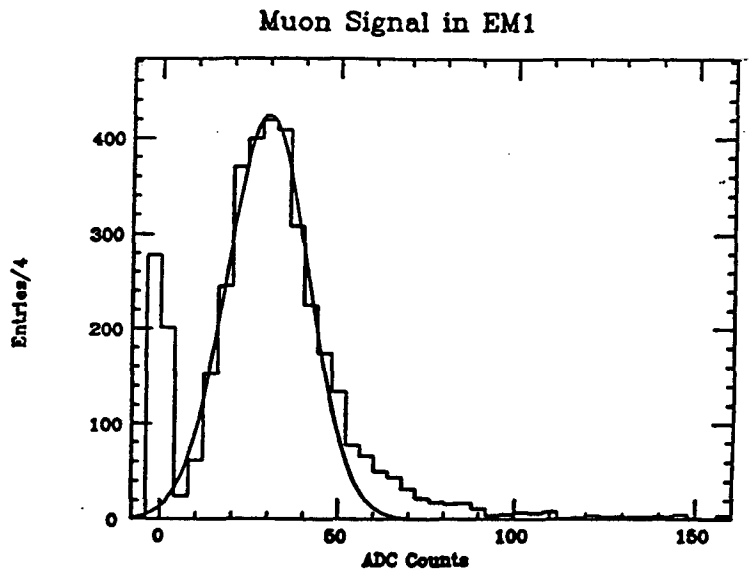

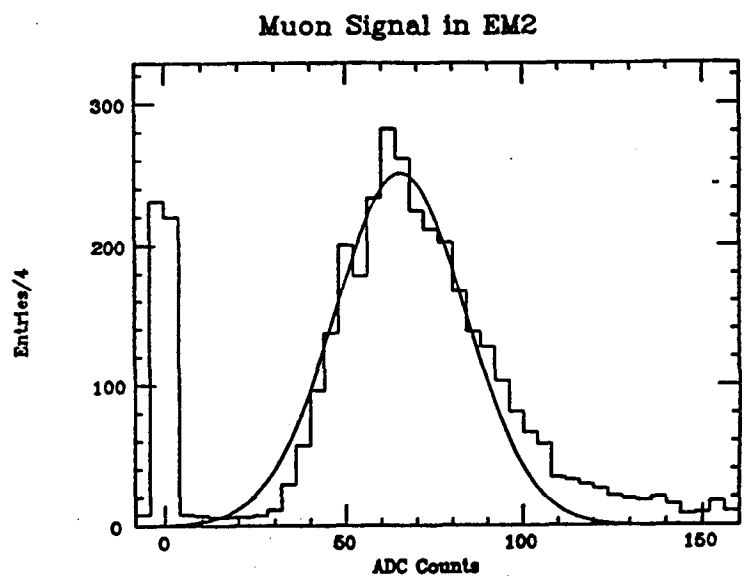

Fig.6-20. Typical ADC distribution for muons in the a) EM1 and b) EM2 Sections prior to calibration. The EM1 section has 7 scintillator plates and the EM2 section has 15 scintillator plates. The smooth curves are gaussian distributions fitted to between the $\pm 1/2$ maximum values of the the central peak.

the ratio of the number of scintillator tiles of $15/7 = 2.14$. The uncertainty arises from different methods of fitting the peak in the simulated data between $\pm\frac{1}{2}$ the maximum value around the cental peak.

Figure 6-20 shows a typical muon distributions for the EM1 and EM2 section of one tower prior to correction. The smooth curves are gaussian distributions fitted to the peak value using the same technique employed for the simulated data. Analogous values, calculated independently for each tower in the calorimeter, were used to fix the relative calibration of the EM1 and EM2 sections.

6.4.2. Electrons

We used 10 GeV/c electrons to adjust the relative tower to tower gains. Figure 6-21 shows oscilloscope traces of the EM1 and EM2 sections, as well as the sum of the two signals.

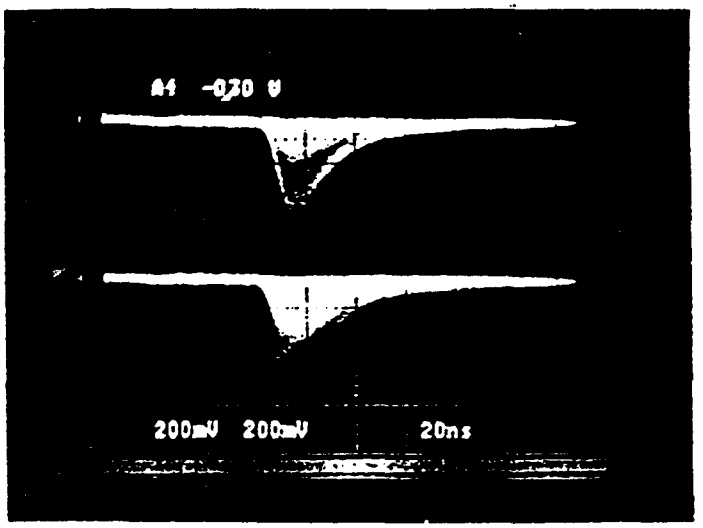

6–21a

6–21b

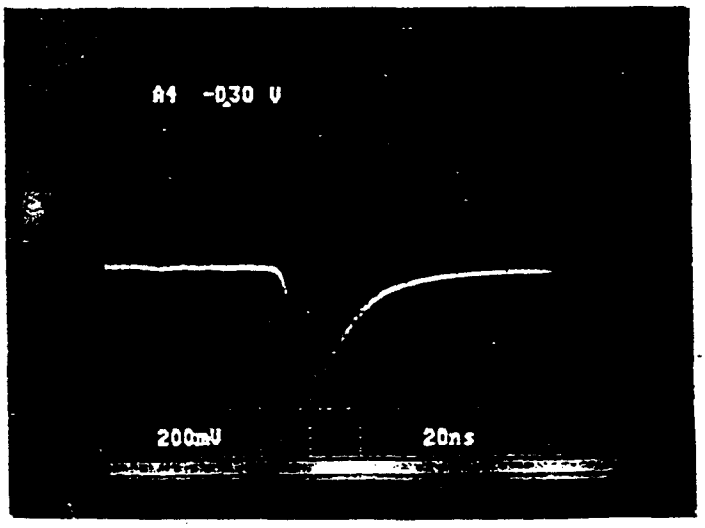

6–21c

Fig.6-21. Oscilloscope traces of the signals from 10 GeV/c electrons in the a) EM1 section, b)EM2 section and c) both sections summed on the oscilloscope. All traces are integrated over the ≈ second spill period.

While the EM1 and EM2 signals are relatively fuzzy, indicative of the fluctuations in the longitudinal energy deposition, the sum is a narrow band reflecting the calorimeter resolution of 5.5% for 10 GeV/c electrons. The relative tower to tower gains (*i.e.* the sum of EM1 and the EM2 sections divided by the nominal value) are histogrammed in Fig. 6-22.

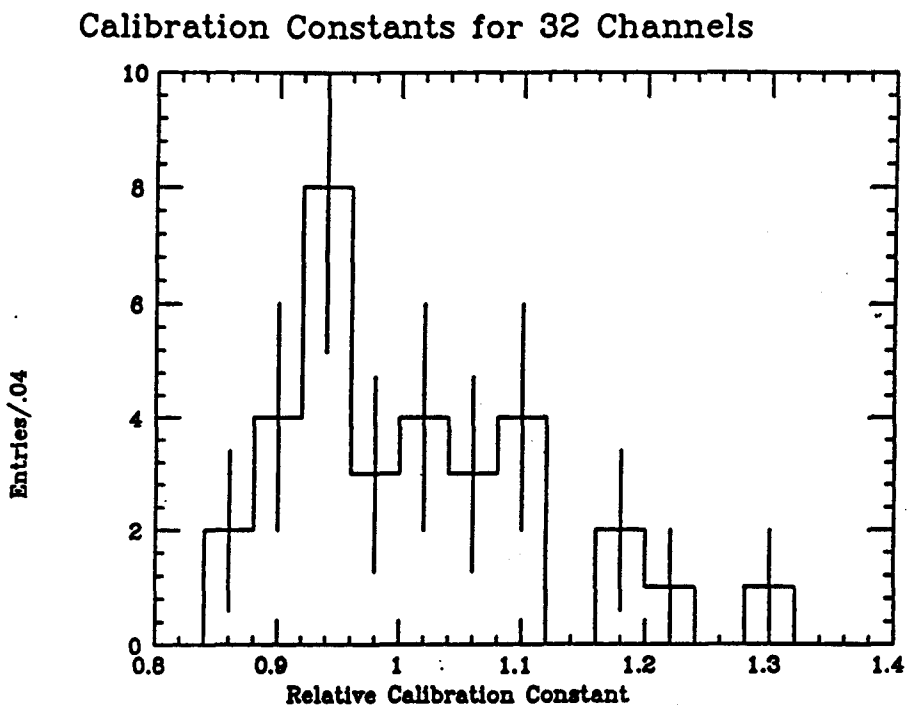

Fig.6-22. Relative tower to tower gains with arbitrary normalization on the horizontal axis. The *rms* of the distribution is 5%.

The *rms* spread of the tower to tower gains is ±5% consistent with gain variations due to the high voltage distribution system.

After determining the relative ratio of the EM1 to EM2 sections and the tower to tower calibrations, we can use EGS code to *predict* the relative signals in the EM1 and EM2 signals.

Figure 6-23 is a plot of the ratio of EM1/EM2 (summed over all towers) for 10 GeV/c e^- together with the EGS prediction, including photostatistics. The average for the data is 0.52 ± 0.006 versus 0.557 ± 0.001 for the EGS simulation. We cannot explain the 6.9% difference. The disagreement is small enough that it does not affect any of the results presented here.

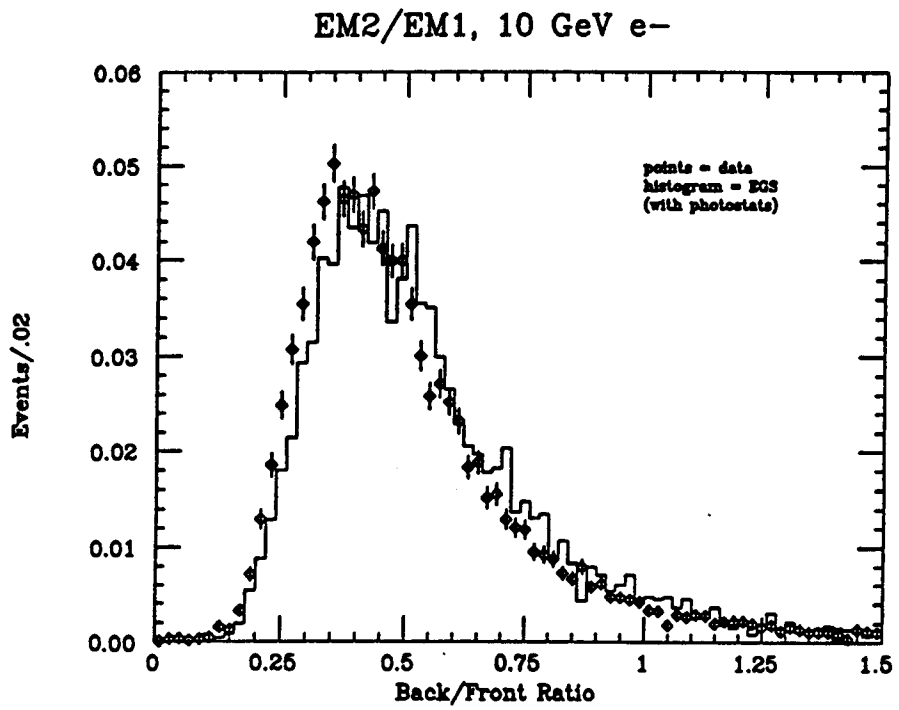

Fig.6-23. Comparison of the EM1/EM2 ratio summed over events as seen in the data (points) and EGS (line).

6.4.3. Sources

Description of Hardware

We used a source and source driver supplied by Purdue University [6-1] employing a 5 mCi Cs^{137} radioactive source to measure the day to day response of the calorimeter. The actual Cs^{137} source consisted of a 380μm diameter wire about 6 *mm* long located at one end of a 6 meter long section of hypodermic tubing with an outside diameter of 685μm. Between each layer of scintillator and its adjoining layer of lead we inserted 860μm inside diameter brass tubes to guide the radioactive source past the center of every scintillating tile in the stack. When not in use, the source is stored in a lead garage integral to the drive mechanism. For the purposes of monitoring, we used only eight of the 88 possible source guide tubes. Four of these tubes are located between the 4th layer of scintillator and the adjoining layer of lead. These provide the monitor locations for the 16 tubes of EM1 section of the calorimeter. The remaining 4 tubes are located between the 13th layer of scintillator and lead and are used to illuminate tiles in the EM2 section of the calorimeter.

Of the 32 photomultiplier tubes in the calorimeter, the phototubes corresponding to

towers 1 through 8 were powered from one high voltage supply and the remaining phototubes for towers 9 through 16 were powered from a second supply. In addition to the 32 photomultiplier tubes in the calorimeter, we used another two phototubes to monitor the high voltage. Each of these photomultiplier tubes was connected to one of the two supplies and viewed a common piece of 4 *mm* thick SCSN-81 scintillator irradiated by an 250 nCi Am^{247} source. The typical current in the HV monitor phototubes was 150 *namp*.

Measurement Technique

A typical source calibration drive consists of three steps:

1. The source is driven from its garage location to the end of a brass guide tube in the calorimeter. The end of the guide tube is plugged and provides the reference location for start of the source run.
2. With the source at the end of its travel, we begin monitoring the current in each of the 4 photomultipliers corresponding to the 4 towers under test.
3. The source is slowly withdrawn from the calorimeter at about 1 *cm/sec* while the current in each of the corresponding photomultipliers is recorded. The current in each photomultiplier tube is measured once every 0.4 *sec* for up to 40 *sec*.

The current from each of the 4 photomultipliers corresponding to the towers under test is monitored with one of four Keithly Model 485 pico-ammeters. These pico-ammeters are read out over a GPIB interface to a Mac-IIci personal computer running LABVIEW^{TM} software [6-2]. The source driver system is independent of current monitor hardware and software and no attempt was made to readback the physical location of the source as it is driven past each tile. Judging by the reproducibility of the readback when the source is parked at the end of a guide tube, we estimate the accuracy of the source readback to be about 1 *cm* along the guide tube.

Fig. 6-24 shows the measured values of the 4 currents versus time for a typical run. As the run begins, the source is stationary near the edge of the left most tile. We then start the motor (at time = 6 *sec*) and pull the source through the calorimeter, ultimately to return it to its garage location. The current in this first tile peaks as the source passes near the center of the tile (time = 8 *sec*) and then rapidly declines as it passes the right edge of the tile,

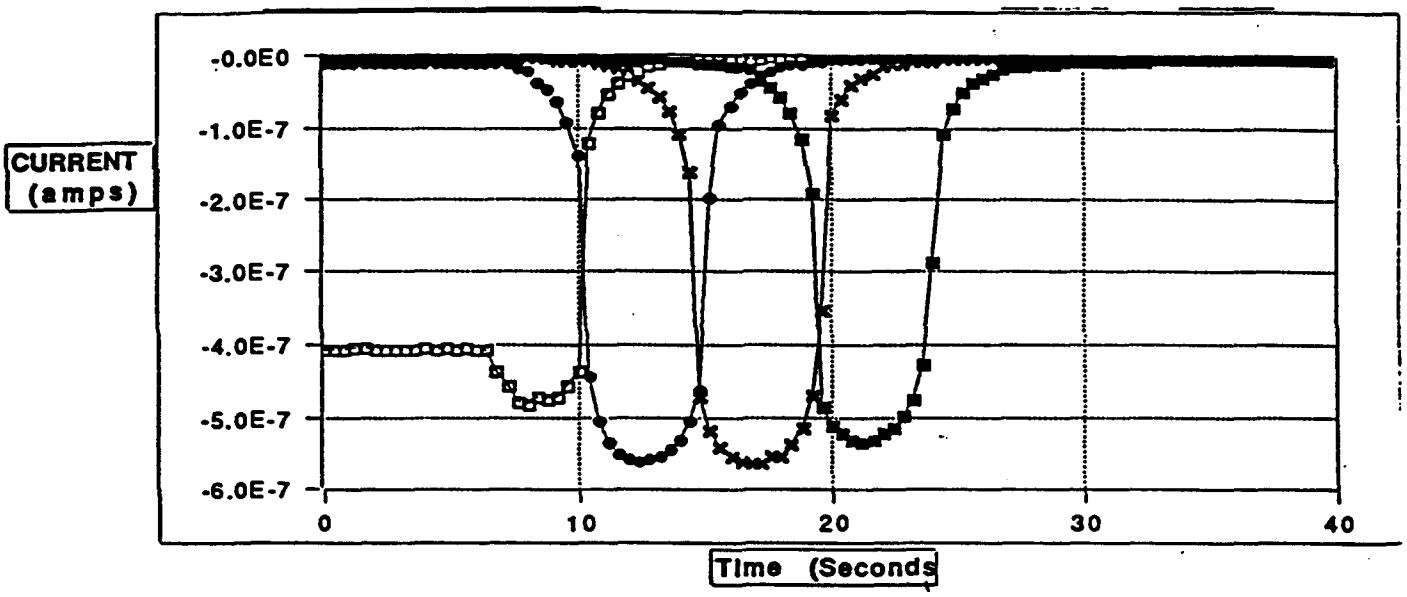

Fig.6-24. Currents measured in 4 photomultipliers versus time during a typical source run. See text for an explanation.

just as the current in the neighboring tile begins to increase. The measured peak current in each tube is typically about 0.5 μamp.

Source Current Reproducibility

We analysed the data in two ways: 1) We fit the 5 measurements of current versus time near the peak with a parabola and used the maximum current from this fit as a measure of the current and 2) we used the peak current per channel directly as measured. Implied in the first method is the assumption that the source driver moves the source with a constant velocity and the DAQ system measures the current at uniform time intervals.

Figures 6-25 and 6-26 show the currents over 4 days for the "fit" and "peak" currents, respectively.

In both cases the average currents are about 0.52 μamp with an rms spread of about 10% of this value. Figure 6-27 shows the relative channel to channel differences between the two techniques. On average the two techniques give the same results to about 2 parts

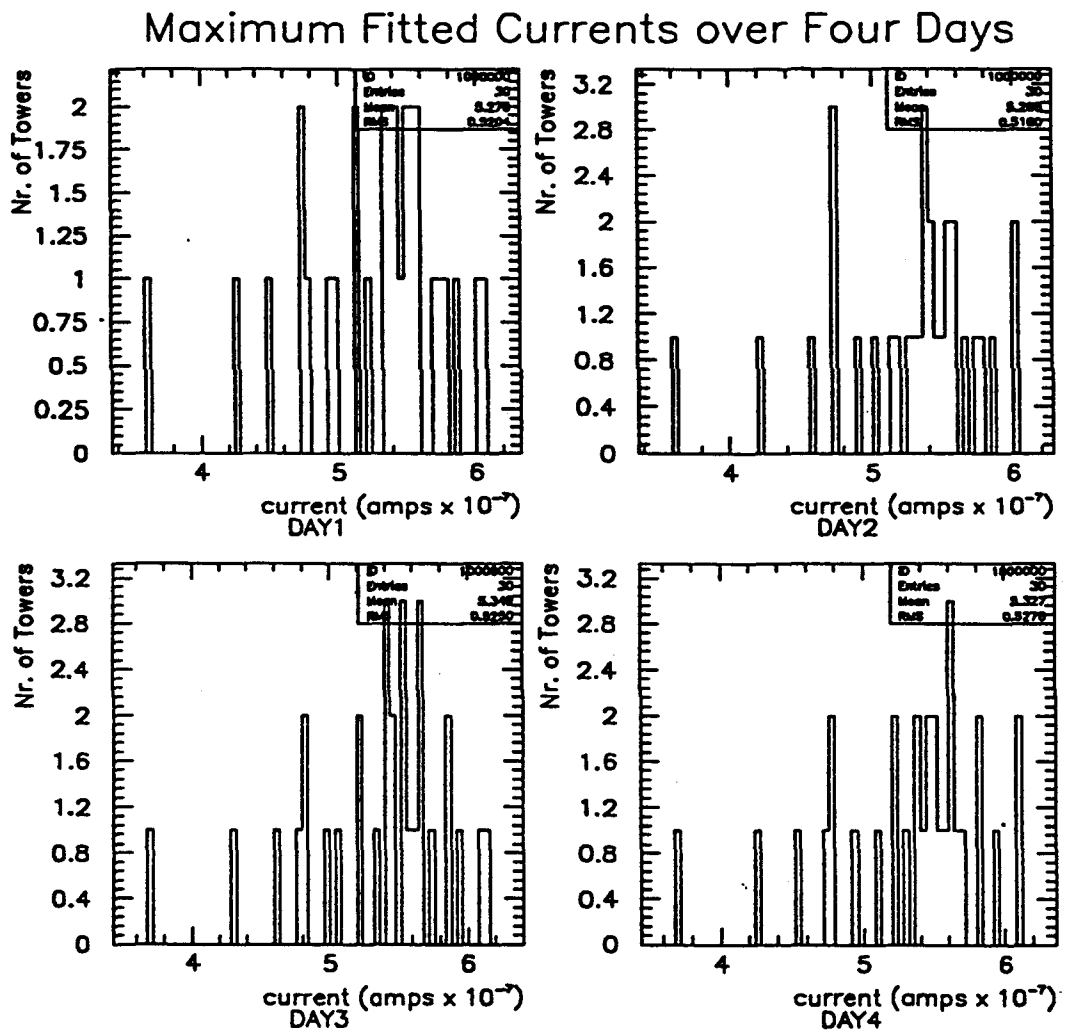

Fig.6-25. Maximum currents for 30 channels obtained from a fit to the measured currents for 4 days. a) Day 1, b) Day 2, c) Day 3 and d) Day 4. Two of the 32 channels are not included because for some of the running they had neutral density filters installed as part of a measurement of light yield

in 10,000 and the *rms* spread is about 0.0025. An investigation of the outlying points in Fig. 6-27 indicated that the "fit" values did not represent the maximum value well because the data points do not follow a smooth curve. Most likely this results from variations in the speed of the source drive motor or in the frequency with which the current is sampled.

In Figs. 6-28 and 6-29 we show the reproducibility of the data for "fitted" and "peak" currents over 96 hours compared to the value on the first day.

In Figs. 6-30 and 31 we show the reproducibility of the "fit" and "peak" values from day-to-day. As can be seen from these figures and Table 6-3, the values obtained from the

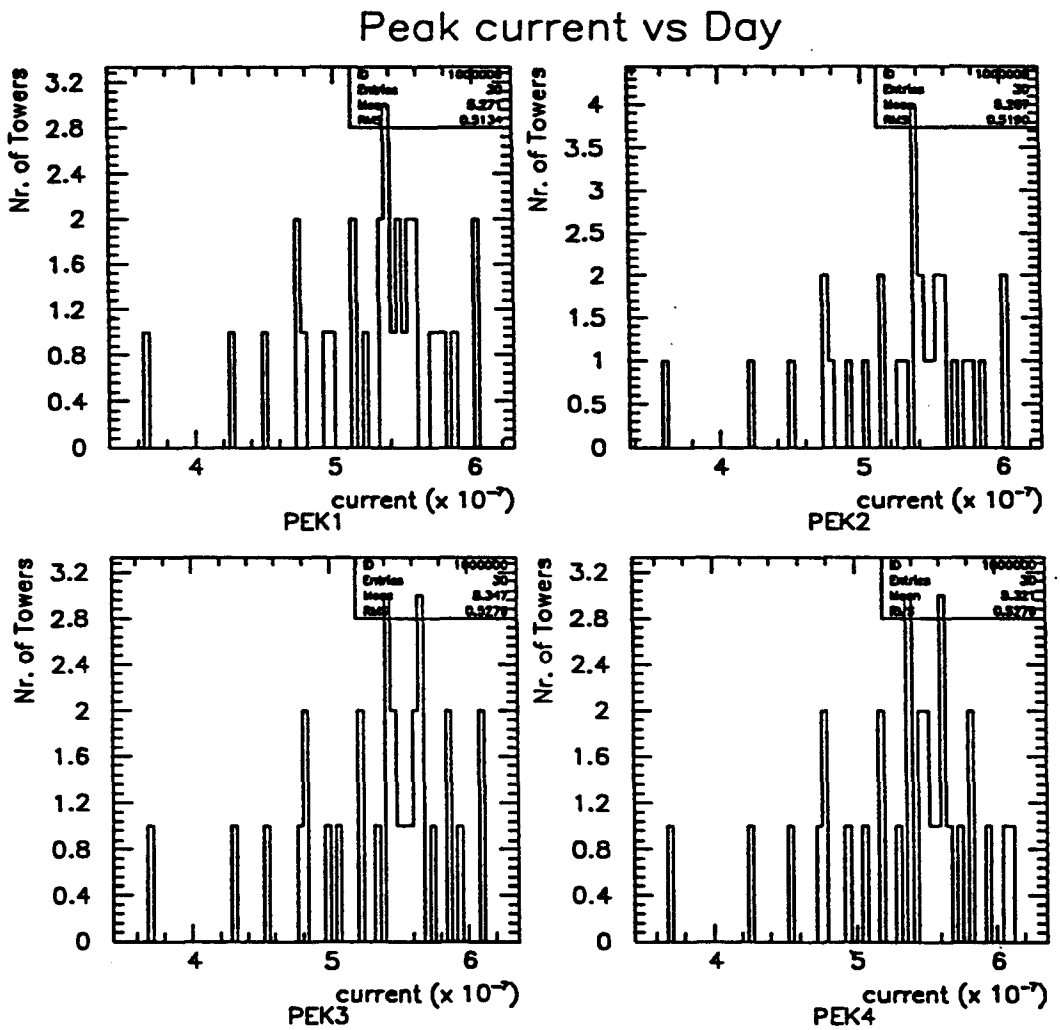

Fig.6-26. Peak measured currents for 30 channels on 4 consecutive days. a) Day 1, b) Day 2, c) Day 3 and d) Day 4. Two of the 32 channels are not included because for some of the running they had neutral density filters installed as part of a measurement of light yield

"fit" results are not as consistent. The "peak" values reproduce to typically 0.3% on a day to day basis and show a monotonic increase with time. Hence, in comparison with other measures of the calorimeter performance in what follows we will always us the "peak" values.

Finally, in Fig. 6-32 we plot the average response of the calorimeter over 96 hours separately for towers 1-8 and 9-16 corresponding to the two HV supplies. The data has been normalized to the values taken on the first day. As can be seen, the two sets of data track each other closely, and the maximum deviation is 1.5% from the measurements of the first day.

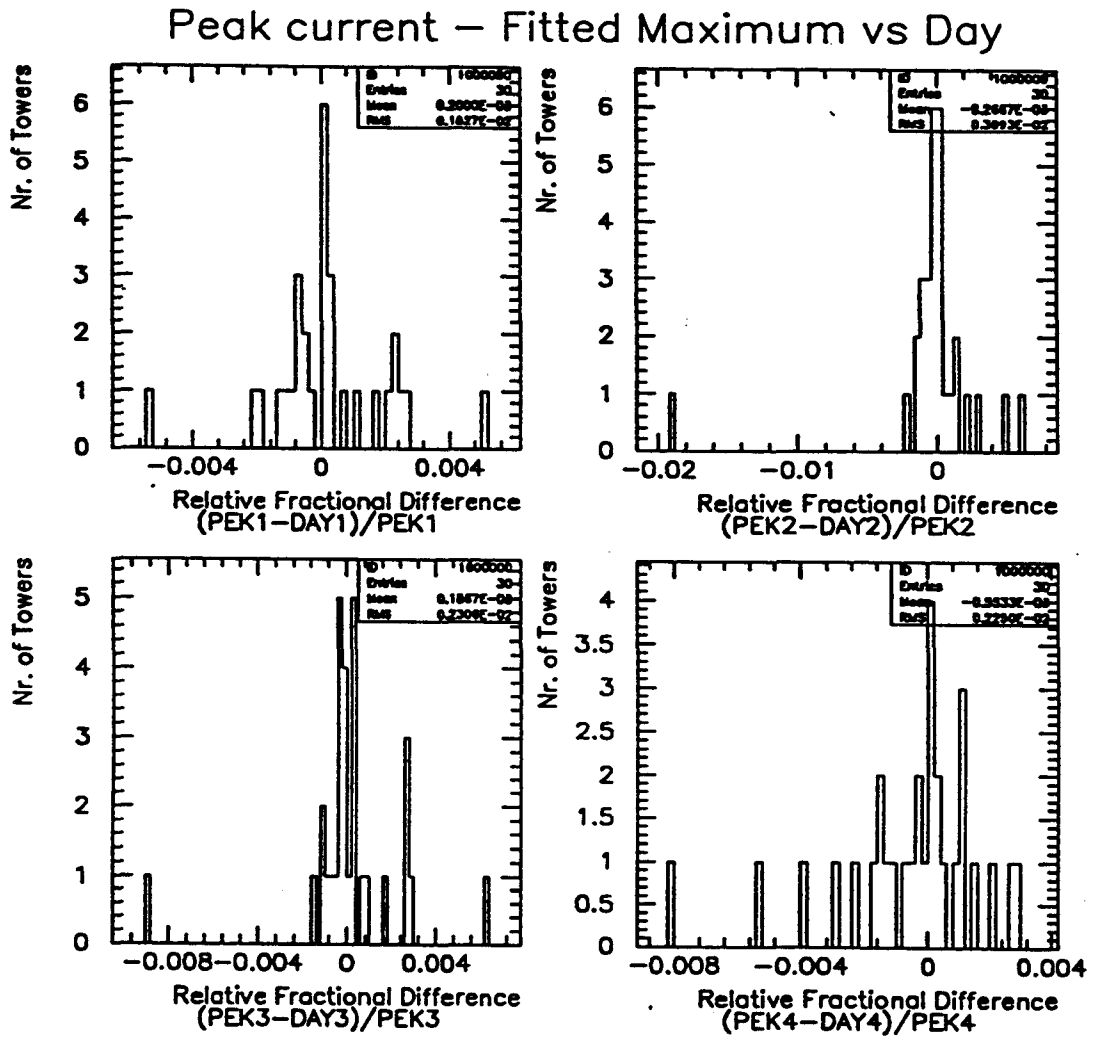

Fig.6-27. Relative difference between the maximum current obtained from a fit to the data versus the direct measurement of the current. a) on the first day, b) after 30 hours, c) after 72 hours and d) after 96 hours.

Comparison of Source Data with HV Monitor

Data from the HV monitor was available for only Day2 and Day3. A typical source data run is shown in Fig. 6-33. The currents listed in table 6-5 for each of the two phototubes in the high voltage monitor is the average of 400 measurements taken over a period of 100 *sec.* The HV monitor data is summarized in table 6-5 in comparison with changes in the average source data from the calorimeter. The results for the source tube data are drawn from Fig. 6-34, which shows the relative fractional change in the source currents on a day to day basis for the two power supplies.

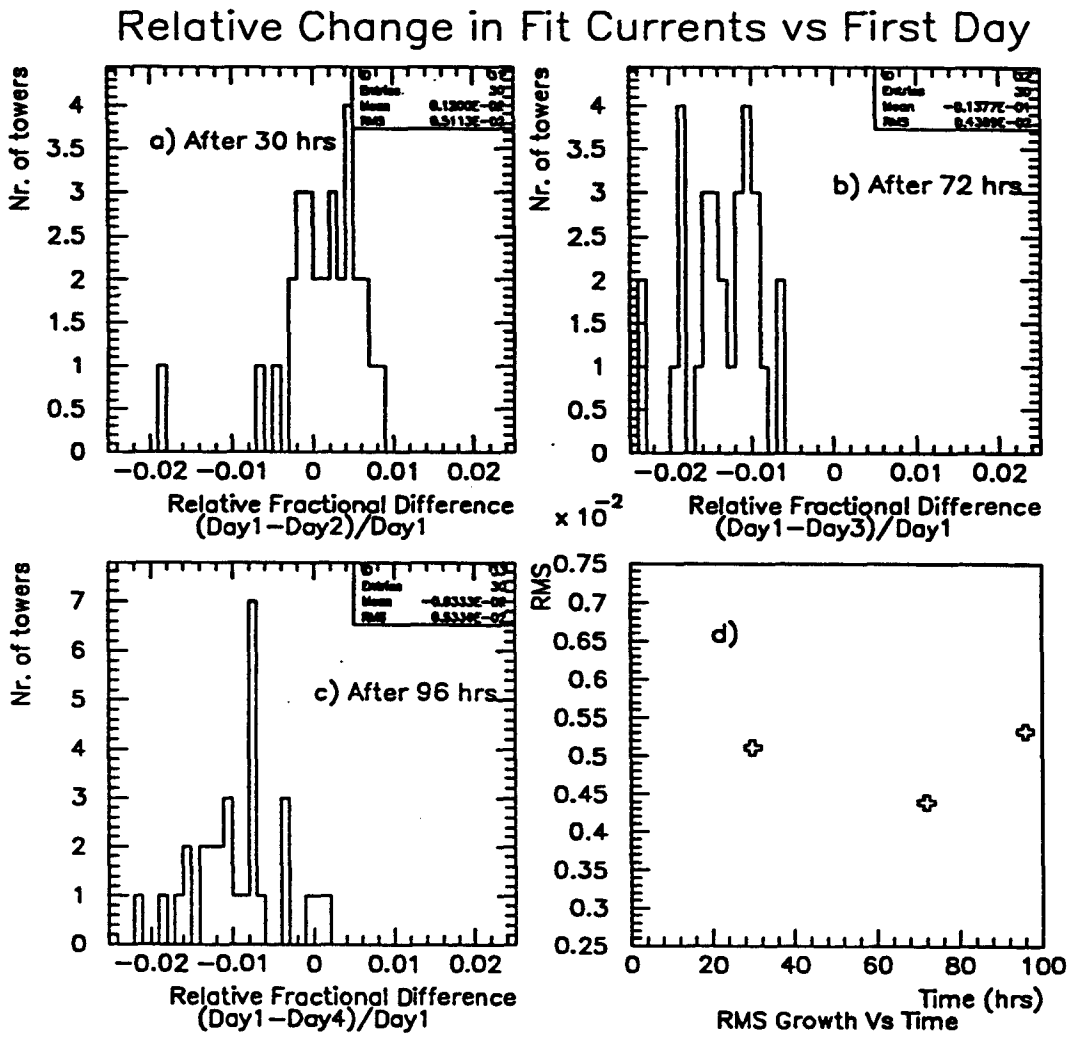

Fig.6-28. Reproducibility of the measured source currents vs time using the maximum value obtained from a fit to the data a) after 30 hours, b) after 72 hrs and c) after 96 hours. In d) we show the change in the *rms* width of a)-c) versus time.

As one can see by from the data in Table 6-5, the HV monitor system did not seem to track changes in the calorimeter performance. We cannot explain the discrepancy. However, in the future, it is clear that the HV monitor system should use more than a single phototube. As it stands, the HV monitor results presented in table 6-5 are based on multiple measurements of a single phototube, as compared to the source tube measurements that are the average of 16 tubes with currents 3 times larger.

Relative Brightness and Muon Calibration Data

During the construction of the calorimeter the relative light yield of every tile and fiber combination was measured. Tile/fiber combinations in the same layer were then sorted from

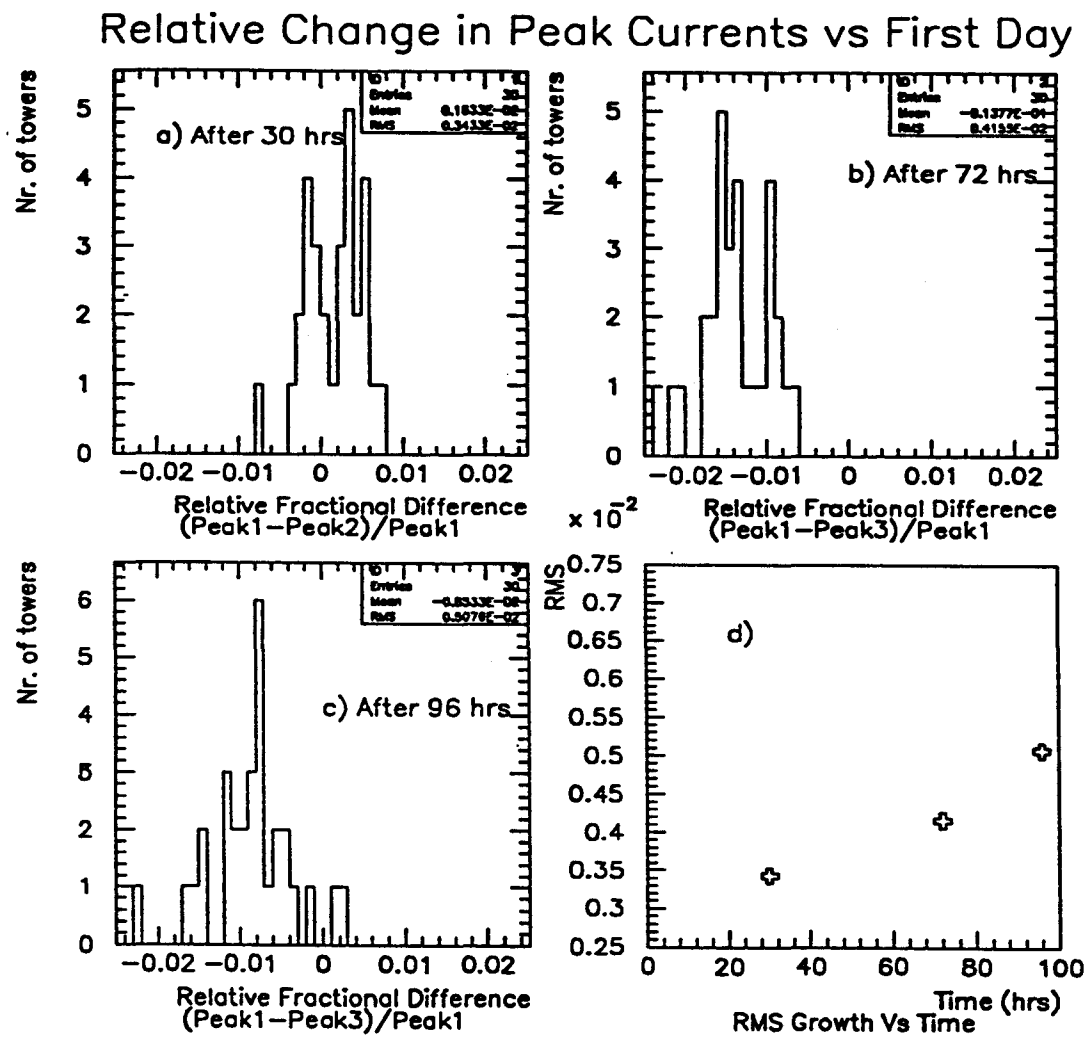

Fig.6-29. Reproducibility of the measured source currents vs time using the peak value a) after 30 hours, b) after 72 hrs and c) after 96 hours. In d) we show the change in the *rms* width of a)-c) versus time.

Table 6-3. Relative fractional difference between "fitted" and "peak" source data taken over 96 hours. Data from Day 1 has been arbitrarily normalized to 1.

Period	Difference in Time (hours)	"Fit" *rms*	"Peak" *rms*	
$(DAY1 - DAY2)/DAY1$	30	0.511	0.343	$\times 10^{-2}$
$(DAY1 - DAY3)/DAY1$	72	0.439	0.416	$\times 10^{-2}$
$(DAY1 - DAY4)/DAY1$	96	0.533	0.508	$\times 10^{-2}$

brightest to dimmest. Tile/fiber combinations with the same brightness rank were always put into the same tower. Additionally, the gain versus high voltage of each photomultiplier tube

Table 6-4. Relative fractional difference between "fitted" and "peak" source data on a day by day basis.

Period	Difference in Time (hours)	"Fit" *rms*	"Peak" *rms*	
$(DAY1 - DAY2)/DAY1$	30	0.511	0.343	$\times 10^{-2}$
$(DAY2 - DAY3)/DAY2$	42	0.261	0.200	$\times 10^{-2}$
$(DAY3 - DAY4)/DAY3$	24	0.418	0.301	$\times 10^{-2}$

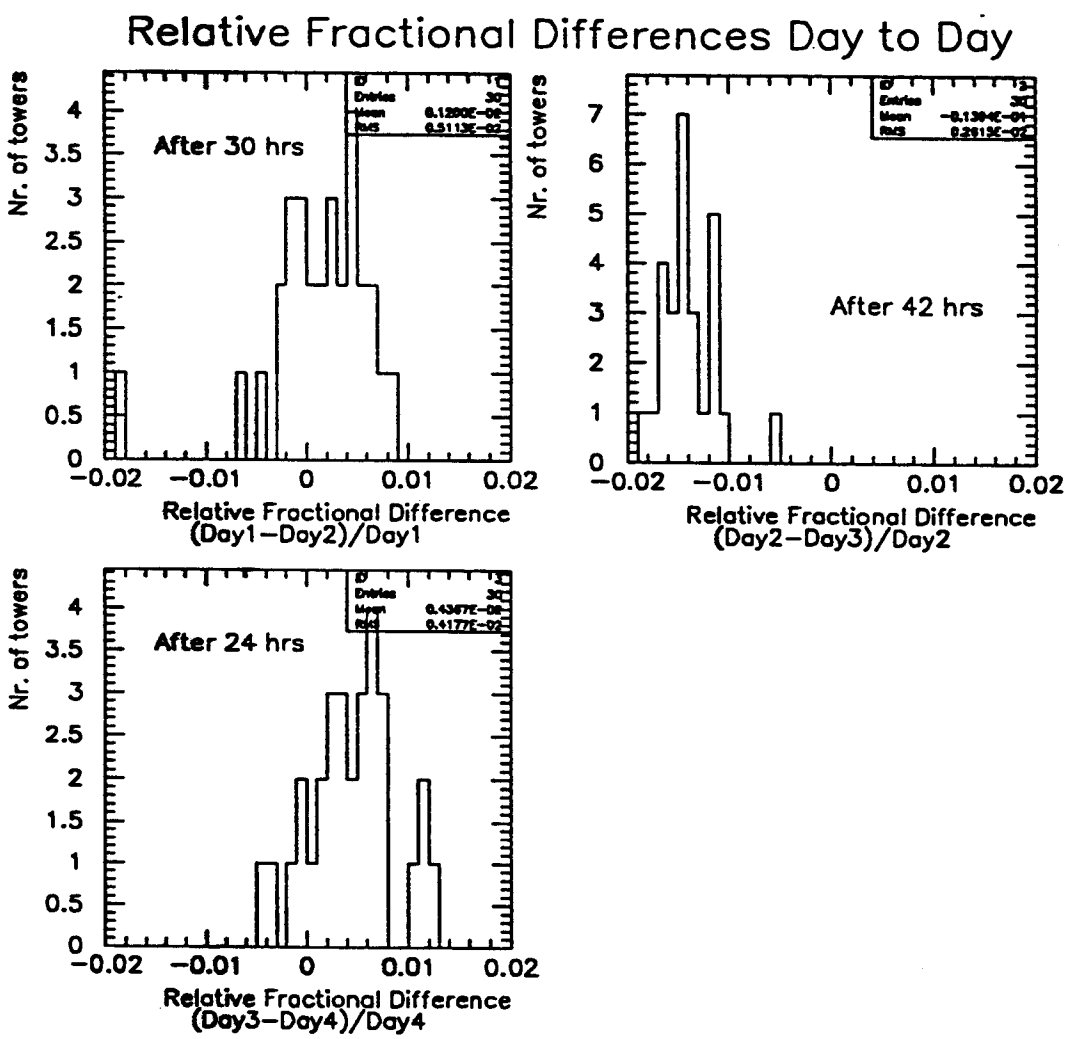

Fig.6-30. Relative fractional difference for the maximum current for a fit to the data for 3 time intervals a) day1-day2, b) day2-day3 and c) day3-day4.

was measured using the same source in conjunction with a standard tile/fiber combination. This allowed us to determine an "ideal" voltage for each phototube so that all phototubes

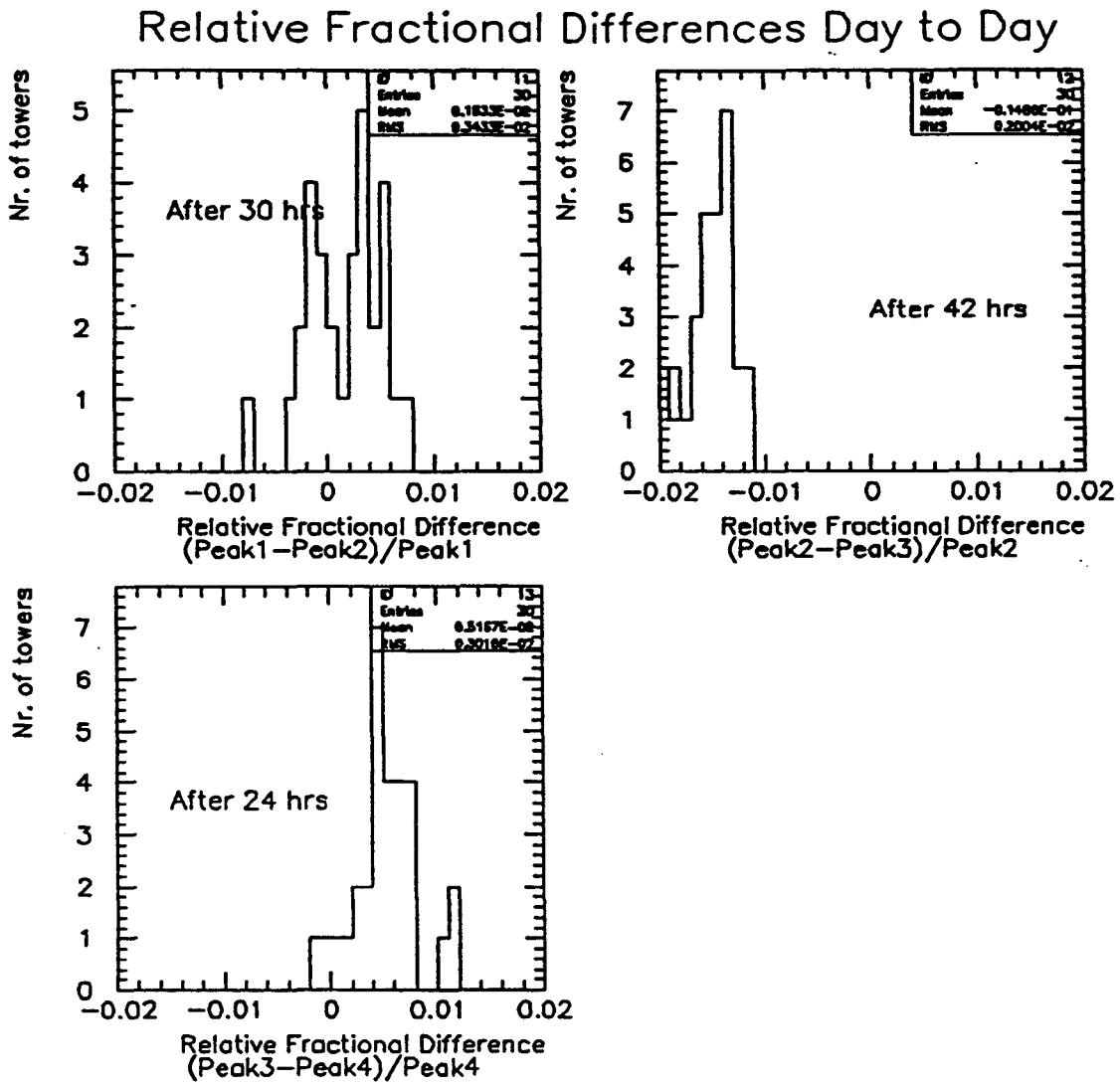

Fig.6-31. Relative fractional difference for the peak currents for 3 time intervals a) day1-day2, b) day2-day3 and c) day3-day4.

had the same relative gain. The typical variation in gain with high voltage was 0.5% per volt.

In Fig. 6-35 we display the correlation between the tower brightness and the source calibration. Our high voltage distribution system only allowed the high voltage to be adjusted to ±10 volts on any individual tube. In this plot the relative gain of each phototube has been adjusted to account for differences between the ideal voltage for the photomultiplier tube and the actual HV setting. As can be seen, there is a reasonable correlation between the tower brightness and the peak source currents. It is interesting to note that the EM1 towers are consistently brighter than the EM2 compartments. Since distinct tile/fiber combinations

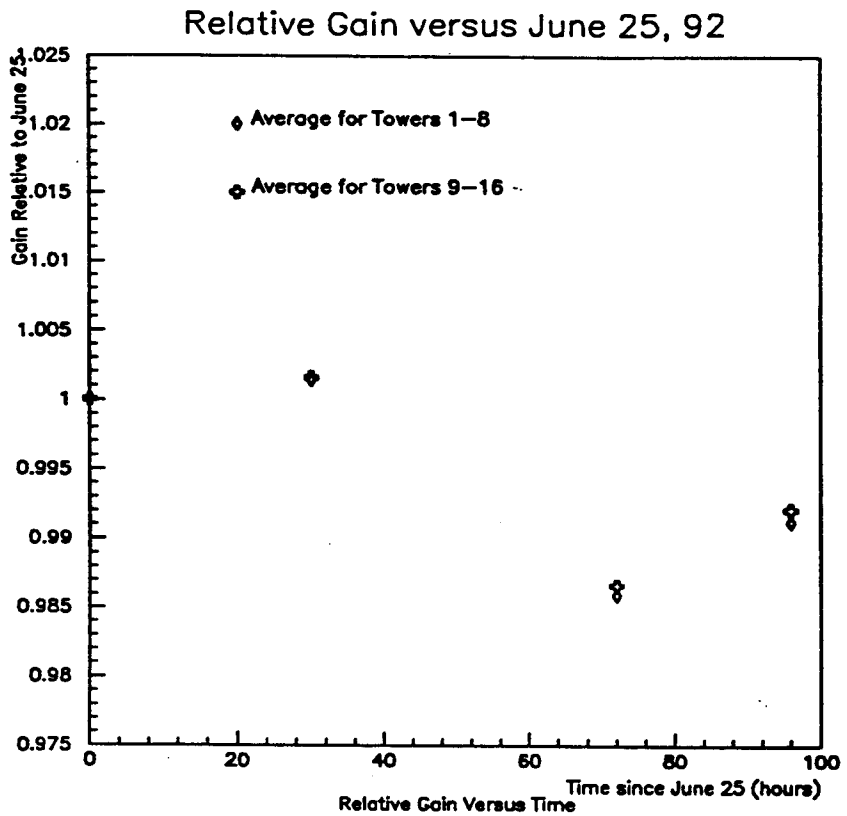

Fig.6-32. Average response of the calorimeter over time. The data has been normalized to the measurements of the first day.

are used in the EM1 versus the EM2 section of the calorimeter, there is no reason that the two compartments should have the same average response. Indeed, this result of the peak source measurements agrees with the gains derived from muon calibration in this respect.

Finally, in Fig. 6-36 we show the correlation between the muon calibration constants and the peak source currents. A reasonable correlation between the two signals are seen. We note that the muon signals were processed through an additional amplifier and the data in the plot has not been corrected for the gain of this amplifier. In Fig. 6-37 we show the deviation of the muon calibration as predicted from the source calibration numbers. The *rms* width of this distribution is about 7%. The DAQ system for the source current measurements was independent of the DAQ system for collecting beam data. Since we did not measure the relative gain between the two systems, we are unable to explain the difference.

Source Calibration Summary

This section has examined the source data taken with the LBL calorimeter test station module. The maximum current obtained from a fit of a parabola to the raw source current

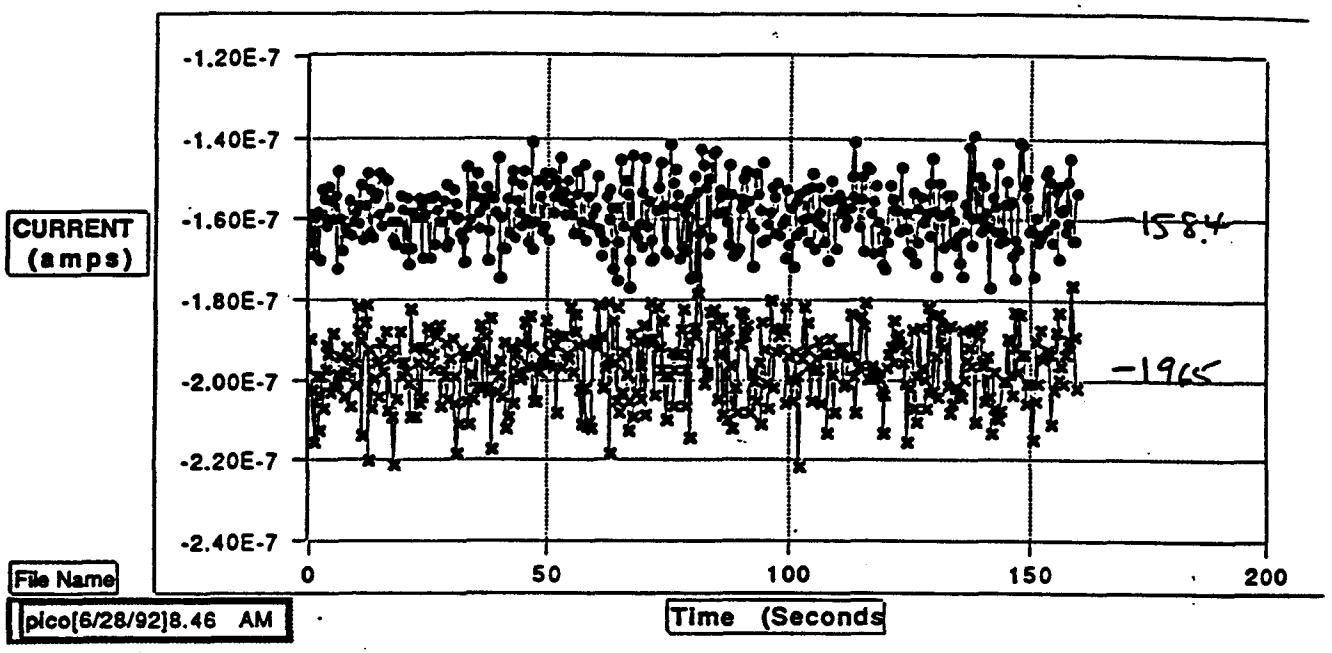

Fig.6-33. An example of the data used to monitor the high voltage. The current from each of two tubes was measured 400 times over 100 seconds to compute the average current in the monitor tubes. One of the two tubes was connected to the same HV supply as used to power towers 1-8, the other channel was connected to the supply for towers 9-16.

data provides less reliable gain information than the peak measured current used directly. Readback of the source location may improve the reliability of the "fit" values.

The peak source current values reproduce to 0.3% over 24 hours. The repeatability of the peak source current measurements degrades versus time, from 0.3% *rms* to 0.5% *rms* after 96 hours. The maximum drift of the system over 96 hours was 1.5%. A high voltage monitoring system, consisting of one photomultiplier tube per HV supply viewing a common Am^{247} source did not reproduce this gain shift. This may be an indication that the HV monitor should measure the response of several tubes, rather than depending on the characteristics of a single photomultiplier tube.

There is a reasonable correlation between the peak source currents and the tower brightness rank implemented during construction. The *rms* difference between the muon calibration constants and their values as predicted from the source data is 7%, not corrected for electronics gain. Since we did not measure the gain of all of the electronics components in the DAQ system, we are unable to explain the difference.

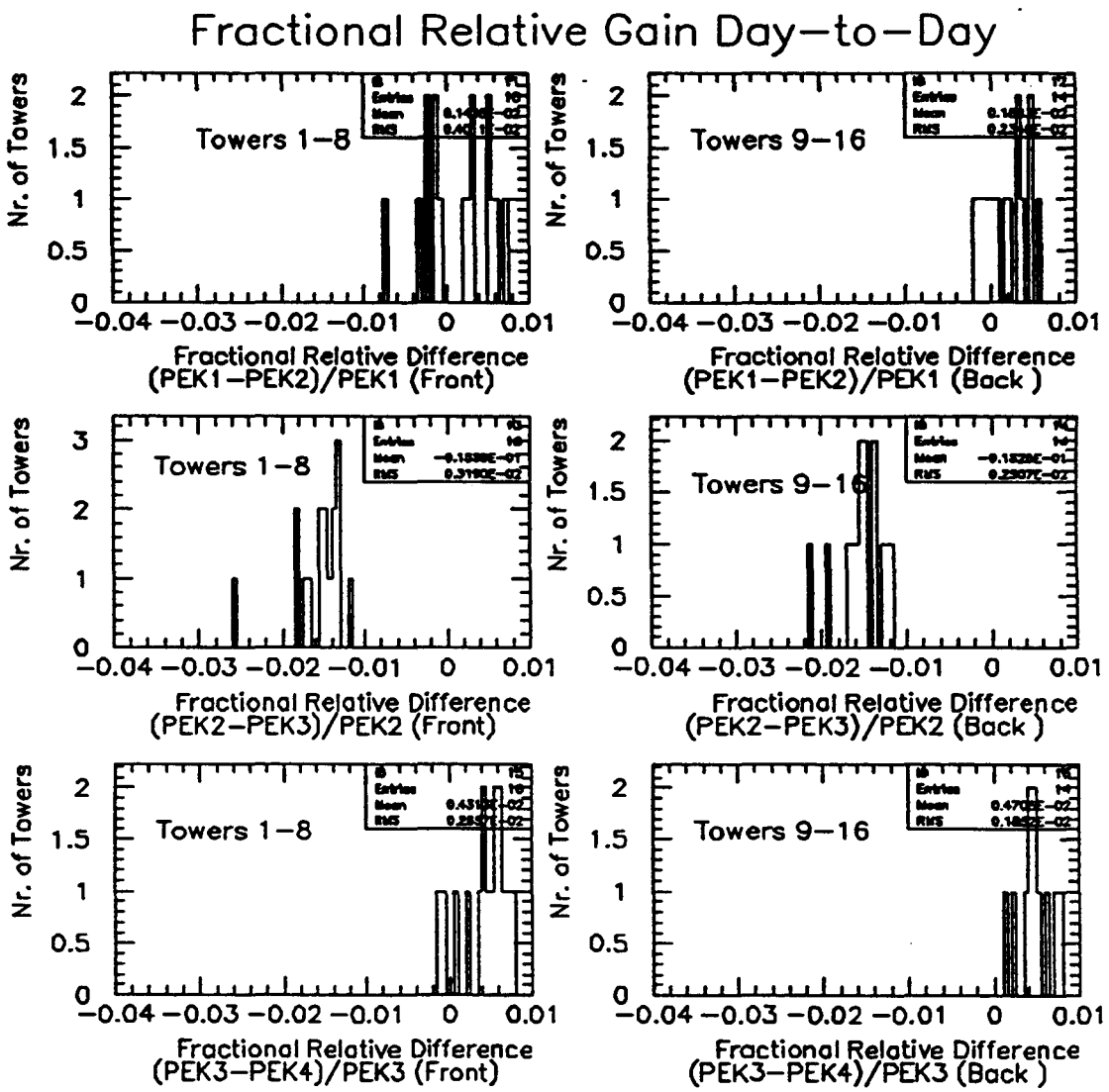

Fig.6-34. Average response of the towers in the calorimeter for the two HV supplies. One supply controlled towers 1-8, and a second supply provided high voltage to towers 9-16. The current from both photomultipliers tubes corresponding to the EM1 and EM2 compartments of tower 11 have been disregarded in this latter sum as part of the time they were used with neutral density filters to measure the photoelectron yield. The six plots record the change in response of the calorimeter during 3 one day intervals, separately for each of the two HV power supplies.

6.5. Electron Resolution

Electron data was taken for momenta of 1, 2, 5, 10 and 15 GeV/c with the beam centered on towers 10 and 11. Additional runs at 10 GeV/c from towers 6, 7, 10 and 11 were also used. Data from other towers were not used because it is not possible to form a nine-tower (three by three) sum around those towers. The purity of the electron trigger selection is illustrated in Fig. 6-38, which shows the observed response (after pedestal subtraction) for each energy.

Table 6-5. Currents in HV monitor photomultiplier tubes vs time as compared to the average drift of the source tube measurements of the calorimeter.

High Voltage Monitor Currents						
	Towers 1-8			Towers 9-16		
Day	Current (*namp*)	Error (*namp*)	1- (Day3/Day2)	Current (*namp*)	Error (*namp*)	1-(Day3/Day2)
Day2	194.7	0.4		158.0	0.4	-
Day3	196.5	0.4	-0.009 ± 0.003	158.4	0.4	-0.003 ± 0.003
Relative Average Changes in "Peak" Source Currents						
			-0.016 ± 0.001			-0.015 ± 0.001

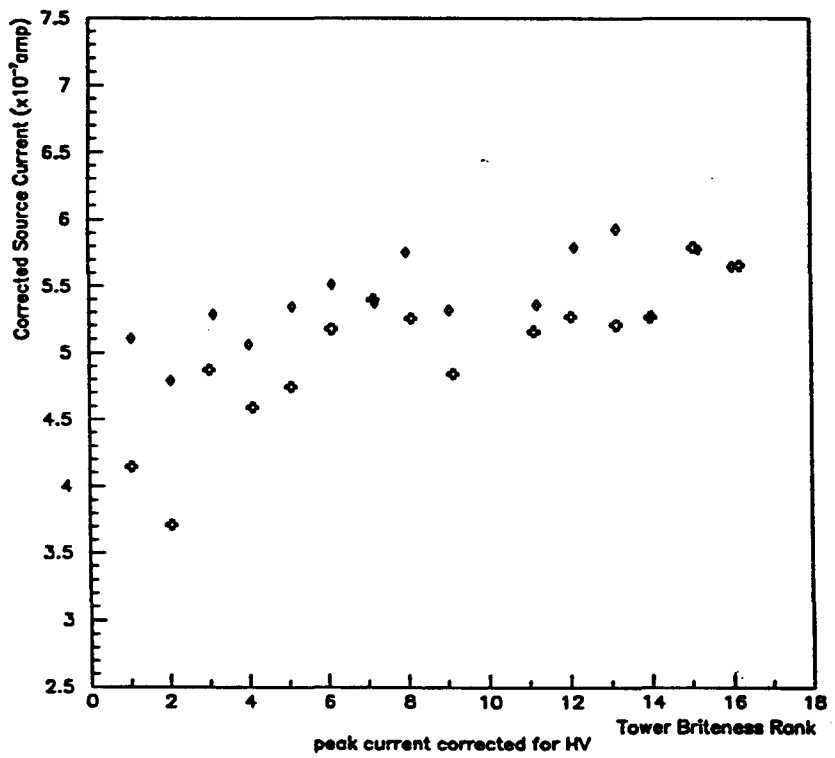

Fig.6-35. Tower brightness rank versus peak source current for each tower. The tower with the brightest tile/fiber combinations has rank 16. The peak currents have been corrected for high voltage (see text).

The data are analysed using nine-tower sums. The beam size at the calorimeter was large–± 3 *cm* in x, ± 1.1 *cm* in y–so single tower quantities are not as well defined. Table 6-6 summaries the observed responses. The values are based on Gaussian fits, and are averages over all runs at each energy. The uncertainties in the mean do not reflect the impact of pedestal drifts of up to tens of counts observed in some runs. In all cases, the fits are very good and the results are insensitive (within the given uncertainties) to reasonable variations in binning and in the fit region. The response is linear to within 1% for $E \geq 5$ GeV/c

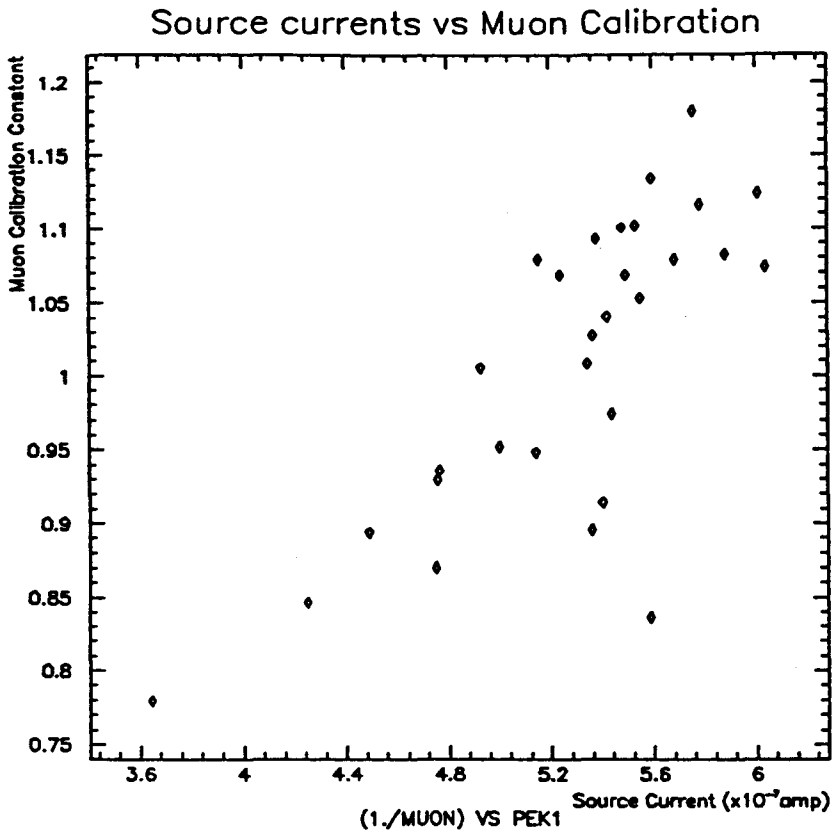

Fig.6-36. Muon Calibration constants vs peak source current for each tower.

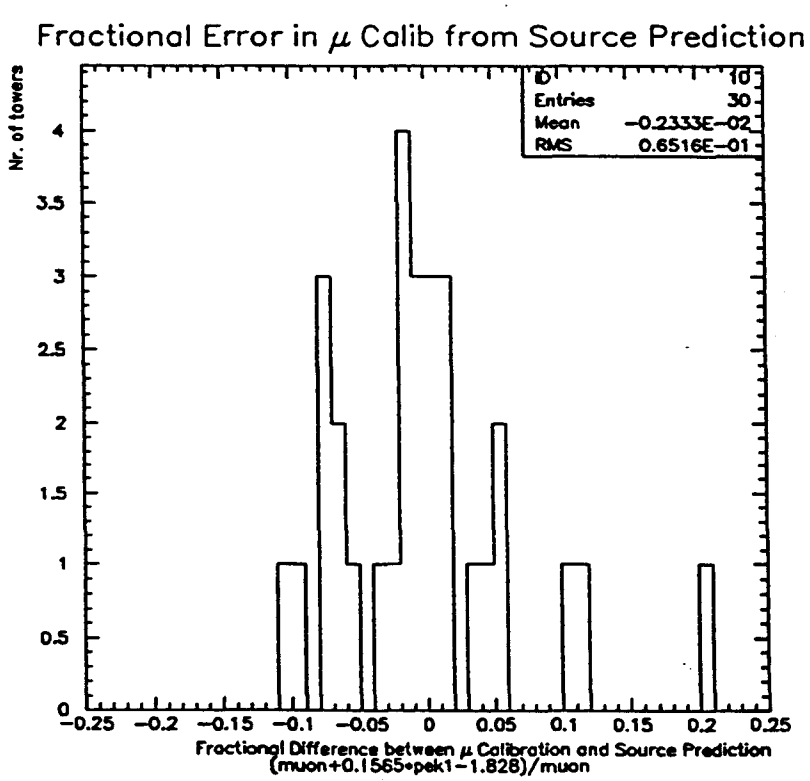

Fig.6-37. Deviation of the muon calibration data from the value predicted by source data. The *rms* of the distribution is about 6.5%.

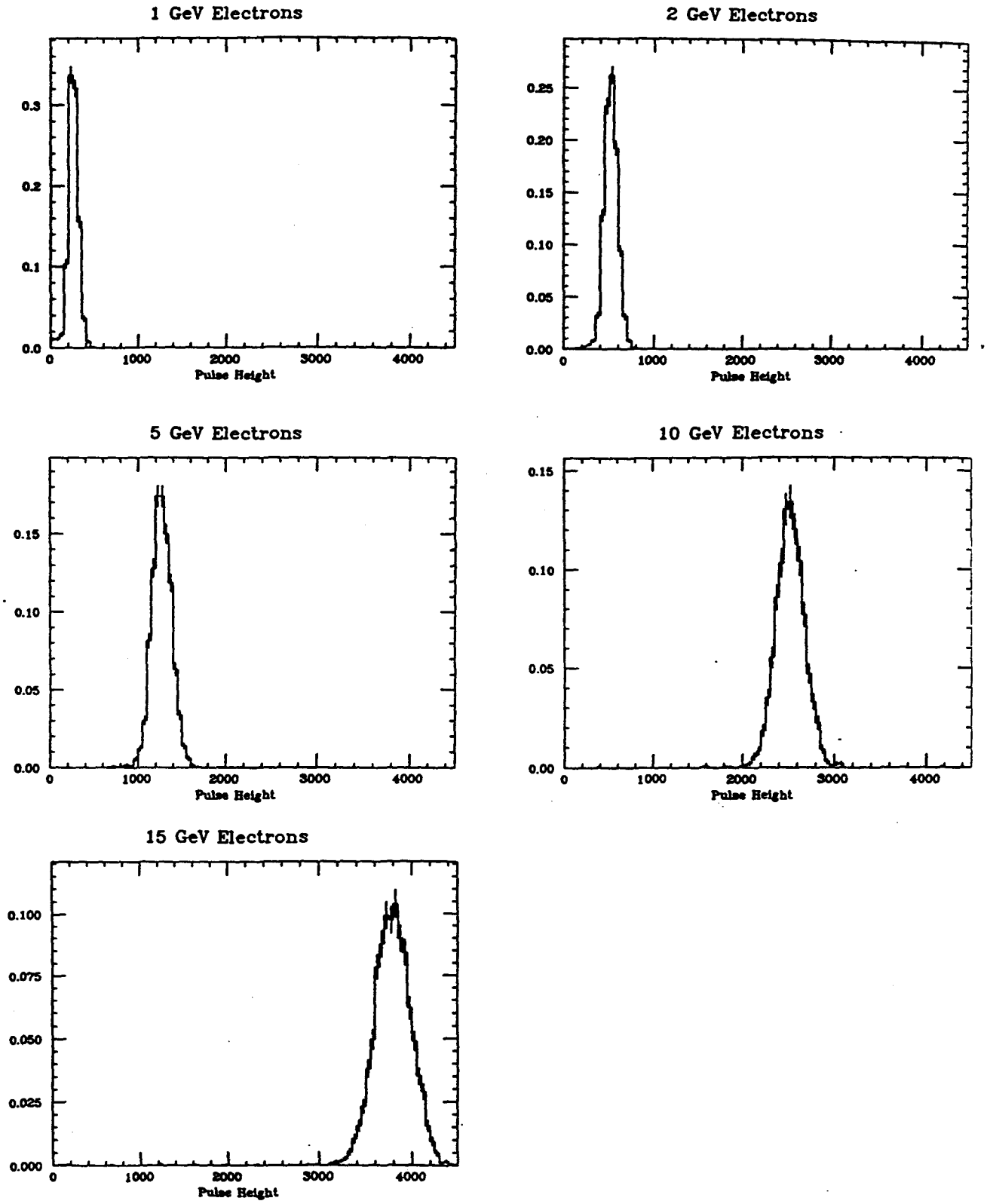

Fig.6-38. Observed pulse heights (after pedestal subtraction) for 1, 2, 5, 10 and 15 GeV/c electron triggers. (Nine tower sum).

(Fig. 6-39). The true beam momentum is not known at lower momentum to an accuracy better than the apparent deviations from linearity.

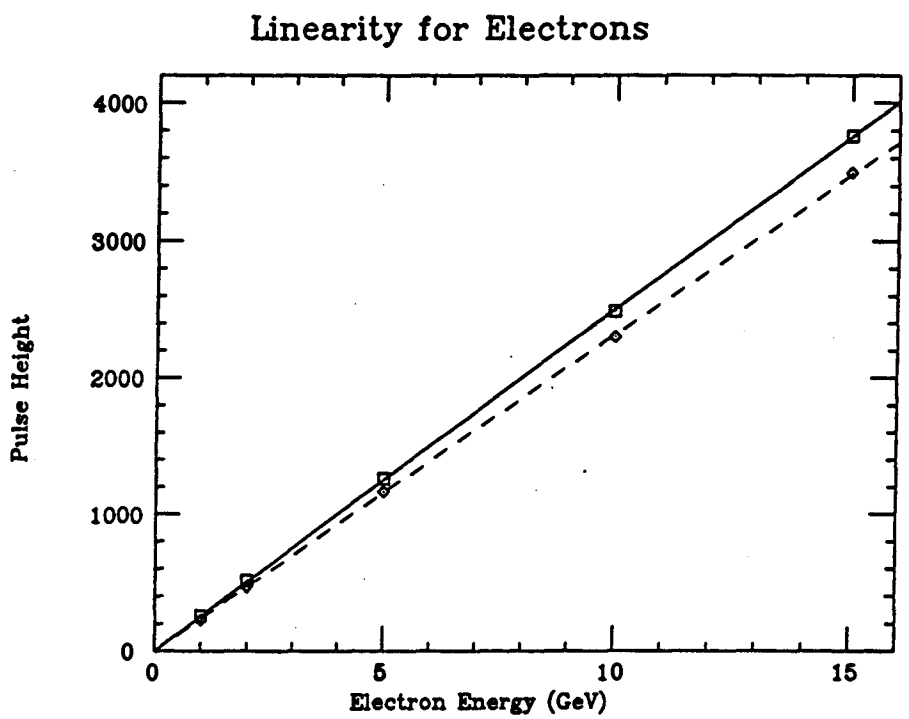

Fig.6-39. Average pulse height vs electron energy for a nine tower (solid) and one tower (dashed) sum.

Table 6-6. Pulse height and resolution for electrons measured with the calorimeter test module in the BNL test beam. A 3 × 3 array of towers is used. p is the nominal beam momentum, which had a momentum spread of $\Delta_p/p = 0.01$. α is defined to be σ/E minus Δ_p/p in quadrature.

p (GeV/c)	mean (counts)	mean/p	rms (counts)	rms/mean	α	$\alpha \cdot \sqrt{E}$
1	253 ± 1	253.0 ± 1.0	49.3 ± 0.8	0.1949 ± 0.0032	0.1946	0.1946 ± 0.0032
2	511 ± 1	255.5 ± 0.5	68.5 ± 0.8	0.1341 ± 0.0016	0.1337	0.1891 ± 0.0023
5	1258 ± 2	251.6 ± 0.4	105.6 ± 1.3	0.0839 ± 0.0010	0.0833	0.1863 ± 0.0022
10	2489 ± 2	248.9 ± 0.2	151.3 ± 1.3	0.0608 ± 0.0005	0.0600	0.1897 ± 0.0023
15	3761 ± 3	250.7 ± 0.2	190.9 ± 2.3	0.0508 ± 0.0006	0.0498	0.1929 ± 0.0023

The energies tested are too low to be sensitive to the constant term expected for a single beam location. Figure 6-40 is a plot of α^2 *vs* $1/E$ ($\alpha = \sigma_E/E$).

For resolution of the form $\sigma_E/E = a/\sqrt{E} \oplus b$, this plot should be a linear relationship with slope a^2 and intercept b^2. The data are consistent with no constant term; the 90%

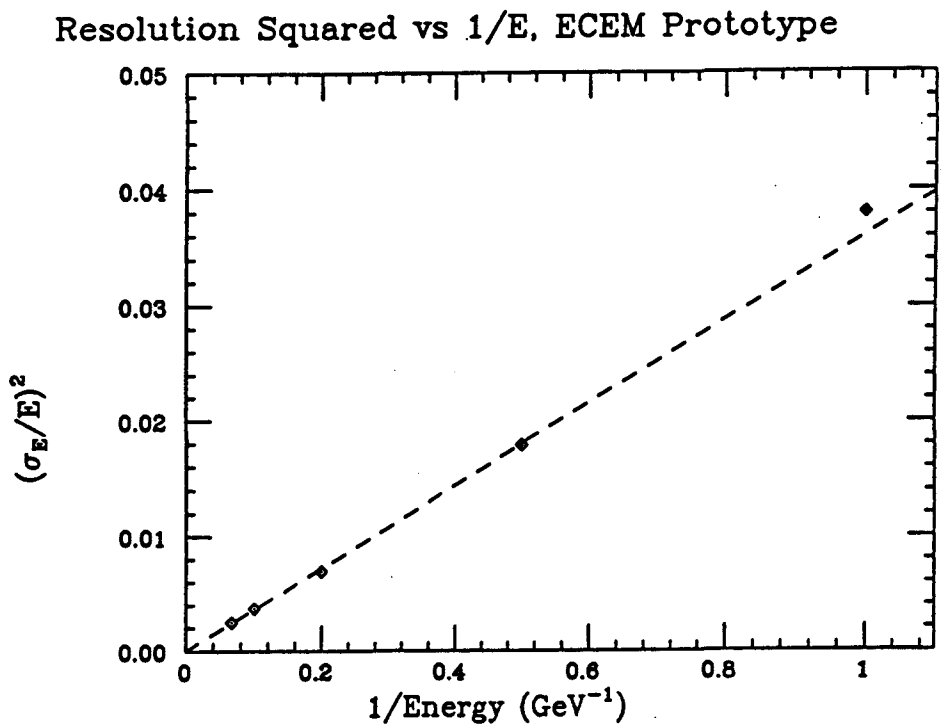

Fig.6-40. Resolution squared as a function of (electron energy)$^{-1}$, for a nine tower sum.

confidence limit is $b < 1.4\%$. Assuming $b = 0$, the resolution is:

$$\sigma_E/E = (0.190 \pm 0.001)/\sqrt{E}.$$

The EGS prediction for the energy deposited in the scintillator and for the energy resolution is given in Table 6-7. The calculation uses cutoffs of 1.0 MeV (*ecut*) and 0.01 MeV (*pcut*). Varying *ecut* from 0.53 to 1.0 MeV does not change the resolution at 10 GeV/c (although it does change the required CPU time). The sampling fraction, independent of energy, is 4.7%. The light yield contribution to the resolution assumes 78 ± 10 photoelectrons per GeV. Fig. 6-41 plots the nine-tower data resolutions and the EGS prediction as a function of energy, with and without the photostatistics contribution. The predicted EGS resolution with 78 pe/GeV is slightly worse than the actual value; $\sigma_E/E = (0.199 \pm 0.004)/\sqrt{E}$. The difference between data and EGS would imply a light yield of 107 pe/GeV.

6.5.1. Lateral Leakage

The tower in which the beam was centered contained, on average, 93% of the energy observed in the nine-tower sum. This fraction represents an average over the large beam spot.

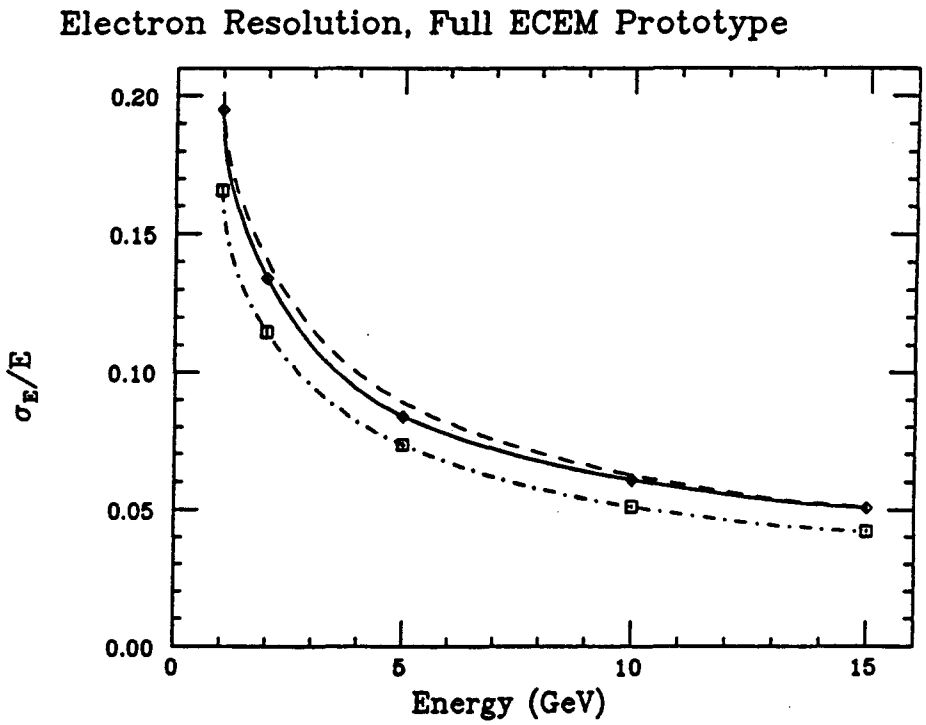

Fig.6-41. Resolution as a function of electron data. Diamonds (solid) are data, dotdash is EGS for infinite photostatistics, and dashed is EGS for 78 pe/GeV.

Table 6-7. Summary of EGS calculation of electron response of full calorimeter test module. Light yield (N_{pe}) is based on measured value of 78 pe per GeV. α is defined to be $\sigma/E \oplus 1/\sqrt{N_{pe}}$.

E (GeV/c)	Mean MeV in scint	Mean/E	*rms* (MeV)	σ/mean	N_{pe}	α	$\alpha \cdot \sqrt{E}$
1	47.0 ± 0.1	47.0 ± 0.1	7.80 ± 0.09	0.1658 ± 0.0019	78	0.2008	0.2008
2	94.2 ± 0.2	47.1 ± 0.1	10.81 ± 0.12	0.1147 ± 0.0013	156	0.1399	0.1978
5	236.0 ± 0.3	47.2 ± 0.1	17.3 ± 0.2	0.0733 ± 0.0009	390	0.0891	0.1992
10	471.5 ± 0.4	47.2 ± 0.1	24.1 ± 0.3	0.0512 ± 0.0005	780	0.0625	0.1976
15	707.2 ± 0.6	47.1 ± 0.1	29.9 ± 0.4	0.0422 ± 0.0006	1170	0.0513	0.1988

The 7% lateral leakage does not affect the linearity, as is shown by the dashed line in Fig. 6-39. The single tower energy resolution is somewhat worse, but is still consistent with no constant term: $b < 1.1\%$ (90% CL). Assuming $b = 0$, the resolution is $\sigma_E/E = (0.198 \pm 0.001)/\sqrt{E}$ for a single tower. These data are consistent with an interpretation that lateral leakage represents a decrease in sampling fraction only. This is in contrast to longitudinal leakage, where 7% leakage would induce a constant term of 3% [6-3].

An EGS simulation with a similar distribution of impact points predicts that the one-tower to nine-tower ratio is 0.933 at 10 GeV/c, in reasonable agreement with the observed

value of 0.926. The calculated single-tower resolution is $\sigma_E/E = 0.0524 \pm 0.0011$ for infinite photostatistics, or 0.0642 ± 0.0016 for 78 photoelectrons per GeV. This is slightly worse than the observed value of 0.0626 ± 0.0006.

6.5.2. e/μ

One of the properties needed to understand the compensation response of the full calorimeter is the e/μ ratio for the EM compartment. We define the ratio of the number of photoelectrons observed per GeV of energy deposited in the calorimeter by electromagnetic showers to that observed for a minimum-ionizing particle as e/μ. Unfortunately, this is not a precisely defined quantity, since experimentally available particles—such as 10 GeV/c muons—are not ideal minimum ionizing particles. Nevertheless, the results are summarized in Table 6-8.

Table 6-8. Calculation of e/mu using 10 GeV/c electrons and either muons or mips. N is the observed peak pulse height; E_{cal} is the energy deposited in the calorimeter; α is the number of ADC Channels per GeV in the calorimeter; s is the fraction of energy deposited in the scintillator (or lost by the mip in the scintillator, in the last column); c is the number of ADC counts per GeV deposited in the scintillator; and e/μ is the ratio of α_e/α_μ or s_e/s_{mip}.

Quantity	10 GeV e	10 GeV μ	mip
N (ADC channels)	2502 ± 2 data	88.9 ± 0.7 data	–
E_{cal} (GeV)	10 data	0.234 ± 0.001 GEANT	0.212 calculation
$\alpha = N/E$ (counts/GeV)	250.2 ± 0.2	380 ± 3	–
s	$0.0470 \pm .0001$ EGS	$0.0710 \pm .0004$ GEANT	0.0834 calculation
$c = \alpha/s$ (counts/GeV)	5320 ± 10	5350 ± 50	–
e/μ	–	0.658 ± 0.005	0.564

The second and third columns relate to test-beam observations and EGS or GEANT calculations for ten GeV/c electrons and muons. The last column applies to "mips", where the total energy deposited and the fraction in the scintillator are calculated using the $dE/dx[min]$ values from ref. [6-4]. It should be noted, however, that these dE/dx values refer to energy lost by the mip while it is in the material, not the energy deposited in the material: some of

the energy lost in the scintillator will actually be deposited in the absorber. These effects are included in GEANT, so to the extent that 10 GeV/c muons are mips, the e/μ value of 0.658 ± 0.005 is more believable than that in the last column.

The quantity c in Table 6-8 is the number of ADC counts observed per GeV of energy deposited in the scintillator (as opposed to α, which is the ADC counts per GeV in the *calorimeter*). The fact that the values for c are consistent for electrons and muons indicates that saturation in the scintillator is negligible for electromagnetic showers. It is expected that c would be smaller for hadronic showers.

6.6. Crack and Spoke Scans

There are four different types of cracks between towers in the module: the three horizontal gaps are 0.2, 0.4 and 0.6 *mm* between the scintillator (including paint), while the vertical cracks are all 0.2 *mm*. The tiles are not beveled, so the vertical crack is slightly "stair-stepped" (by the thickness of the tile), while the horizontal cracks are purely projective. Unfortunately, due to the problems with the tracker, only the 0.2 and 0.6 *mm* horizontal cracks have enough data to be studied (and the 0.2 *mm* case is marginal). Figure 6-42 shows the full calorimeter response as a function of the impact point of the ten GeV/c electrons for the two cases. The 0.2 *mm* gap is not visible, while the 0.6 *mm* gap results in a 2% dip in response at the crack, and some degradation of response over a distance of ± 8 *mm*.

If uncorrected, this dip would result in a constant term of approximately 0.3% (ignoring the other observed nonuniformities). However, this variation is probably correctable even with the position determined from the energy splitting between the towers.

The spoke location in a tower is shown in Fig. 6-43. In tower-number units, it is at shower-maximum for $y = 0.46$ and $0.26 < x < 0.41$. Figure 6-44 shows the calorimeter response as a function of vertical position for 10 GeV/c electrons in this horizontal region. No dip in response is visible at the spoke location.

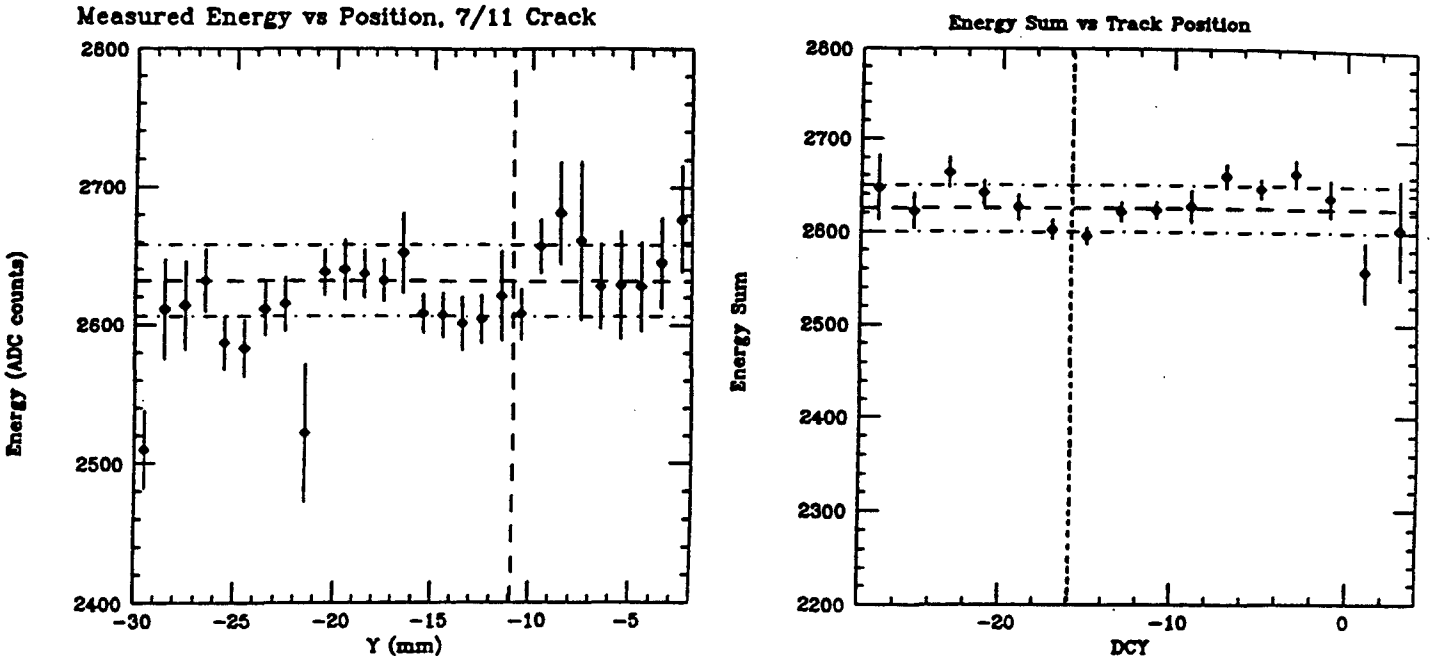

Fig.6-42 Nine tower signal for 10 GeV/c electrons scanned across a (a) 0.2 *mm* and a (b) 0.6 *mm* crack between active scintillator. (Crack is filled with paint and plastic). The dashed line indicates the location of the crack.

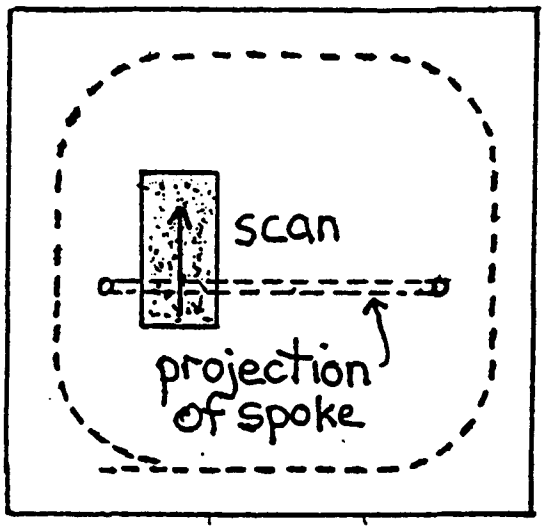

Fig.6-43 Location of spoke in tower. The spoke hole is at the left-most point in the first tile in depth, and progresses to the right-most point in the last tile. The arrow and the speckled region indicate the region used in the scan across the spoke.

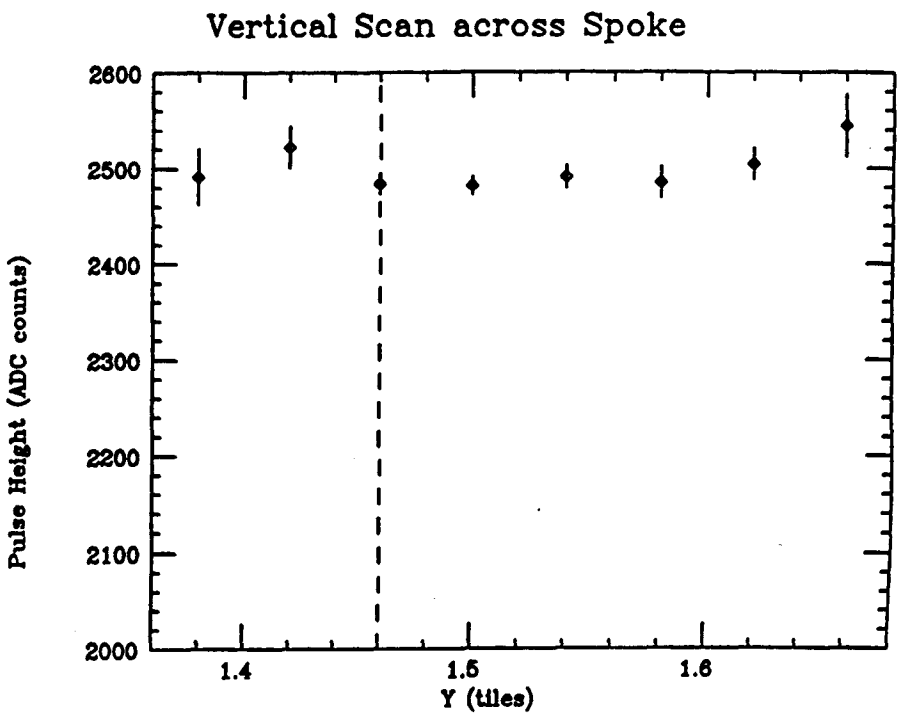

Fig.6-44 Observed signal for 10 GeV/c electrons as a function of vertical position. The spoke is at shower maximum at the dashed line.

6.7. Test Beam References

[6-1] The source driver, source and controller were supplied by V. Barnes, Purdue University.

[6-2] LABVIEW is a product of National Instruments, Inc.

[6-3] C. Hearty, "Effect of Electromagnetic Calorimeter Thickness on Resolution", SDC–91–00084, Sept. 1991.

[6-4] Particle Data Group, Review of Particle Properties, PRD, Vol. 45, Nr.11, Part II (1992).

7. Cost estimate

The following steps have been / are being taken to arrive at a comprehensive cost estimate for the monolithic ECEM:

- The baseline ECEM cost has been extracted from the existing cost estimate [7-1]. This required apportioning of costs from several areas in the WBS, since the ECEM was not conceived of as a separate entity at the time of the baseline cost exercise. The resulting baseline cost attributable to the ECEM is $12.3 M, with a net contingency of 31%, yielding a final cost estimate of $16.1M.
- A new WBS section (2.2.5) has been tentatively allocated for a separate, monolithic ECEM and a detailed WBS down to the seventh level has been written in a manner consistent with the balance of the calorimeter WBS
- A new "bottoms up" cost estimate using the WBS for the new monolithic ECEM is now being prepared. It will be based on budgetary quotes from several components vendors combined with new manpower estimates. However, since the purpose of this estimate is to allow an "apples and apples" comparison of the cost of the new mechanical design with the baseline cost, estimates for generic, common items such as the scintillator tiles and fibers have been copied directly from the baseline estimate.

8. Summary, Remaining R&D and Schedule

We have presented a novel design for an endcap calorimeter for SDC. The design utilizes thin, non-projective bicycle spokes to support the absorber plates, and maximizes acceptance by removing η bulkheads and ϕ cracks between modules. Test beam studies of the 4x4 calorimeter test station module have shown that:

- The supports are invisible in 10 GeV/c electron showers.
- The calorimeter is linear over the measured energy range to 1%.
- The measured energy resolution is $19\%/\sqrt{E}$ and consistent with no constant term; the constant term is less than 1.4% at the 90% confidence limit.
- The linearity and resolution are consistent with the expectations derived from Monte Carlo simulations.

These tests also show that the transverse uniformity of the scintillator tiles is dominated by the optical response of tile/fiber combinations and the inter-tile gaps of 0.65 mm do not introduce any significant non-uniformity (less than 2% over 5 mm).

Hiding the mechanical structure behind the barrel EM calorimeter maintains uniform electron acceptance from $0 <| \eta |\approx 3.0$ The endcap is designed to overlap approximately 2 cm with the barrel EM, as viewed from the interaction region. Minimal material is placed at the $| \eta |= 3.0$ boundary so the missing E_t can be accurately measured both in the endcap and forward calorimeters.

By design the calorimeter is compatible with a shower maximum detector. Indeed, the bicycle spoke positions are defined by the gaps between the shower maximum detector tiles. We additionally accommodate a pre-shower detector with a geometry appropriate for both behind the coil and in regions where only material from the tracking system is in front of the calorimeter.

Given the high radiation environment, and the $sin^{-3}\theta$ dependence of the radiation dose, we have designed the ECEM with a replaceable inner core so that radiation damaged tiles can be removed without disturbing the 80% of the calorimeter that is not expected to be damaged. While our current baseline shows fibers exiting the $| \eta |= 3.0$ boundary, we

are actively looking at low profile connectors so that all fibers can be routed to the outer perimeter.

The design of the calorimeter maintains the separation between the mechanical support of the absorber and the optical system. While the baseline design and cost estimate assumes individually wrapped tiles and silica readout fibers, the design can accommodate wide variations around this solution, from "multi-tiles" to new, radiation hard scintillators and WLS fibers as they are developed.

The basic design concept for the ECEM has be verified in the 4x4 calorimeter test station module. Hence, our immediate future plans for R&D center on the optical system. We know of no optical system which meets the speed, radiation, *and cost* requirements of the SDC. We are not satisfied with the light yield or life time of present tile fiber combinations and plan to investigate some new materials (*e.g.*WLS clad, high aperture silica fiber; or 3HF-O_2 tiles/fibers) and new photodetectors (*e.g.* avalanche photodiode photomultiplier) with higher quantum efficiency at red wavelengths. These optical R&D issues represent the highest priority for the group in the coming year and should culminate in a rebuilding and retest of the 4x4 calorimeter test station module during calender year 1993.

Table 8-1. Long term schedule for the ECEM calorimeter

Milestone	Date
Beam Test of 4x4 calorimeter	Summer 93
Design Review of 1/16 ECEM Wedge	Fall 93
Beam Test of 1/16 ECEM Wedge	Fall 94
Critical Design Review ECEM	Winter 94/95
Begin Assy of ECEM at LBL	Mar 96
Receive 1st ECEM at SSCL	Apr 97
Receive 2nd ECEM at SSCL	Oct 97
Beam test of 1st ECEM complete	Oct 97
Installation of 1st ECEM in SDC	Oct 98
Installation of 2nd ECEM in SDC	Nov 98

Longer term goals are summarized in table 8-1. This longer term schedule includes the following points:

- Test of the 4x4 with a new optics system in 1993, in addition to full working drawings of a 1/16 wedge by the end of 1993.
- Construction in 1994 of a 1/16 wedge module to verify the physical layout and fine tune the design parameters. This module would eventually be delivered to the SSCL for the response mapping of the full calorimeter (barrel and endcap) in the beam at SSCL. The first test of this device would be in the test beam at FNAL in late 1994 or early 1995.
- A critical design review in late 1994, early 1995, based on data collected in the FNAL beam test.
- First assembly of one of the full endcap calorimeters at LBL in 1996.

It is our intention that both endcaps are placed in the test beam at SSCL for full calibration. Given that the ECEM does not affect the magnetic field, we would plan to install the ECEM coincident with the installation of the tracking system, *i.e.* after the mapping of the solenoid field. This gives us the most flexibility in the schedule and provides an extra year to test the ECEM in the beam. Overall we feel the schedule is reasonable, and allows us time to meet the design goals for the ECEM and schedule of the experiment.

To conclude, the monolithic ECEM design presented in this report here appears to meet the objectives of SDC while minimizing inert material in the active volume of the electromagnetic calorimeter and maximizing the acceptance for electrons and photons in the endcap region.

9. Appendix A: Surface operations at SSCL

1) Arrival:

   a) From LBL, monolithic assembly, 5.3 m dia., 30 tons, on truck (wide load) or railcar.

   b) Unloading via Assembly Building crane, rotation to horizontal plane using provided fixtures.

   c) Inspection and testing using source calibration system ($\approx$ 2 months)

2) Interim Storage:

   a) Store in vertical orientation in the assembly area using lifting/storage fixture.

3) Beamline Calibration:

   a) Transport to fixed-target hall (across site). truck? rail? Assume use of shipping fixtures.

   b) Unloading, mounting in calibration fixture

   c) Calibration run - 1003 months)

4) Interim Storage:

   a) Transport to storage area, store in vertical orientation using lifting/storage fixture.

   (Option: Subject to space and schedule constraints, the ECEM could be delivered directly to the test beam facility for source testing and calibration, thus eliminating one cross-site transportation link.)

(Repeat all of the above for second ECEM)

5) Installation:

   a) Lower into experiment hall using crane or elevator.

   b) Mount on inner face of Hadronic Endcap, using crane lifting fixture.

   c) Verify integrity with source calibration system.

   d) Repeat for second ECEM

6) Eventual Reconditioning for Radiation Damage:

   a) During major shutdown, remove ECEMs to Surface Assembly Building

b) Rotate to horizontal plane on work support fixtures.

c) Rebuilding of inner core (2 months?)

d) Re-installation in calorimeter

(Note: Shutdown schedule may dictate that both ECEMs be reconditioned simultaneously.)

10. Appendix B: Drawings for Vendor Quotes

The cost of most of the mechanical parts for the ECEM have been estimated by vendor quotes. In this appendix we present (reduced) copies of the drawings sent to vendors for estimating purposes.

REQD	ITEM	PART NUMBER	DESCRIPTION
1			PLATE 1/2" THK x 108" W - ALUMINUM 6061-T6

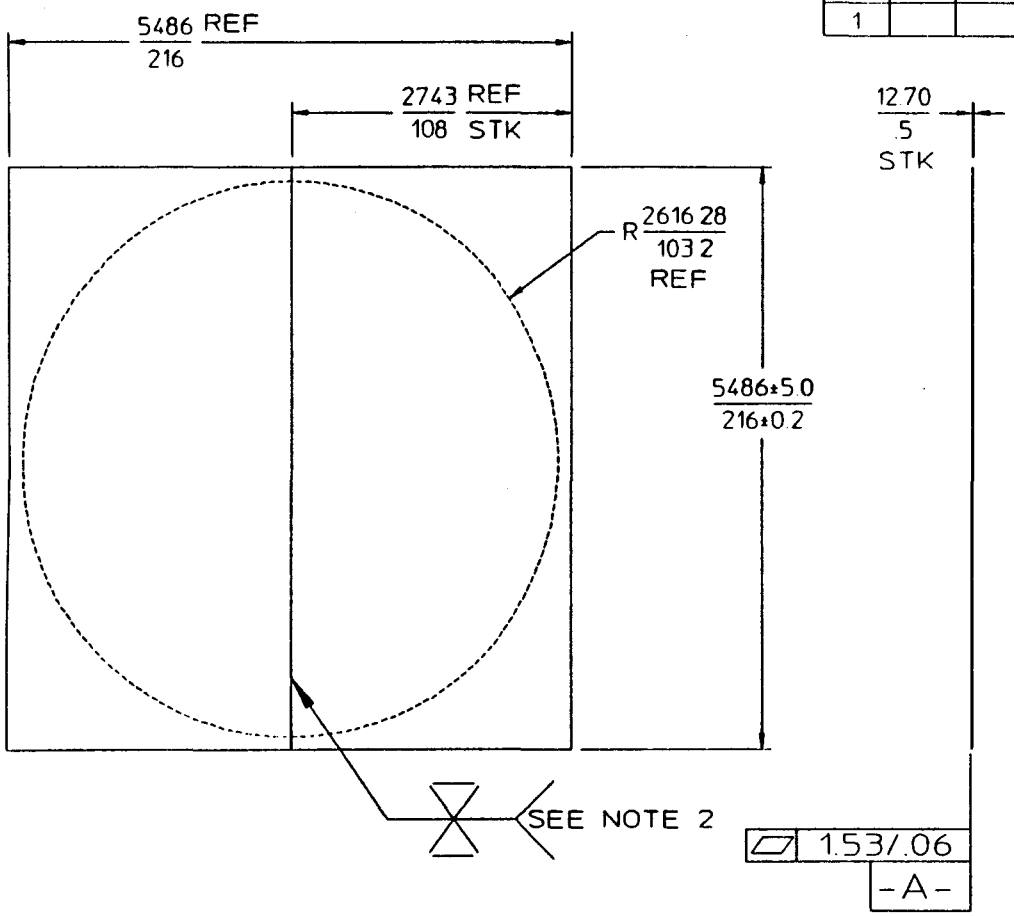

NOTE: Unless otherwise specified

1. DIMENSIONS ARE MILLIMETRE / INCH ; MILLIMETRE/INCH.
2. FULL PENETRATION "V" WELD FROM ONE SIDE ONLY IS ACCEPTABLE.

REV	DWN	CHK	DATE	DESCRIPTION

UNLESS OTHERWISE SPECIFIED
TOLERANCES AS NOTED
SURFACE FINISH 125 √

1. SAWED, FLAMECUT, SHEARED OR CUT STOCK FINISH.
2. THREADS CLASS 2.
3. CHAMFER ENDS OF ALL SCREW THRDS 30°.
4. 1 1/2 PITCH RELIEF WITH ROUND NOSE TOOL ON ALL MACHINE CUT THRDS
5. BREAK EDGES 1/64 MAX ON MACHINE WORK.
6. REMOVE BURRS, LOOSE SCALE AND WELD SPLATTER
7. REF.-USASI OR ASA STDS SECT Y-14 & B46-1.

SHOP ORDERS

ACCT NO	SER NO	
DATE ISSD	DATE REQD	NO REQD
DELIVER TO		
SURFACE TREATMENT	DEGREASE	
IDENTIFIC METHOD		
DWG BY lim	DATE 09-01-92	
CHK BY	DATE 00-00-00	

LAWRENCE BERKELEY LABORATORY
UNIVERSITY OF CALIFORNIA-BERKELEY

SDC DETECTOR
ENDCAP CALORIMETER
FRONT PLATE WELDMENT

PAT CLEAR	DWG TYPE	SHOWN ON	SCALE: 1/50
	DETAIL		DO NOT SCALE PRINTS
MICROFILMED	DESIGN ACCT NO 8817-11	CATEGORY CODE	DWG NO 20M9002 REV

REQD	ITEM	PART NUMBER	DESCRIPTION
1			PLATE 1/2" THK. x 108" W. - ALUMINUM 6061-T6

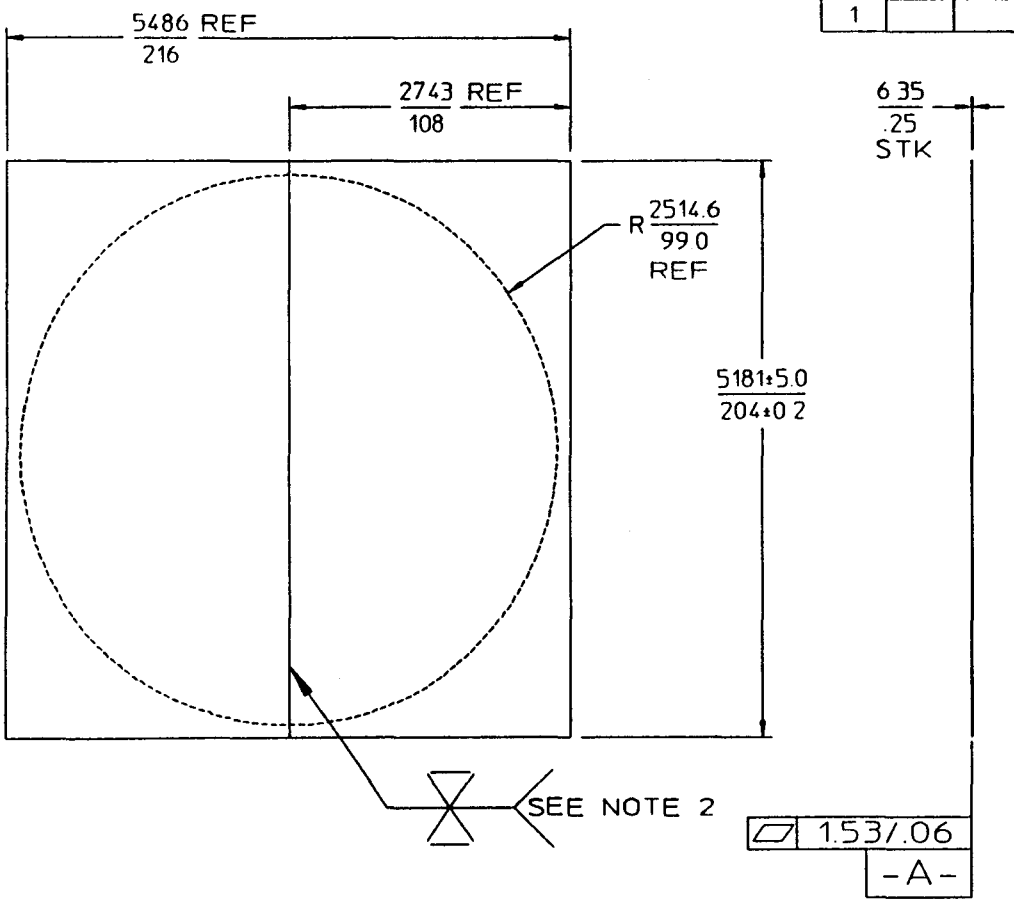

NOTE: Unless otherwise specified

1. DIMENSIONS IN MILLIMETRE/INCH, MILLIMETRE/INCH.
2. FULL PENETRATION "V" WELD FROM ONE SIDE ONLY IS ACCEPTABLE.

REV	DWN	CHK	DATE	DESCRIPTION

UNLESS OTHERWISE SPECIFIED
TOLERANCES AS NOTED
SURFACE FINISH 125

1. SAWED, FLAMECUT, SHEARED OR CUT STOCK FINISH.
2. THREADS CLASS 2.
3. CHAMFER ENDS OF ALL SCREW THRDS 30°
4. 1 1/2 PITCH RELIEF WITH ROUND NOSE TOOL ON ALL MACHINE CUT THRDS.
5. BREAK EDGES 1/64 MAX. ON MACHINE WORK
6. REMOVE BURRS, LOOSE SCALE AND WELD SPLATTER
7. REF.-USASI OR ASA STDS SECT Y-14 & B46-1

SHOP ORDERS

ACCT NO	SER NO	
DATE ISSD	DATE REQD	NO REQD
DELIVER TO		
SURFACE TREATMENT	DEGREASE	
IDENTIFIC METHOD		
DWG BY	lim	DATE 09-01-92
CHK BY		DATE 00-00-00

LAWRENCE BERKELEY LABORATORY
UNIVERSITY OF CALIFORNIA-BERKELEY

SDC DETECTOR
ENDCAP CALORIMETER
BACK PLATE WELDMENT

PAT CLEAR	DWG TYPE	SHOWN ON	SCALE: 1/50
	DETAIL		DO NOT SCALE PRINTS
MICROFILMED	DESIGN ACCT NO 8817-11	CATEGORY CODE	DWG NO 20M9012 REV

REQ	ITEM	PART NUMBER	DESCRIPTION
3			SHEET, 1.5 MM THICK, 70 IN X 210 IN , 6061-T6

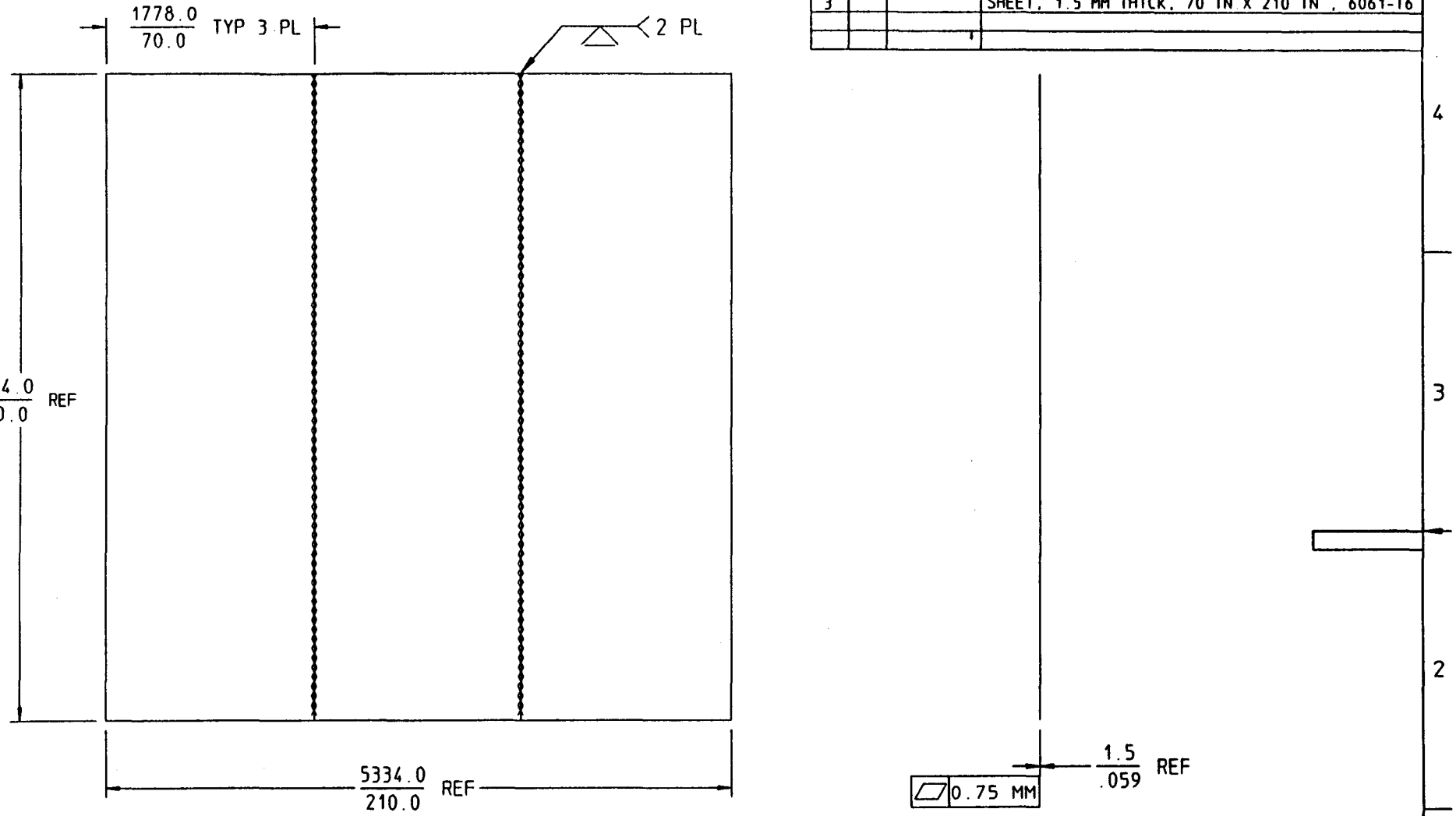

NOTE: 1. ALL DIMENSIONS ARE IN MILLIMETERS OVER INCHES.
2. LAY FINISHED SHEETS ON FLAT SURFACE AND PROTECT FROM DAMAGE.

REV	DWG	CHK	ZONE	DATE	CHANGES

UNLESS OTHERWISE SPECIFIED

TOLERANCES			
X ±	FRAC. ±		
.XX ±	ANGLES ±		
XXX ±	FINISH √		

THREADS ARE CLASS 2
CHAMFER ENDS OF ALL SCREW THREADS 30°
CUT 1.5 PITCH TWO RELIEF WITH ROUND NOSE TOOL ON MACHINE CUT THREADS.
BREAK EDGES .016 MAX ON MACHINED WORK
REMOVE BURRS WELD SPLATTER & LOOSE SCALE
REFERENCES: ANSI Y14.5 & B46.1

SHOP ORDERS

ACCT NO		SERIAL NO.	
DATE ISSD.	DATE REQD	NO. REQD.	
DELIVER TO			
SURFACE TREATMENT	DEGREASE		
IDENT METH.			
DWG BY	MINAMIHARA	DATE	8-15-92
CHK. BY		DATE	

LAWRENCE BERKELEY LABORATORY
UNIVERSITY OF CALIFORNIA-BERKELEY

SSC DETECTOR
ENDCAP CALORIMETER
1.5MM AL SHEET WELDMENT

PATENT CLEAR	DWG TYPE DETAIL	SHOWN ON	SCALE 1/25	DO NOT SCALE PRINTS
MICROFILMED	DESIGN ACCT. NO. 8817-11	CATEGORY CODE	DWG NO 20M9023	SIZE / REV.

10-4

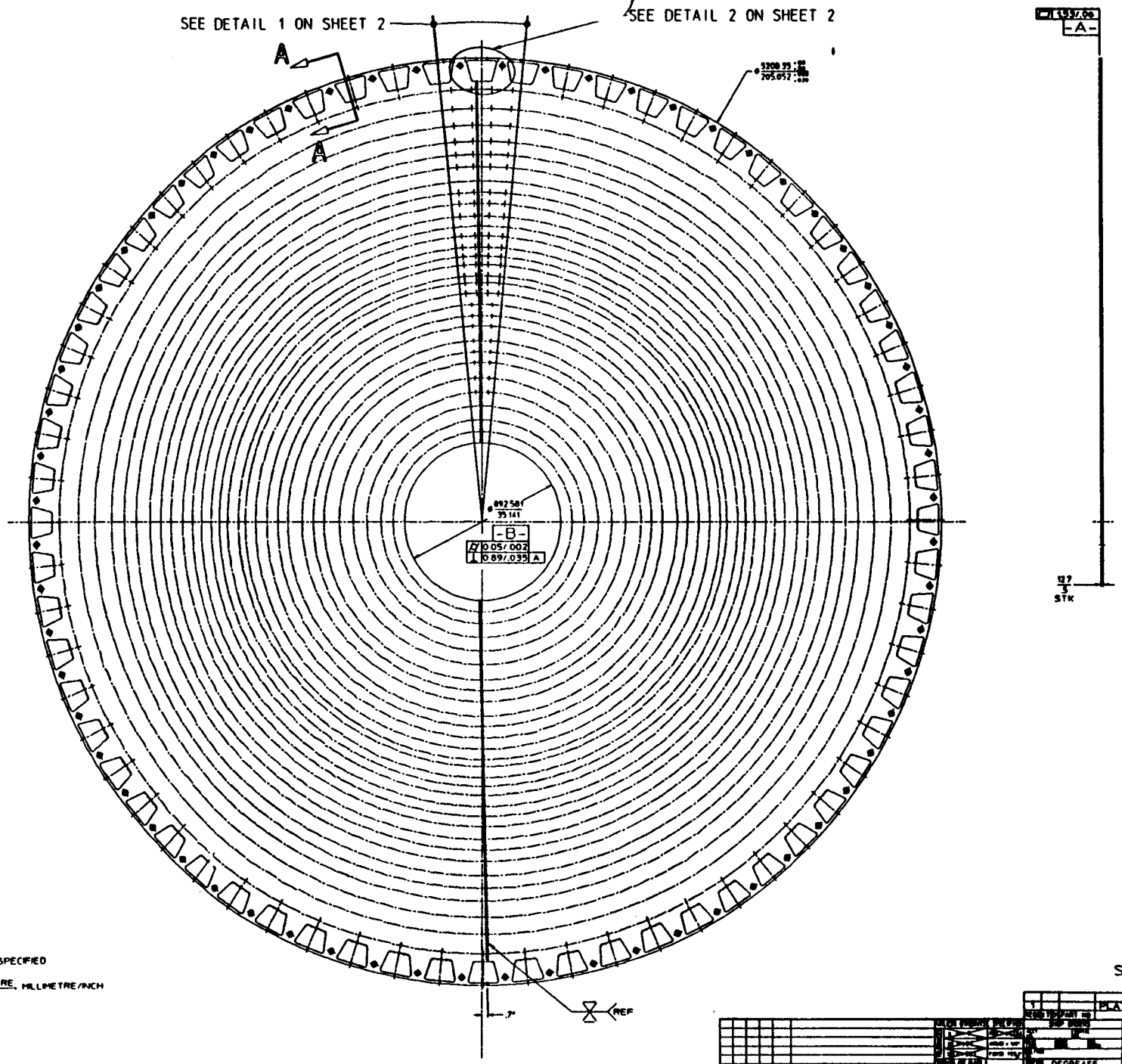

NOTES: UNLESS OTHERWISE SPECIFIED

1 DIMENSIONS ARE MILLIMETRE/INCH, MILLIMETRE/INCH

SHEET 1 OF 2

PLATE - 1/2" THK ALUM 6061-T6

LAWRENCE BERKELEY LABORATORY
UNIVERSITY OF CALIFORNIA-BERKELEY

SDC DETECTOR
ENDCAP CALORIMETER
FRONT PLATE

DEGREASE

1/8

2049034

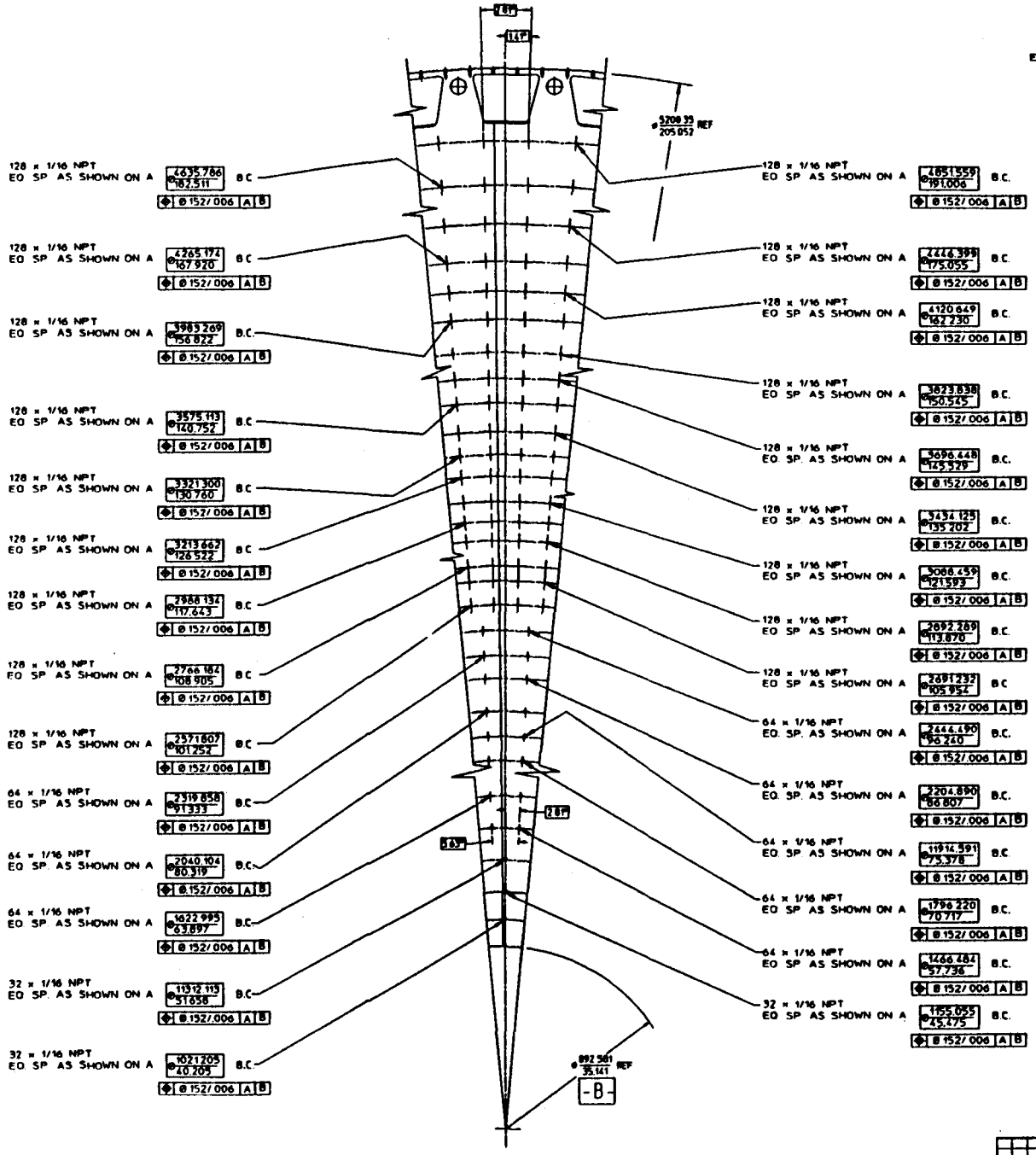

DETAIL 1
TYP. 64 PLACES

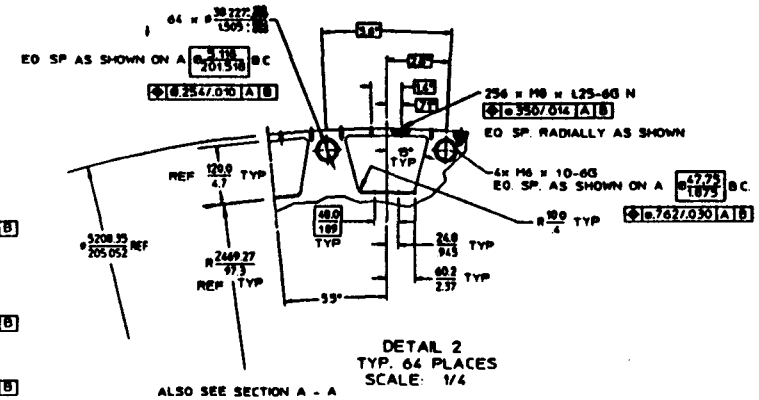

DETAIL 2
TYP. 64 PLACES
SCALE: 1/4

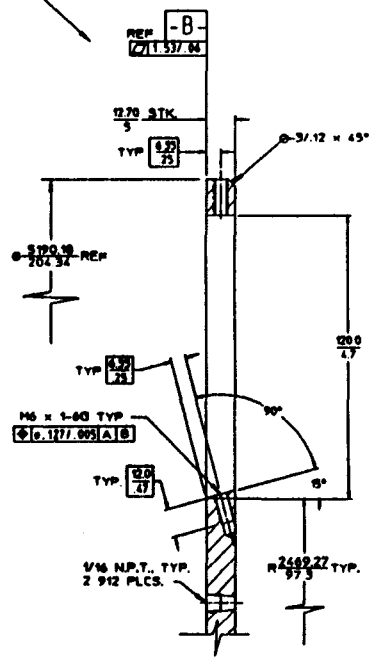

SECTION A - A
ROTATED CW 17°
SCALE: NONE

SHEET 2 OF 2

LAWRENCE BERKELEY LABORATORY
UNIVERSITY OF CALIFORNIA-BERKELEY
SDC DETECTOR
ENDCAP CALORIMETER
FRONT PLATE
DETAIL
2019903-1

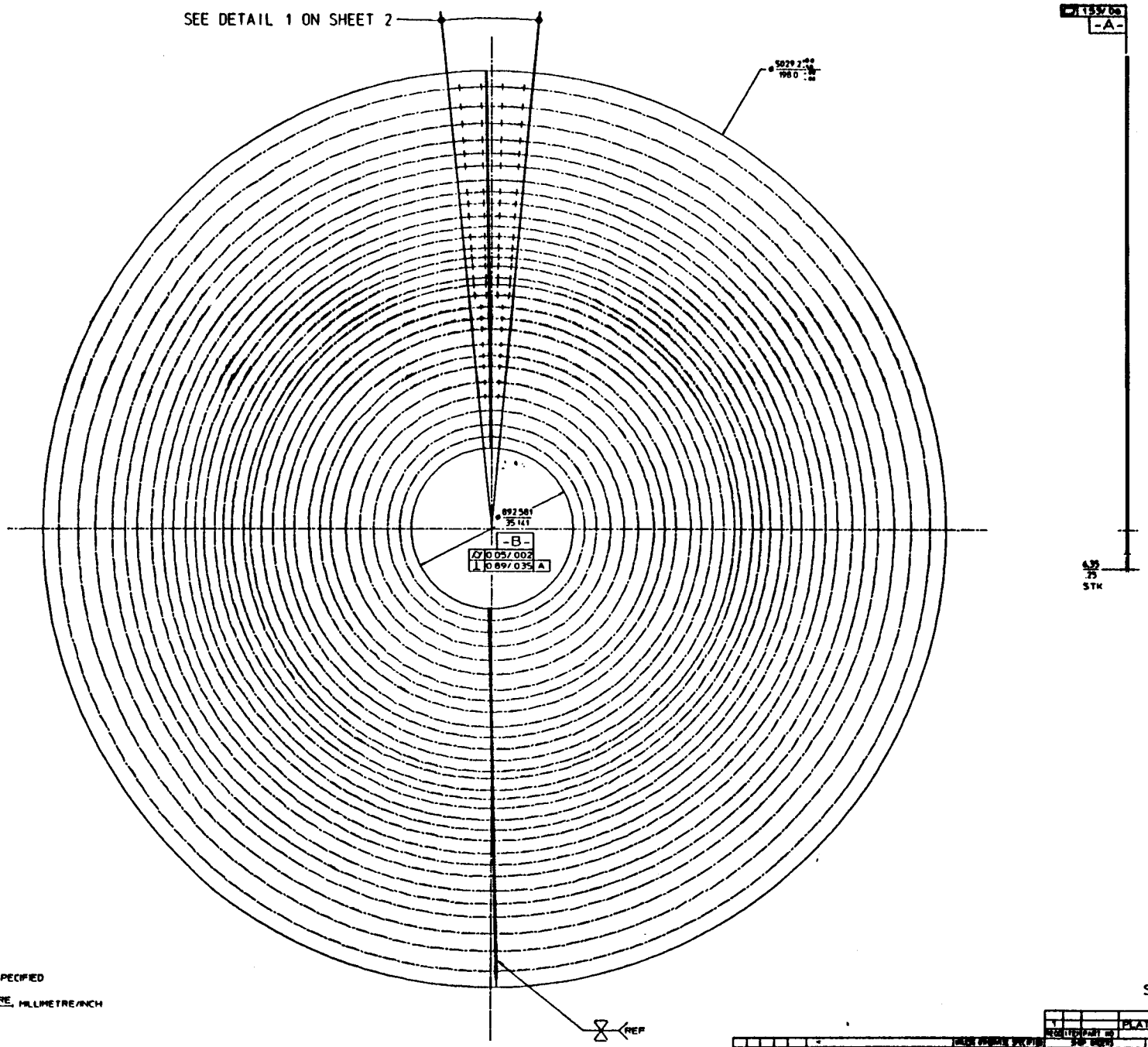

NOTES: UNLESS OTHERWISE SPECIFIED

1 DIMENSIONS ARE MILLIMETRE/INCH, MILLIMETRE/INCH

SHEET 1 OF 2

PLATE - 1/2" THK ALUM 6061-T6

LAWRENCE BERKELEY LABORATORY

UNIVERSITY OF CALIFORNIA-BERKELEY

SDC DETECTOR

ENDCAP CALORIMETER

BACK PLATE

1/50

2049044

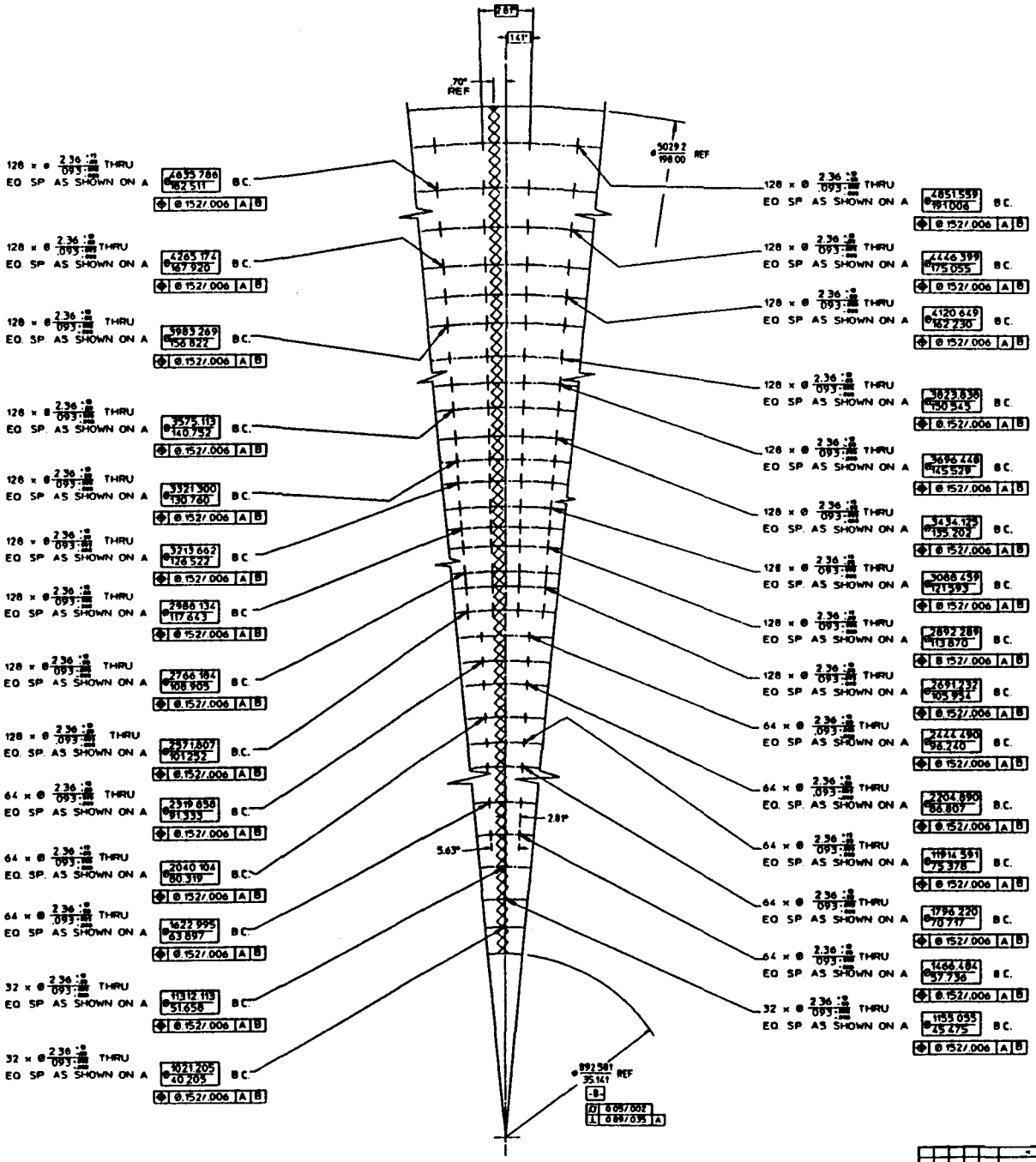

DETAIL 1
TYP. 64 PLACES

NOTE: UNLESS OTHERWISE SPECIFIED

1. DIMENSIONS ARE MILLIMETRE / INCH, MILLIMETRE/INCH

DEGREASE	DESCRIPTION: LAWRENCE BERKELEY LABORATORY, UNIVERSITY OF CALIFORNIA-BERKELEY; SSC DETECTOR; ENDCAP CALORIMETER; BACK PLATE	
	DETAIL	12019044

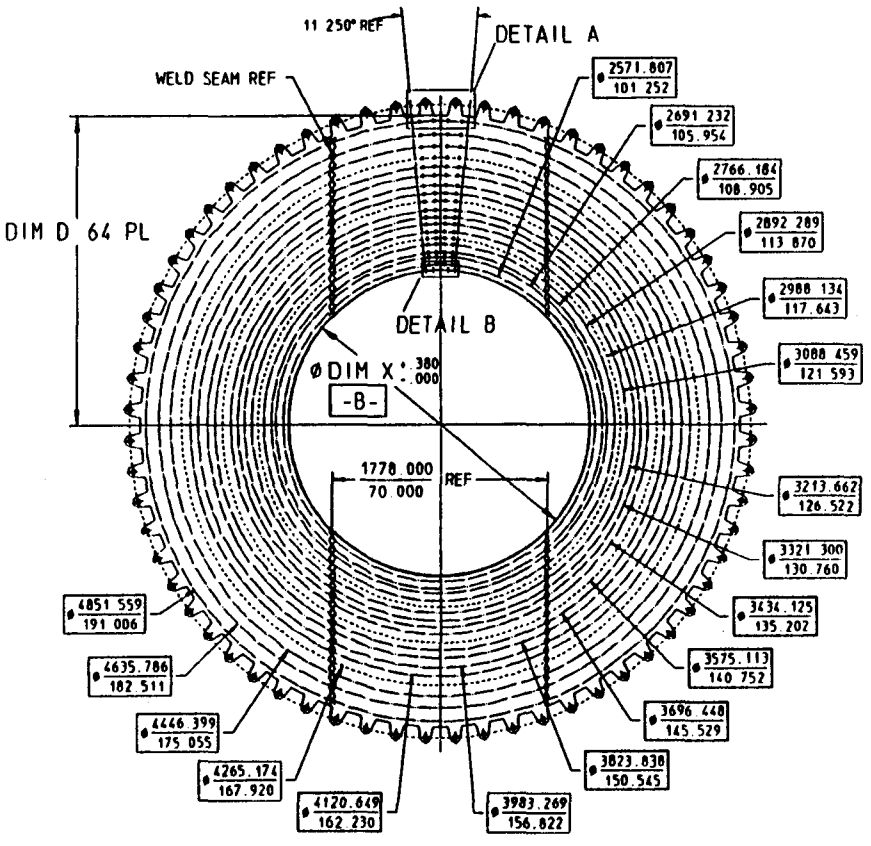

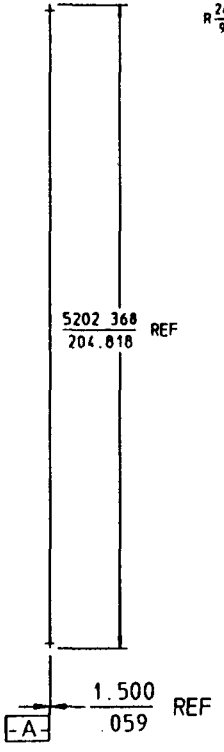

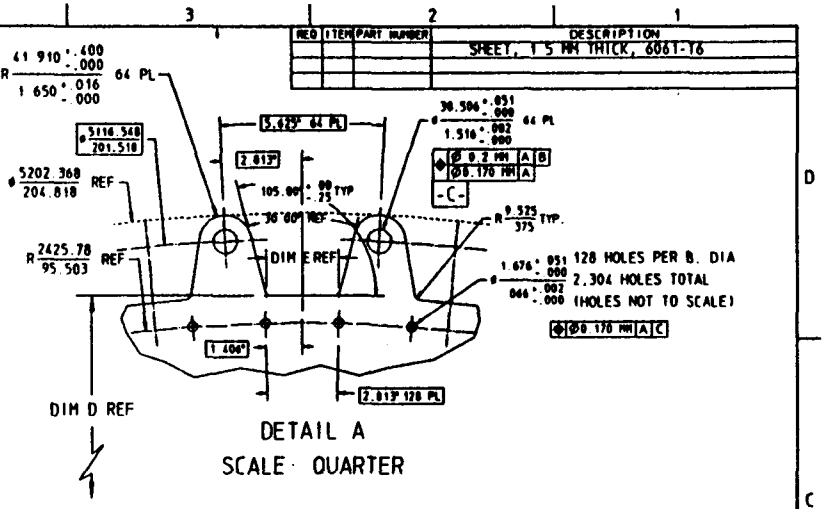

DETAIL A
SCALE QUARTER

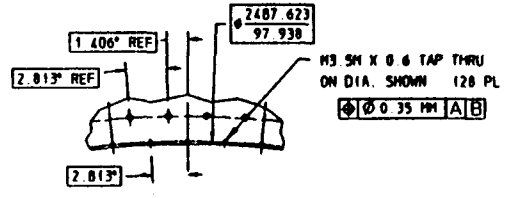

DETAIL B
SCALE QUARTER
NOTE: ALL HOLES NOT TO SCALE.

NOTE: 1 ALL DIMENSIONS ARE IN MILLIMETERS OVER INCHES.
2 BE SURE TO SAVE AND PROTECT THE CORE SHEET FOR FURTHER MACHINING.

REQ	ITEM	PART NUMBER	DESCRIPTION
			SHEET, 1.5 MM THICK, 6061-T6

REV	DWG	CHK	ZONE	DATE	CHANGES

UNLESS OTHERWISE SPECIFIED
DIMENSIONS: .XX ±, .XXX ±, .XXXX ±, ANGLES ±0.1°, FINISH 125
THREADS ARE CLASS 2
CHAMFER EDGES OF ALL SCREW HOLES 30°
FOR 1.5 PITCH THRU SHOP HOLES ADD THREE
ON MACHINE CUT EDGES
BREAK EDGES
REMOVE BURRS AND SPLINTER & LOOSE SCALE
REFERENCES ANSI Y14.5 & B46.1.

SHOP ORDERS
REV. / DATE / INITIAL
DRAWN: MINAMIHARA 2-27-97
CHECKED
ENGINEER
SUPERVISOR
APPROVED

LAWRENCE BERKELEY LABORATORY
UNIVERSITY OF CALIFORNIA-BERKELEY
SDC DETECTOR
ENDCAP CALORIMETER
OUTER CURTAIN
PATENT CLEAR | DWG. TYPE DETAIL | SHEET 1/20 | SIZE | REV.
INTERPRETATION | DWG. NO. 8817-11 | CONTROL CODE | DWG. ID 20M9054

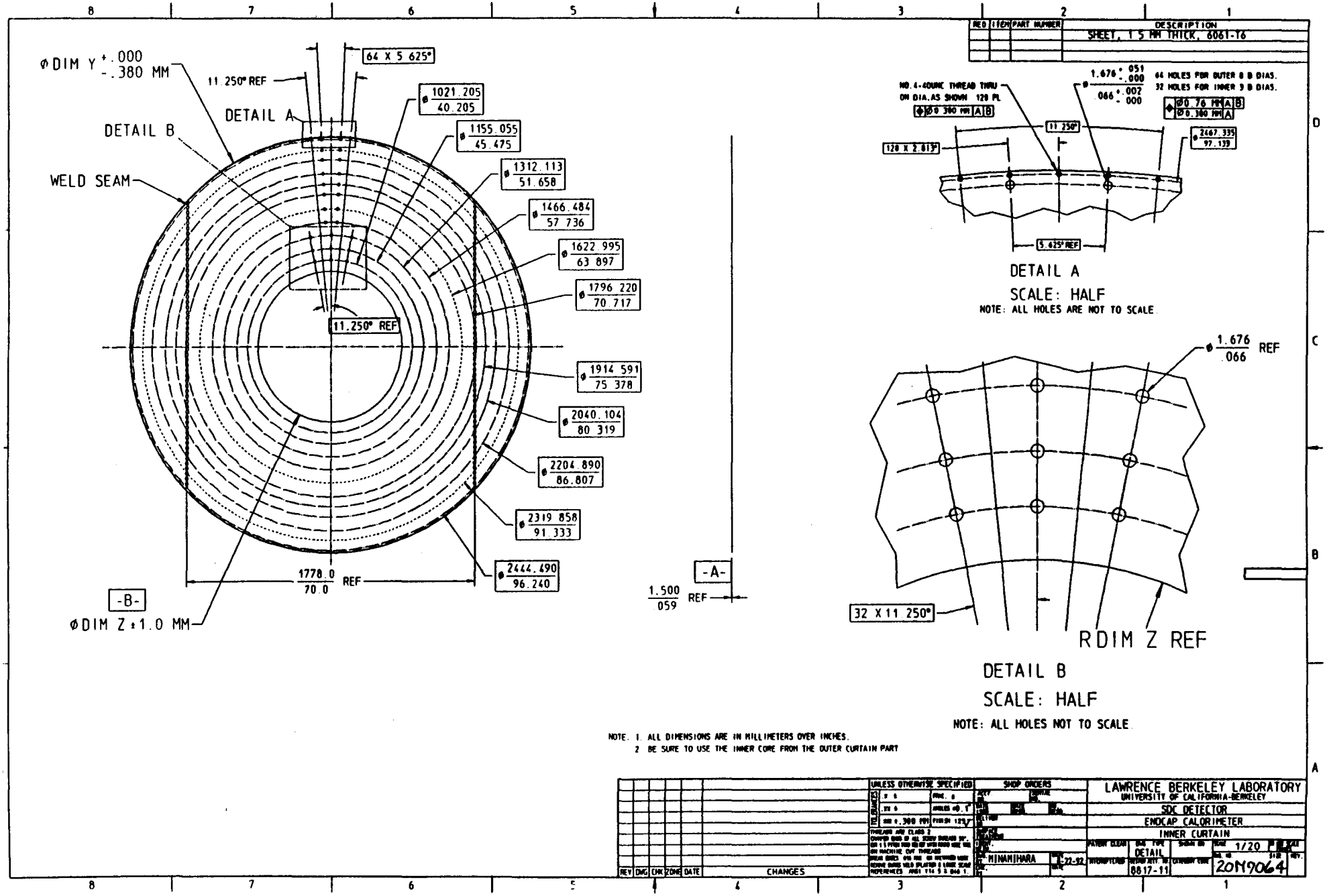
REQ ITEM PART NUMBER DESCRIPTION
SHEET, 1.5 MM THICK, 6061-T6
ØDIM Y +.000 -.380 MM
11.250° REF
64 X 5.625°
DETAIL A
DETAIL B
WELD SEAM
Ø 1021.205 / 40.205
Ø 1155.055 / 45.475
Ø 1312.113 / 51.658
Ø 1466.484 / 57.736
Ø 1622.995 / 63.897
Ø 1796.220 / 70.717
11.250° REF
Ø 1914.591 / 75.378
Ø 2040.104 / 80.319
Ø 2204.890 / 86.807
Ø 2319.858 / 91.333
Ø 2444.490 / 96.240
1778.0 / 70.0 REF
-B-
ØDIM Z ±1.0 MM
-A-
1.500 / .059 REF
NO. 4-40UNC THREAD THRU ON DIA. AS SHOWN 120 PL
Ø0.380 MM A B
1.676 +.051 -.000
.066 +.002 -.000
64 HOLES FOR OUTER 8 B DIAS.
32 HOLES FOR INNER 9 B DIAS.
Ø0.76 MM A B
Ø0.380 MM A
11.250°
120 X 2.813°
Ø 2467.335 / 97.139
5.625° REF
DETAIL A
SCALE: HALF
NOTE: ALL HOLES ARE NOT TO SCALE.
Ø 1.676 / .066 REF
32 X 11.250°
RDIM Z REF
DETAIL B
SCALE: HALF
NOTE: ALL HOLES NOT TO SCALE.
NOTE. 1. ALL DIMENSIONS ARE IN MILLIMETERS OVER INCHES.
2. BE SURE TO USE THE INNER CORE FROM THE OUTER CURTAIN PART
REV DWG CHK ZONE DATE CHANGES
UNLESS OTHERWISE SPECIFIED
SHOP ORDERS
MINAMIHARA
LAWRENCE BERKELEY LABORATORY
UNIVERSITY OF CALIFORNIA-BERKELEY
SDC DETECTOR
ENDCAP CALORIMETER
INNER CURTAIN
DETAIL
8817-11
1/20
20M9064

CURTAIN

Z Dim Face of Hadronic Rec		4850.000								
Zgap		0.000								
Zface		30.070			Disk No. 24					
Cut-width		0.500		Dim Z	Dim Y	Dim X				
Starting Pt. =	(Zhad+Zgap)*TAN(ata) =			961.066	2657.908	2656.908				
Disk Name	No. Req'd	Al Shts/Disk	Total Shts Req'd	Total Wt	Mat'l Cost	Holes/11.25d	Total Holes	Dim X	Dim Y	Dim Z
			(70"X210"X1.5mm)							
Outer	48	3	144	12,226.85	$29,344.44					
D1	2	3	6			72	2304	2479.965		
D2	2	3	6			72	2304	2487.685		
D3	2	3	6			72	2304	2495.405		
D4	2	3	6			72	2304	2503.126		
D5	2	3	6			72	2304	2510.846		
D6	2	3	6			72	2304	2518.566		
D7	2	3	6			72	2304	2526.286		
D8	2	3	6			72	2304	2534.006		
D9	2	3	6			72	2304	2543.105		
D10	2	3	6			72	2304	2550.825		
D11	2	3	6			72	2304	2558.545		
D12	2	3	6			72	2304	2566.266		
D13	2	3	6			72	2304	2573.986		
D14	2	3	6			72	2304	2581.706		
D15	2	3	6			72	2304	2589.426		
D16	2	3	6			72	2304	2597.146		
D17	2	3	6			72	2304	2604.867		
D18	2	3	6			72	2304	2612.587		
D19	2	3	6			72	2304	2620.307		
D20	2	3	6			72	2304	2628.027		
D21	2	3	6			72	2304	2635.747		
D22	2	3	6			72	2304	2643.467		
D23	2	3	6			72	2304	2651.188		
D24	2	3	6			72	2304	2656.908		
Totals	48	72	144			1728	55296			
Inner										
D1	2					19	608		2478.965	896.282
D2	2					19	608		2486.685	899.077
D3	2					19	608		2494.405	901.872
D4	2					19	608		2502.126	904.667
D5	2					19	608		2509.846	907.462
D6	2					19	608		2517.566	910.257
D7	2					19	608		2525.286	913.052
D8	2					19	608		2533.006	915.847
D9	2					19	608		2542.105	919.141
D10	2					19	608		2549.825	921.936
D11	2					19	608		2557.545	924.731
D12	2					19	608		2565.266	927.526
D13	2					19	608		2572.986	930.321
D14	2					19	608		2580.706	933.116
D15	2					19	608		2588.426	935.911
D16	2					19	608		2596.146	938.706
D17	2					19	608		2603.867	941.501
D18	2					19	608		2611.587	944.296
D19	2					19	608		2619.307	947.091
D20	2					19	608		2627.027	949.886
D21	2					19	608		2634.747	952.681
D22	2					19	608		2642.467	955.476
D23	2					19	608		2650.188	958.271
D24	2					19	608		2657.908	961.066
Totals	48					456	14592			

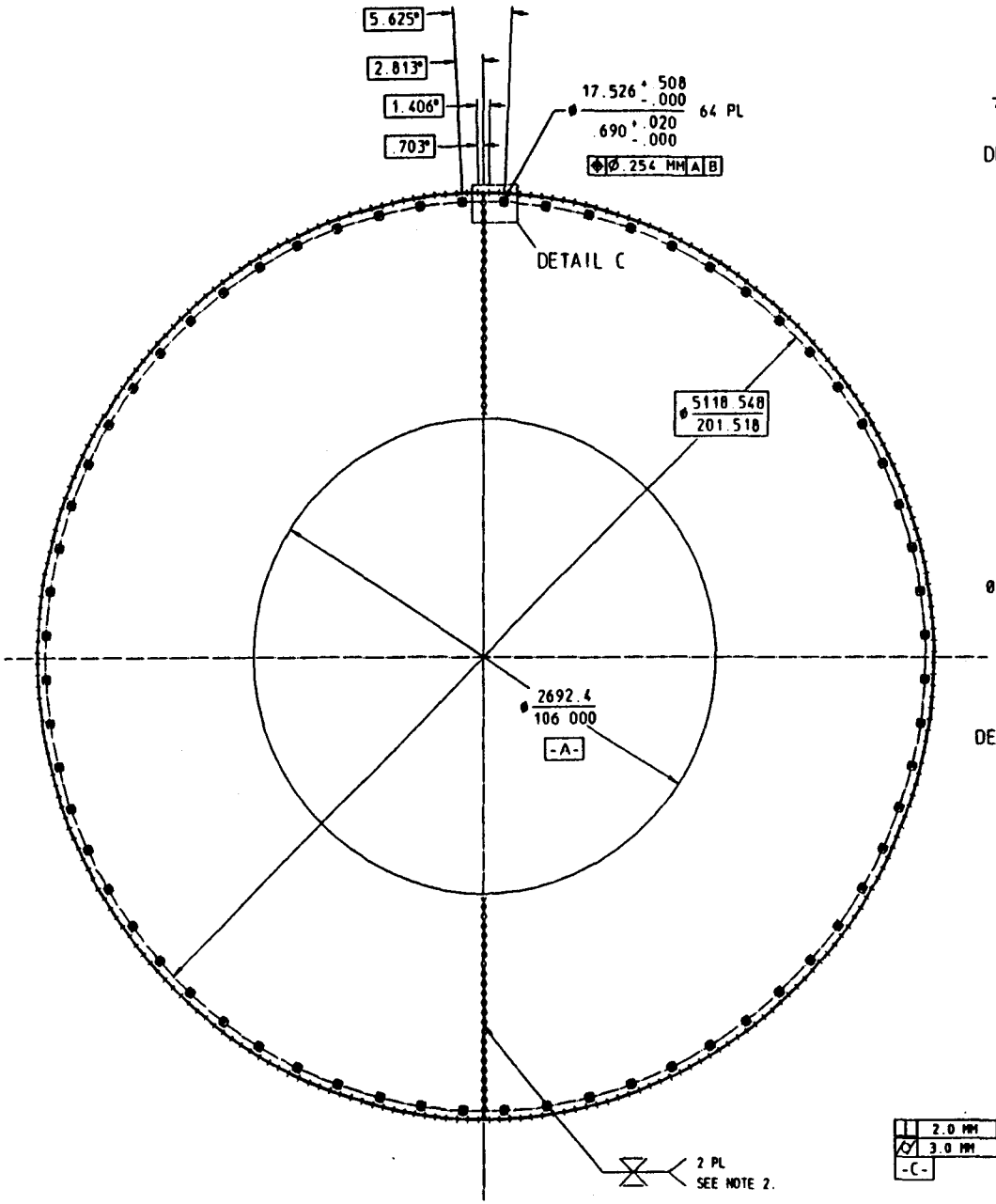

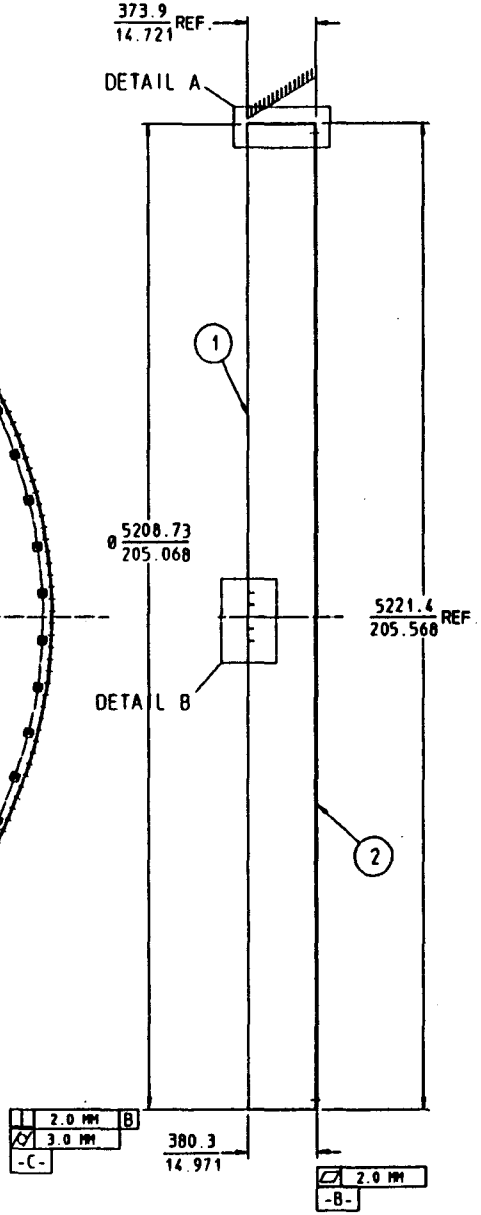

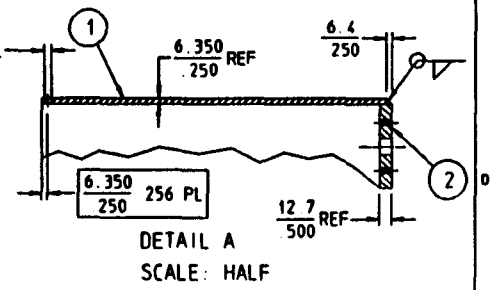

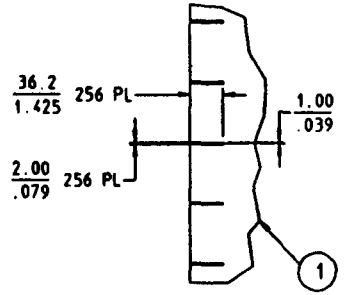

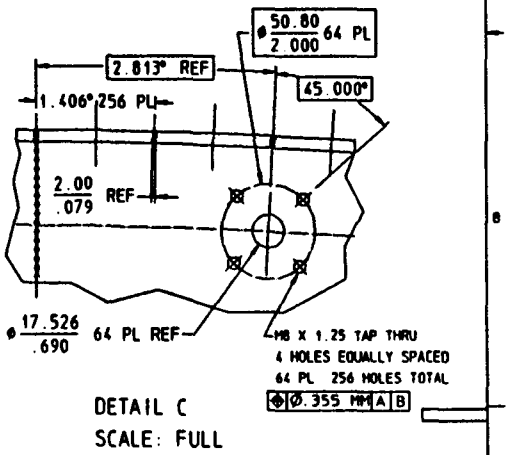

NOTE 1. ALL DIMENSIONS ARE IN MILLIMETERS OVER INCHES
2. CAN BE A 'V' WELD ONLY FROM ONE SIDE WITH FULL PENETRATION

2	A/R	PLATE, ASM1-16, 1/2 INCH THICK
1	A/R	PLATE, ASM1-16, 1/4 INCH THICK
REQ	PART NO	DESCRIPTION

LAWRENCE BERKELEY LABORATORY
UNIVERSITY OF CALIFORNIA-BERKELEY
SDC DETECTOR
ENDCAP CALORIMETER
CAN
DEGREASE
RIMARINA
DETAIL
1/10
20M9016

10-12

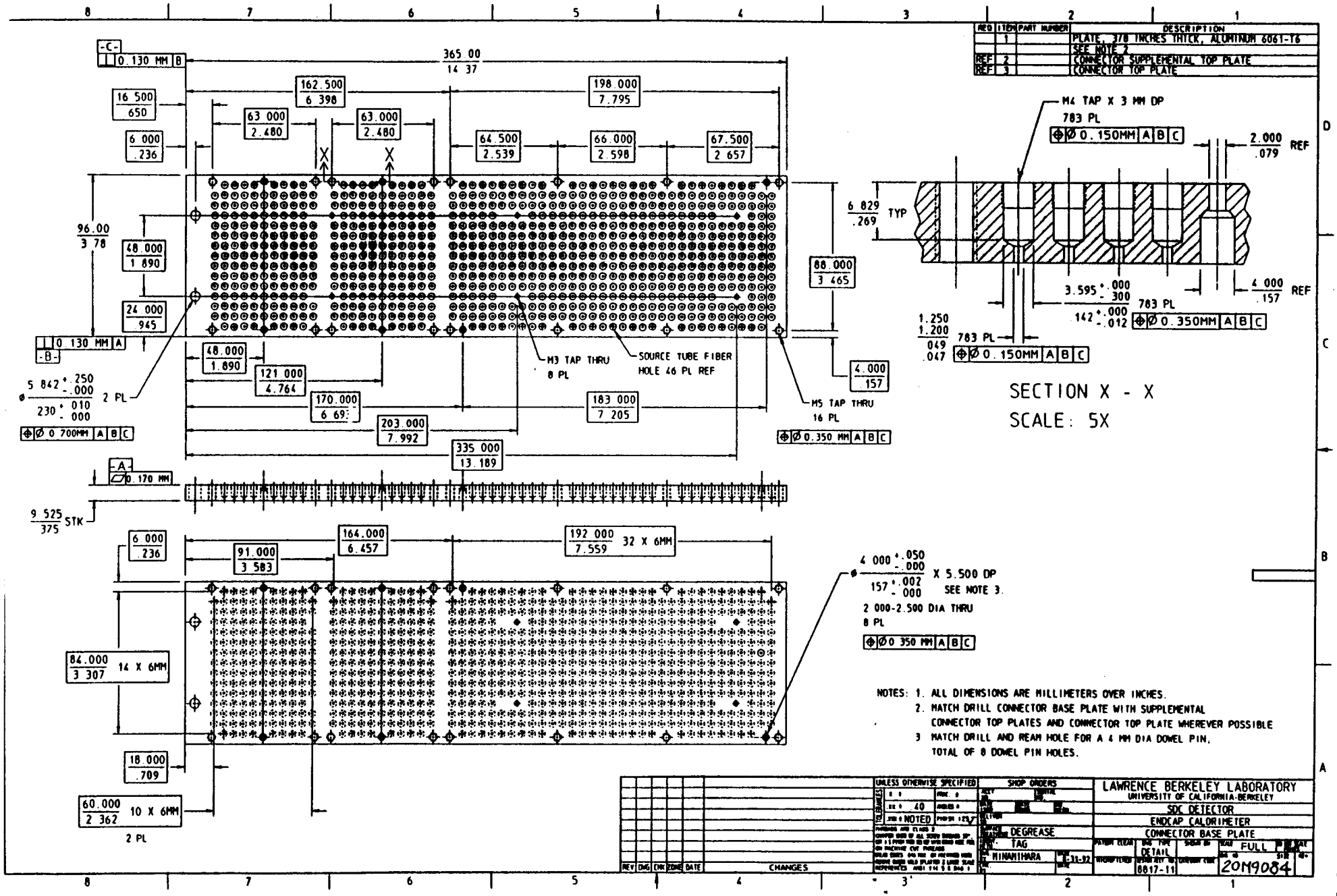
REQ ITEM PART NUMBER DESCRIPTION
1 PLATE, 3/8 INCHES THICK, ALUMINUM 6061-T6 SEE NOTE 2
REF 2 CONNECTOR SUPPLEMENTAL TOP PLATE
REF 3 CONNECTOR TOP PLATE
365.00 / 14.37
162.500 / 6.398
198.000 / 7.795
16.500 / .650
63.000 / 2.480
63.000 / 2.480
64.500 / 2.539
66.000 / 2.598
67.500 / 2.657
6.000 / .236
96.00 / 3.78
48.000 / 1.890
24.000 / .945
88.000 / 3.465
4.000 / .157
48.000 / 1.890
121.000 / 4.764
170.000 / 6.69
183.000 / 7.205
203.000 / 7.992
335.000 / 13.189
M3 TAP THRU 8 PL
SOURCE TUBE FIBER HOLE 46 PL REF
M5 TAP THRU 16 PL
5.842 +.250 -.000 / 230 +.010 -.000 2 PL
9.525 / .375 STK
6.000 / .236
91.000 / 3.583
164.000 / 6.457
192.000 / 7.559 32 X 6MM
84.000 / 3.307 14 X 6MM
18.000 / .709
60.000 / 2.362 10 X 6MM 2 PL
4.000 +.050 -.000 / 157 +.002 -.000 X 5.500 DP SEE NOTE 3.
2.000-2.500 DIA THRU 8 PL
M4 TAP X 3 MM DP 783 PL
6.829 / .269 TYP
2.000 / .079 REF
4.000 / .157 REF
3.595 +.000 -.300 783 PL
142 +.000 -.012
1.250 / 1.200
.049 / .047
783 PL
SECTION X - X
SCALE: 5X
NOTES: 1. ALL DIMENSIONS ARE MILLIMETERS OVER INCHES.
2. MATCH DRILL CONNECTOR BASE PLATE WITH SUPPLEMENTAL CONNECTOR TOP PLATES AND CONNECTOR TOP PLATE WHEREVER POSSIBLE
3 MATCH DRILL AND REAM HOLE FOR A 4 MM DIA DOWEL PIN, TOTAL OF 8 DOWEL PIN HOLES.
UNLESS OTHERWISE SPECIFIED
SHOP ORDERS
DEGREASE
TAG
MINAMIHARA
LAWRENCE BERKELEY LABORATORY
UNIVERSITY OF CALIFORNIA-BERKELEY
SDC DETECTOR
ENDCAP CALORIMETER
CONNECTOR BASE PLATE
DETAIL
8817-11
FULL
20M9084
CHANGES

REQ	ITEM	PART NUMBER	DESCRIPTION
	1		PLATE, .378 INCHES THICK, ALUMINUM 6061-T6 SEE NOTE 2
REF	2		CONNECTOR BASE PLATE
REF	3		CONNECTOR SUPPLEMENTAL TOP PLATE

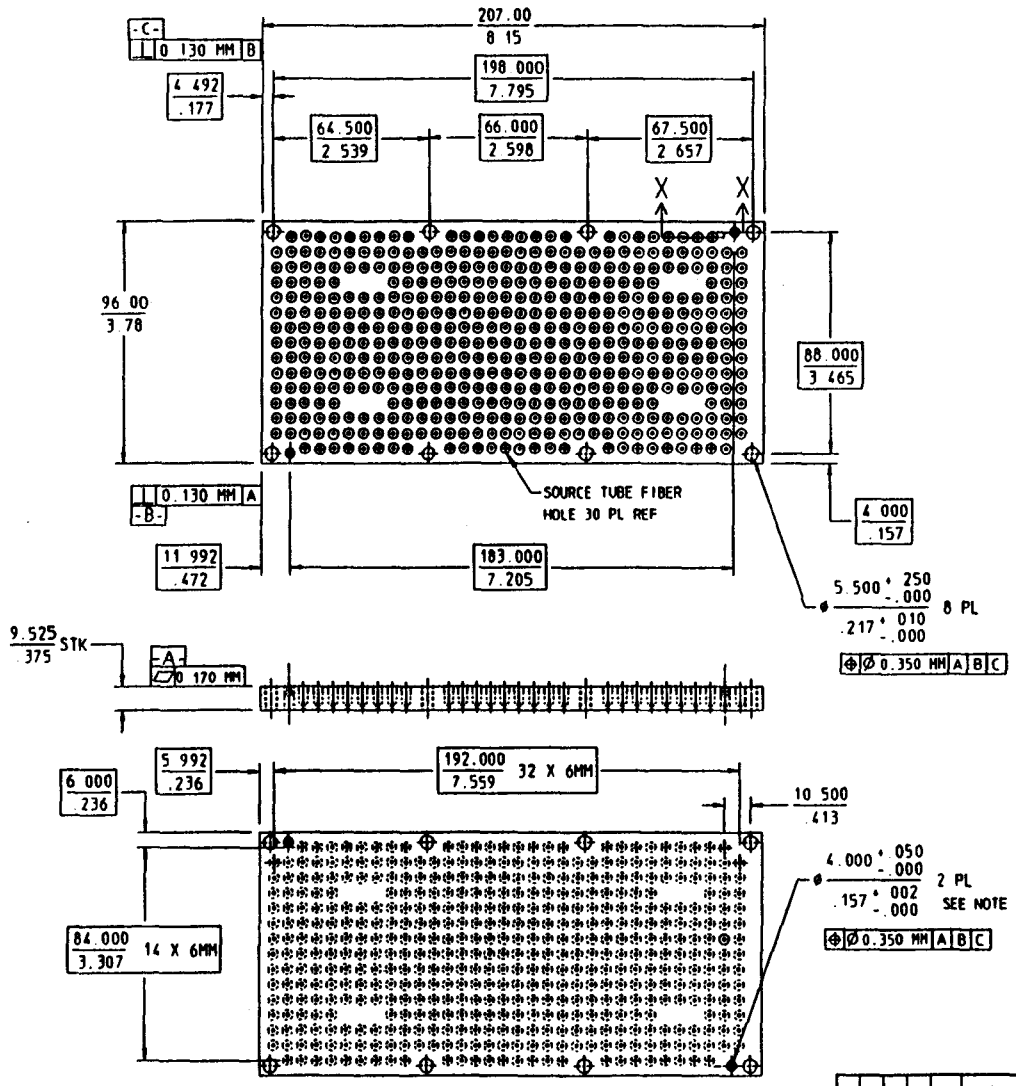

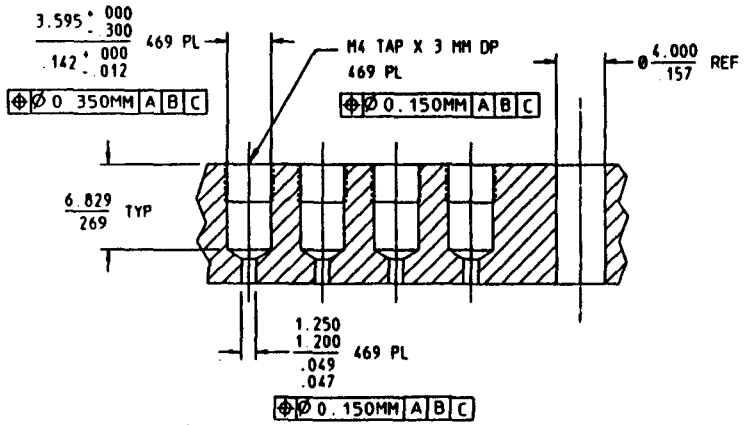

SECTION X - X
SCALE: 5X

NOTES:
1. ALL DIMENSIONS ARE MILLIMETERS OVER INCHES.
2. MATCH DRILL CONNECTOR BASE PLATE WITH SUPPLEMENTAL CONNECTOR TOP PLATES AND CONNECTOR TOP PLATE WHEREVER POSSIBLE.
3. MATCH DRILL AND REAM HOLE FOR A 4 MM DIA DOWEL PIN, TOTAL OF 8 DOWEL PIN HOLES.

REV	DWG	CHK	ZONE	DATE	CHANGES

UNLESS OTHERWISE SPECIFIED
.40
NOTED

SHOP ORDERS
DEGREASE
TAG
MINAMIHARA 1-31-92

LAWRENCE BERKELEY LABORATORY
UNIVERSITY OF CALIFORNIA-BERKELEY
SDC DETECTOR
ENDCAP CALORIMETER
CONNECTOR TOP PLATE
DETAIL
8817-11
FULL
20M9094

REQ	ITEM	PART NUMBER	DESCRIPTION
	1		PLATE, 3/8 INCHES THICK, ALUMINUM 6061-T6 SEE NOTE 2
REF	2		CONNECTOR BASE PLATE
REF	3		CONNECTOR TOP PLATE

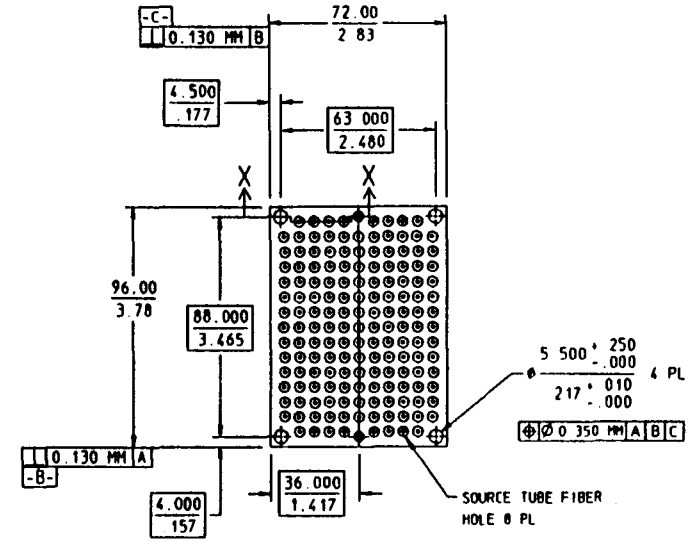

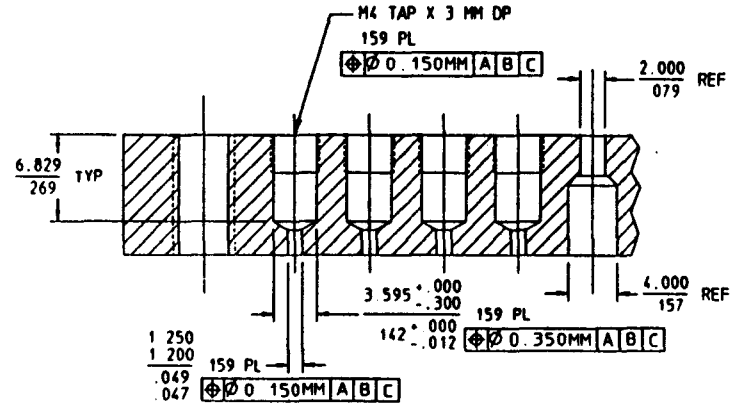

SECTION X - X
SCALE: 5X

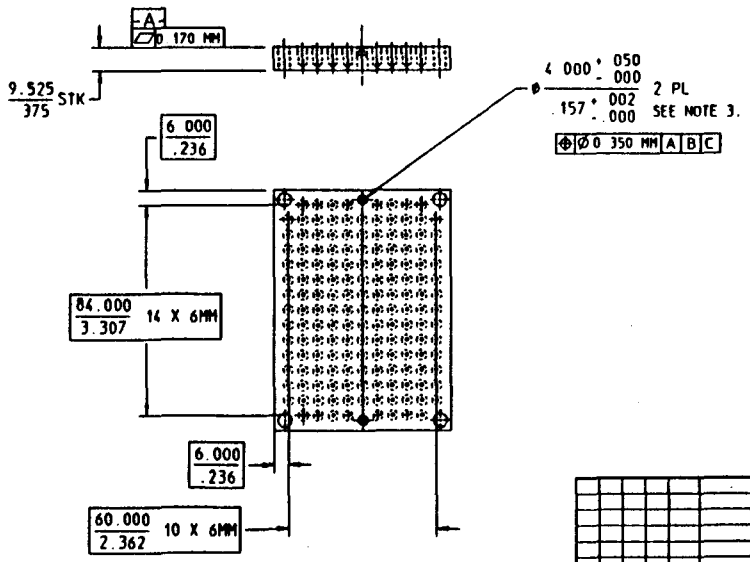

NOTES: 1. ALL DIMENSIONS ARE MILLIMETERS OVER INCHES.
2. MATCH DRILL CONNECTOR BASE PLATE WITH SUPPLEMENTAL CONNECTOR TOP PLATES AND CONNECTOR TOP PLATE WHEREVER POSSIBLE
3. MATCH DRILL AND REAM HOLE FOR A 4 MM DIA DOWEL PIN, TOTAL OF 8 DOWEL PIN HOLES.

REV	DWG	CHK	ZONE	DATE	CHANGES

UNLESS OTHERWISE SPECIFIED
NOTED
DEGREASE
TAG
MINAMIHARA
31-92

SHOP ORDERS

LAWRENCE BERKELEY LABORATORY
UNIVERSITY OF CALIFORNIA-BERKELEY
SDC DETECTOR
ENDCAP CALORIMETER
CONNECTOR SUPPLEMENTAL TOP PLATE
DETAIL
8817-11
FULL
20M9104

REQ	ITEM	PART NUMBER	DESCRIPTION
			A ROUGH CUT OF 22.5 DEG LEAD SEGMENT (SHEET, 6 MM THICK, (SN/LEAD) ALLOY, REF)

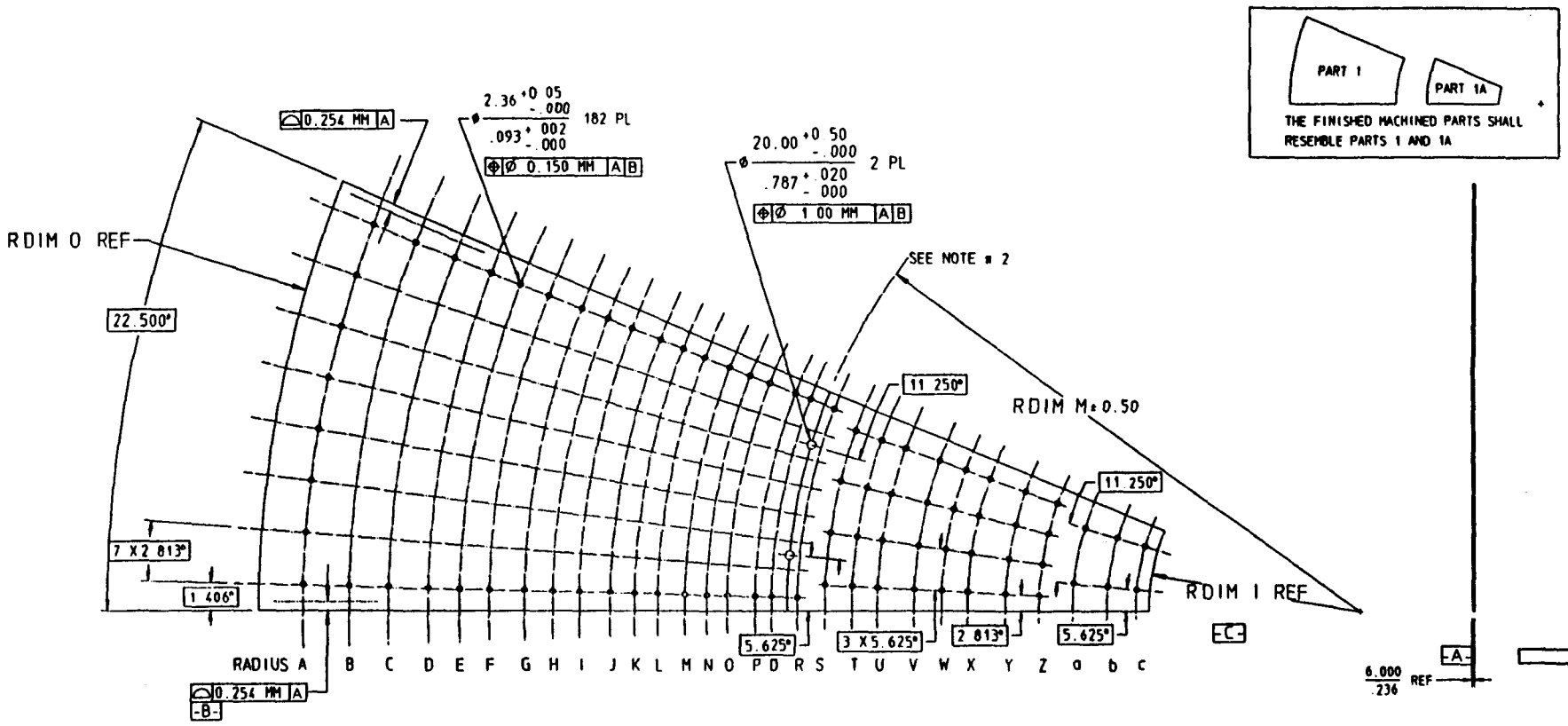

RADIUS

	A	B	C	D	E	F	G	H	I	J	K	L	M	N	O	P	Q	R	S	T	U	V	W	X	Y	Z	a	b	c
MM	2425.78	2317.88	2223.20	2132.58	2060.32	1991.64	1911.92	1848.22	1787.55	1717.07	1660.65	1606.83	1544.23	1494.07	1446.15	1383.09	1345.62	1285.90	1222.25	1159.93	1102.45	1020.05	957.38	898.11	811.49	733.25	656.06	577.53	510.60
IN	95.503	91.255	87.528	83.960	81.115	78.411	75.273	72.765	70.376	67.601	65.380	63.261	60.769	58.822	56.935	54.453	52.977	50.626	48.120	45.667	43.404	40.160	37.689	35.359	31.949	28.868	25.829	22.738	20.103

NOTE 1. ALL DIMENSIONS ARE MILLIMETERS OVER INCHES.
2. "DIM M" TO BE THE LAST MACHINING CUT AND THE WIDTH OF CUT SHALL NOT BE MORE THAN 0.400 MM.

REV	DWG	CHK	ZONE	DATE	CHANGES

UNLESS OTHERWISE SPECIFIED

SHOP ORDERS

TAG

HINAMIHARA

LAWRENCE BERKELEY LABORATORY
UNIVERSITY OF CALIFORNIA-BERKELEY

SDC DETECTOR
ENDCAP CALORIMETER
22.5 DEGREE LEAD SEGMENT

DETAIL

8817-11

1/5

20M9114

Lead Segments

Z Dim Face of Hadronic Rece		4850.000								
Zgap		0.000								
Zlead		42.570			Lead Disk L22					
Cut-width		0.500		Dim I	Dim M	Dim O				
Starting Pt. =		(Zhad+Zgap)*TAN(eta) =		479.885	1325.507	2528.704				
Disk Name	No. Req'd	Pb Seg/Disk	Total Shts Req'd	Total Wt	Mat'l Cost	Holes/22.5d	Total Holes	Dim I	Dim M	Dim O
			(42"x100"X6mm)		($0.80/Lb)					
Outer	44	16	352	143,070.68	$114,456.55					
				406.45	$325					
L1	2	16	16			144	2304		1154.285	2202.601
L2	2	16	16			144	2304		1162.005	2217.305
L3	2	16	16			144	2304		1169.725	2232.008
L4	2	16	16			144	2304		1177.445	2246.712
L5	2	16	16			144	2304		1185.166	2261.415
L6	2	16	16			144	2304		1192.886	2276.119
L7	2	16	16			144	2304		1200.606	2290.822
L8	2	16	16			144	2304		1217.425	2322.855
L9	2	16	16			144	2304		1225.145	2337.558
L10	2	16	16			144	2304		1232.865	2352.262
L11	2	16	16			144	2304		1240.585	2366.965
L12	2	16	16			144	2304		1248.306	2381.669
L13	2	16	16			144	2304		1256.026	2396.372
L14	2	16	16			144	2304		1263.746	2411.076
L15	2	16	16			144	2304		1271.466	2425.779
L16	2	16	16			144	2304		1279.186	2440.483
L17	2	16	16			144	2304		1286.906	2455.187
L18	2	16	16			144	2304		1294.627	2469.890
L19	2	16	16			144	2304		1302.347	2484.594
L20	2	16	16			144	2304		1310.067	2499.297
L21	2	16	16			144	2304		1317.787	2514.001
L22	2	16	16			144	2304		1325.507	2528.704
Totals	44	352	352			3168	50688			
Inner										
L1	2					19	608	417.896		
L2	2					19	608	420.691		
L3	2					19	608	423.486		
L4	2					19	608	426.281		
L5	2					19	608	429.076		
L6	2					19	608	431.871		
L7	2					19	608	434.666		
L8	2					19	608	440.755		
L9	2					19	608	443.550		
L10	2					19	608	446.345		
L11	2					19	608	449.140		
L12	2					19	608	451.935		
L13	2					19	608	454.730		
L14	2					19	608	457.525		
L15	2					19	608	460.320		
L16	2					19	608	463.115		
L17	2					19	608	465.910		
L18	2					19	608	468.705		
L19	2					19	608	471.500		
L20	2					19	608	474.295		
L21	2					19	608	477.090		
L22	2					19	608	479.885		
Totals	44					418	13376			